IN SITU ALUMINIUM BASED DUAL MATRIX HYBRID COMPOSITE THROUGH POWDER METALLURGY ROUTE FOR AUTOMOTIVE INDUSTRIES

By

Tasratur Reaj Neha

Student No: 1018112023

MASTER OF SCIENCE IN MATERIALS AND METALLURGICAL ENGINEERING

Supervisor: Dr. Fahmida Gulshan

Department of Materials and Metallurgical Engineering

Bangladesh University of Engineering and Technology (BUET)

February 2023

Approval Page

The thesis titled "IN SITU ALUMINIUM BASED DUAL MATRIX HYBRID COMPOSITE THROUGH POWDER METALLURGY ROUTE FOR AUTOMOTIVE INDUSTRIES" submitted by Tasratur Reaj Neha, Roll No: 1018112023, Session: October/2018, has been accepted as satisfactory in partial fulfillment of the requirement for the degree of Master of Science in Materials and Metallurgical Engineering on 22nd March 2023.

BOARD OF EXAMINERS

1.....

Dr. Fahmida Gulshan — Chairman (Supervisor)
Professor
Department of MME, BUET, Dhaka.

2.....

Head/Director — Member (Ex-officio)
Professor
Department of MME, BUET, Dhaka

3.....

Dr. Kazi Mohammad Shorowordi — Member
Professor
Department of MME, BUET, Dhaka.

4.....

Dr. Hossain Mohammad Mamun Al Rashed — Member
Associate Professor
Department of MME, BUET, Dhaka.

5.....

Professor Dr Qumrul Ahsan — Member (External)
Vice Chancellor
University of Asia Pacific, Dhaka.

Candidate's Declaration

Date: 22/03/2023

Candidate's Signature: Tasratur

Tasratur Reaj Neha

Student ID: 1018112023

Acknowledgement

First and foremost, I would like to express my gratitude to the divine for providing me with the necessary means and opportunity to complete this thesis on schedule, despite the challenges encountered.

I wish to extend my heartfelt appreciation to my supervisor, Dr. Fahmida Gulshan, for her unwavering support and guidance throughout my academic journey. Her zeal for research and dedication to her students have been a source of inspiration, urging me to strive for excellence. I am grateful for the invaluable insights and knowledge she has imparted to me, as well as for the valuable and constructive suggestions, liberal assistance, and continuous encouragement that she provided during this thesis work.

I would also like to extend my gratitude to Md Abdul Gafur, Principal Scientific Officer at the PP& PDC, BCSIR, for providing me access to his laboratory to process my samples. His technical knowledge and assistance played a pivotal role in the successful completion of this research.

I would like to express my gratitude to Md Irfan Khan, Lecturer at MME, DUET and Surya Akhtar for their consistent support in ensuring the smooth completion of this project.

Additionally, I want to express my heartfelt gratitude to my parents, aunt, and in-laws for their support in taking care of my little toddler and encouragement. I also want to thank my husband for his countless support, including assisting me during my weekly journey from Gazipur to Dhaka to complete my research work. Without the support and encouragement of all these individuals, I would not have been able to complete this project. I am deeply grateful for their contributions and for helping me achieve this significant milestone.

Abstract

In recent times, the focus of researchers worldwide has shifted from monolithic materials to composite materials, primarily due to the need for high performance and affordable materials. Amongst the various types of composite materials, aluminum metal matrix composites (AMMC) are an excellent choice for manufacturing high-specific-strength automotive components, as well as for various mechanical and tribological applications. They are preferred over other materials because of their lighter weight, which is around one-third as much as steel per cubic meter. This property not only ensures more energy-efficient automobiles but also facilitates their production at a lower cost. This study was carried out to attain a deeper understanding of the structural performance of AMMCs. For this purpose, a simple Al-H_3BO_3-TiO_2 system was utilized for AMMC production through ball milling, cold pressing, and sintering. The ball milling process was found to have a considerable impact on particle growth, and the in situ generated reinforcements provide several benefits, including strong bonding and clean particle-metal interface. During the sintering procedure, reinforcement particles were created and uniformly distributed throughout the Aluminium matrix. AMMC's dual matrix structure was observed to perform as a desired characteristic, increasing both ductility and toughness. The percentage of added external aluminum varied from 0% to 25% to 50% to 75% of the total sample. Differential thermal analysis of the green sample was performed up to 800°C, which indicated that the particle development took place after 550°C. Consequently, the sintering temperature was chosen from 600°C to 800°C. Initial microstructural analysis was carried out using optical microscopy, while scanning electron microscopy (SEM) and X-ray diffraction (XRD) techniques were utilized to examine the morphological and structural reinforcing effects of AMMCs. The presence of various in situ reinforcements, including γAl_2O_3, AlB_2, B_2O_3, TiB_2, and TiAl in aluminum matrix was confirmed through X-ray diffraction (XRD) analysis. The mechanical properties were evaluated using a diametral compression tester and a Brinell hardness tester. It was observed that hardness increased with higher sintering temperatures. The sample sintered at 800°C with 0% unmilled aluminum exhibited the highest hardness of 169.2 HV. The results showed that the highest toughness , approximately 6.12 J/m^{-3}, was found in the 75% external aluminum dual matrix composites sintered at 800°C .

Graphical Abstract

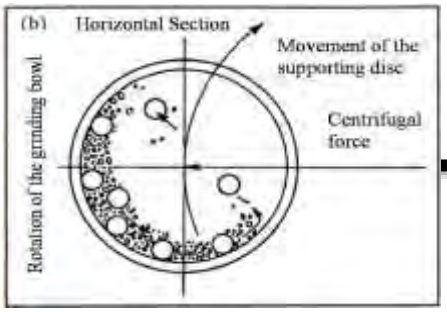

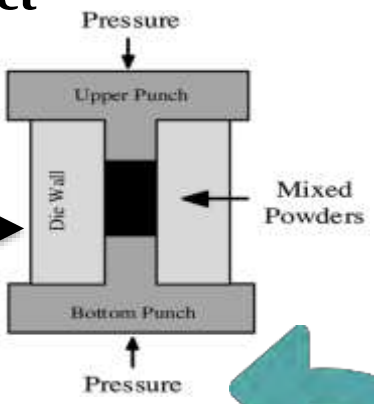

Ball Milling

Cold ompression

Final Product

Sintering

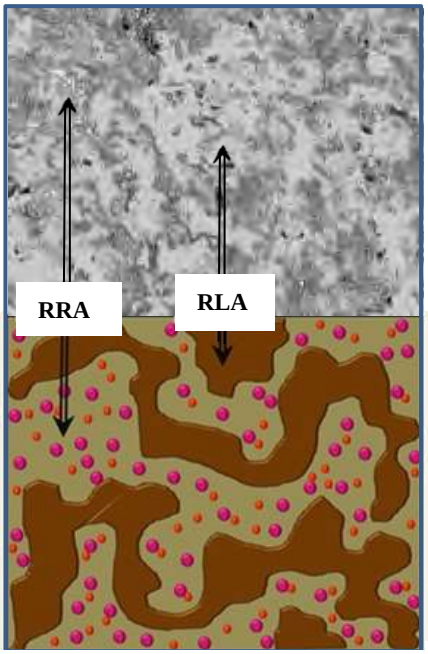

Dual matrix composites. RRA (Reinforcements rich area); RLA (Reinforcements lean area)

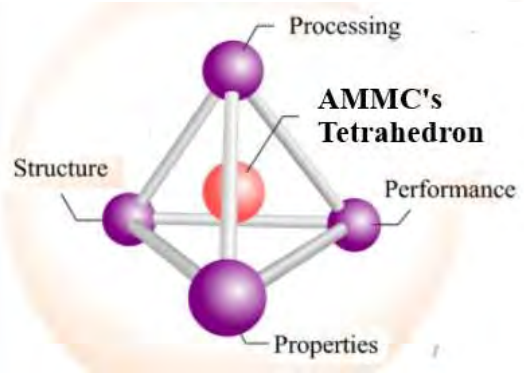

Applications(Pistons)

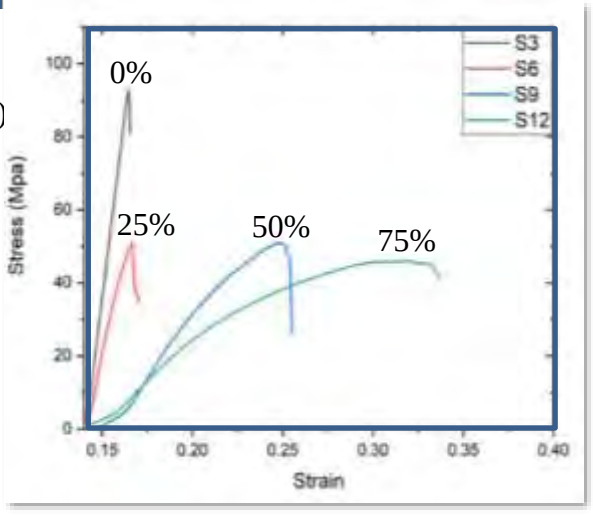

Change in toughness with increasing external aluminum percentage.

vi

Table of Contents

Contents

Table of Figures

List of Tables

List of Abbreviation

MMC	**Metal Matrix Composite**
AMMC	**Aluminium Metal Matrix Composite**
RLA	**Reinforcement Lean Area**
RRA	**Reinforcement Rich Area**
TG	**Thermogravimetry**
DTA	**Differential Thermal Analysis**
DTG	**Derivative Thermogravimetry**
XRD	**X-ray diffraction**
SEM	**Scanning Electron Microscopy**

Chapter 1: Introduction

1.1 Thesis Background and Present State

Aluminium is the favored material among designers for attaining better fuel efficiency and decreased emission levels by 2025, according to a survey by Wards Auto and DuPont. The survey indicates that using aluminum parts instead of steel reduces fuel consumption by 6.5% and vehicle mass by 10%. In addition, the vehicle's mass is lowered by 100 kg, which results in an 8 g/km reduction in CO_2 emissions. Additionally, the growth of electric vehicles has increased the demand for aluminum. The global automotive market is projected to see a 30% increase in hybrid vehicle sales by 2030. Ten million more aluminum will be needed to build electric and hybrid vehicles, according to expectations [1].

According to the assessment, there is a significant need in the current industrial sector for lightweight materials with superior mechanical and tribological capabilities, such as aluminum. For automotive applications where fuel efficiency and enhanced engine performance are becoming crucial, aluminum offers a good strength to weight ratio. It is rather challenging to meet the application requirements for many current engineering systems employing monolithic material systems since they call for materials with a wide range of qualities. Numerous techniques are employed to improve aluminum because metal cannot be utilized directly in automobiles. Although it is difficult to find reinforcements with high strength at a reasonable price, one conventional improvement includes adding reinforcements to aluminum, resulting in the creation of aluminium metal matrix composites (AMMCs). So, AMMCs are an excellent choice for high-specific-strength automobile components because of enabling vehicles to be light-weighted and save energy.

To compete with steel, aluminium needs to be reinforced with appropriate reinforcements to improve physicomechanical properties. Reinforcements favor strength, wear resistance and hardness at the expense of ductility [2 - 5]. In an aluminium dual matrix hybrid composite, a "hard" composite zone made up of various reinforcements embedded in a milled aluminium matrix is separated by a "soft" unmilled aluminium matrix in the microstructure. Because the outer aluminium matrix surrounding the composite area plastically deforms and absorbs energy, the concept of an aluminium dual matrix hybrid composites could be effective for

ductility and wear resistance along with strength. In general, reinforcements are commonly used to enhance strength and hardness. However, a drawback of reinforcements is that they tend to reduce ductility. In order to address this issue, I have conducted research on the development of a dual matrix composite, which offers a potential solution to increase toughness. While producing composites through ex-situ route hurdles include poor matrix-reinforcement bonding, floating, or sinking reinforcements, high processing temperatures, complicated processing routes and particle agglomeration [5 - 7] . In situ powder metallurgy is the most effective way to overcome these issues. In this process, high energy ball milling of the powders ensures uniform mixing and better mechanical properties [3]. In the aluminium matrix composites, the in situ generated phases Al_2O_3, TiC, TiB_2, SiC, and Al_3Ti display strong interfacial interaction with the matrix [8]. TiB_2, TiC raise wear resistance and strength; Al_3Ti increases high temperature oxidation; Al_2O_3 assists hardness, specific strength, wear resistance, high-temperature strength; SiC boosts stiffness, thermal properties, refractoriness [4 - 6] , [8 - 10]. Construction of aluminium dual matrix hybrid composites from an Al-H_3BO_3-TiO_2 system is yet to be explored. The resulting composites with two or more reinforcements are the optimum strategy for attaining the synergistic strengthening effect and making these composites appropriate for practical application.

1.2 Objectives with specific aims and Possible outcome

1.2.1 Objectives with specific aims

The objective with specific aims of this research can be enlisted as follows:

(i) Developing an economically feasible method of producing aluminium dual matrix hybrid composite from a simple Al-H_3BO_3-TiO_2 system through ball milling, cold pressing followed by sintering.

(ii) Analyzing thermal, structural, morphological, and mechanical properties to compare the findings with single matrix composites.

1.2.2 Possible outcome

The physicomechanical properties of dual matrix composites are expected to be superior to single matrix composites. The possible outcome is the production of aluminum dual matrix

hybrid composites employing a convenient and cost-effective powder metallurgy route. The probable in situ reinforcements in the composites are Al_2O_3, TiB_2, Al_3Ti, AlB_2. Fabricating dual matrix hybrid composites in a realistic manner while evaluating characteristics will aid us in developing viable materials for usage in the automotive industry.

1.3 Thesis Structure

The thesis is organized into seven chapters, which include, Chapter 1-Introduction, Chapter 2- Literature Review, Chapter 3- Materials and Method, Chapter 4 - Results and Discussion, Chapter 5- Summary and Conclusion, Chapter 6 - Recommendation to Future Work.

In Chapter 1, the research background and present state of the thesis are described, along with the objective, specific aims, and probable outcome of this work.

In Chapter 2, the relevant literature is presented in a concise and informative approach. This chapter includes different reinforcements contribution to aluminium matrix, discussion about the dual matrix composites, hybrid composites, automotive industries, AMMC production techniques and review of prior related works. This chapter also explains the required characterization techniques.

In Chapter 3, each step of the sample preparation process is described in detail, including the ball milling parameters, the mixing ratio for the formation of the dual matrix, the cold pressing parameters, and the sintering temperature. This chapter also includes comprehensive instructions for preparing samples for microscopy.

In Chapter 4, the outcomes of the sample testing are shown. The results of the work have also been carefully evaluated and compared where necessary. Based on samples, differences in microstructures are discussed with possible explanations.

In Chapter 5, a summary of the findings is presented. A conclusion focusing on the novelties of this work is also presented here. Some future work scopes are also recommended in this chapter.

In Chapter 6, future work and recommendations are listed.

Chapter 2: Literature Review

AMMCs have significantly better mechanical properties than the base alloy alone [11]. AMMCs therefore play a crucial role in the mechanical and tribological applications including automotive, aerospace, and other industries because of the improved specific mechanical properties, the typically low cost of their reinforcements and the well-developed production methods [12].

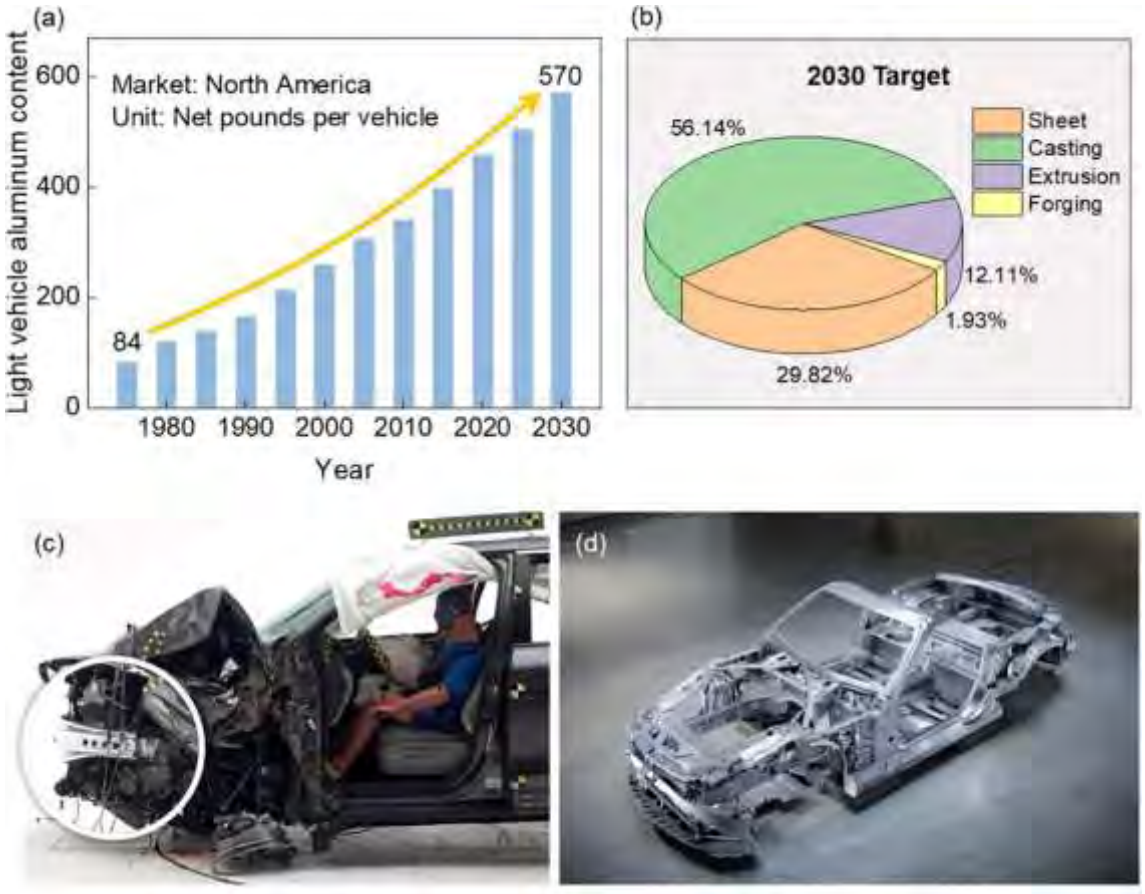

Figure 2.1 (a) Yearly change of aluminum content in the light vehicle from 1975 to 2030 (North American market), data from Light Metal Age; (b) Predicted proportion of different types of aluminum alloy in 2030; (c) Honda Pilot frontal crash test (from the Insurance Institute for Highway Safety (IIHS)), where an extruded aluminum bumper beam plays a significant role in impact protection (enlarged area); (d) New Mercedes AMG SL with high aluminum content in the bodyshell architecture to lower weight while achieving maximum rigidity (from Mercedes Benz)[13].

From an automotive engineering standpoint, aluminum and its alloys have gradually moved to the forefront of lightweight materials applied to automobiles in recent years (Figure 2.1 (a)). In 2006, aluminum overtook cast iron as the second most-used automotive material (second to steel) in the North American market [1]. Furthermore, the light vehicle aluminum content of the market is targeted at about 570 net pounds per vehicle for 2030, where the cast aluminum alloy may contribute more than 50% (Figure 2.1(b)). Specifically, an extruded aluminum bumper beam was highlighted in the crashworthiness design of the Honda Pilot for its significant role in impact protection (Figure 2.11(c)). To ensure low weight while optimizing rigidity, Mercedes Benz employed intelligent material composition with high aluminum content to manufacture the bodyshell architecture of the new AMG SL (Figure 2.1(d)). In Table 2.1 different parts of automobiles made of aluminium are shown.

Table 2.1 Aluminium for different parts of automobiles [13].

Typical components	Model	Application
Shock absorber, brake, piston, tank, wheel rim, fender, roof, door, bumper, heat insulator, handle, piping, steering component, conrod, rotor, suspension component, bonnet, chassis, spoke, valve, gas cylinder, seat frame	Audi A8	Chassis
	Jaguar XE	Monocoque
	Mercedes AMG GT	Body
	Ford F-150	Body panel
	Toyota GT86	Bonnet
	Mazda MX-5	Bumper
	Nissan Leaf	Battery case, sealing component
	Tesla Model S	Frame and heat exchangers

Production of diesel engine pistons at the Toyota automaker is a breakthrough in the application of AMMC shown in Figure 2.2(a). In 1983, Japan began producing such pistons in bulk. To reduce wear and enhance resilience to material fatigue at high temperatures, the pistons' materials were composites made of aluminum alloy matrices reinforced by ceramic

particles and fibers. The advantageous features of the materials being used are also positively impacted by lighter piston weights. In addition, the AMMC casting procedure is much simpler than the conventional method of fabricating pistons [13].

Figure 2.2 (a) Pistons made of AMMC , (b) Pushrods made of AMMC at engine , (c) Piston connecting rod [14].

Cast iron has less wear resistance than aluminum metal matrix composites , which is more wear resistant. Application of MMC reduces the engine block's overall weight by 20%. Furthermore, since AMMC has higher thermal conductivity than other materials, it can operate at lower temperatures for longer periods of time. Honda S2000 sport cars, Acura NSX automobiles, and Porsche Bower motors all feature engines with cylinder barrels built of MMC composite. Utilizing powder metallurgical techniques, such materials are created [14]. AMMC reinforced by fibers is used for production of pushrods of valves at engines shown in Figure 2.2 (b). As reinforcing material, fibers of Al_2O_3 are used. Piston connecting rod made of aluminium is shown in Figure 2.2 (c).

Aluminium alloys have distinctive physical and mechanical properties such as high tensile, high compressive strength and low weight. These materials are attractive due to some unique characteristics such as high electrical conductivity and excellent corrosion resistance [15].

To date, many efforts have been made to develop new Aluminium matrix composites (AMMC) benefiting a uniform microstructure, desirable phases and superior mechanical properties compared to Aluminium alloys [16] .

Aluminium Metal matrix composites (AMMC) are classified into several distinct classes with the type and shape of their reinforcements as shown in Figure 2.3.

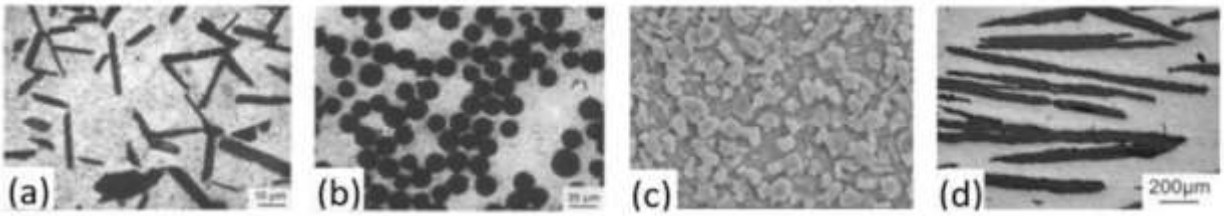

Figure 2.3 Typical microstructures of AMMCs. (a) Al/Al2O3 platelets. (b) Al/Al2O3 continuous fibres. (c) Al/SiCp. (d) Al/graphite with 20 vol.% graphite flakes taken along the basal plane [18].

Particle-reinforced AMMCs: Ceramic reinforcements, primarily oxides (for example, alumina, Al_2O_3), carbides (for example, silicon carbide, SiC), or borides (for example, titanium bromide, TiB_2), with an aspect ratio less than 5 and present in volume fraction less than 30%. They can be created by mixing metal and ceramic powders, then either solid-state sintering or liquid-metal procedures including stir casting, squeeze infiltration, and in situ processes can be used to create them.

Continuous fiber reinforced AMMCs: These have continuous fibers that are either relatively fine, typically made of Al_2O_3, SiC, or carbon, and have a diameter under 20 m, or they have coarser fibers. The bending flexibility restricts the variety of shapes that can be formed, while the former can either be parallel or pre-woven prior to infiltration to form a composite. Large diameter (100-150 m) fibers known as monofilaments are typically created by chemical vapour deposition (CVD) of either silicon carbide (SiC) or boron (B) into a core of carbon fiber or tungsten (W).

Whisker- and short-fiber-reinforced AMMCs: Although they are not continuous, these reinforcements have an aspect ratio larger than 5. The majority of AMMCs used in pistons are short Al_2O_3 fiber reinforced AMMCs. The majority of whisker-reinforced composites are made to a net or nearly a net shape using either powder metallurgy or squeeze infiltration into a fiber preform. However, because there are alleged health risks, using whiskers as reinforcements is now prohibited.

Numerous researchers have examined the microstructural characterization of aluminum composites with improvement in structural characteristics. The results of AMMCs after considering various types and forms of reinforcements are noted in Table 2.2 [3].

Table 2.2 Commonly used reinforcements in AMMCs and outcome of the research [3]

Reinforcements	**Relevant Properties**	**Application**
SiC	High hardness, stiffness, good thermal properties, and refractoriness	Connecting rod, piston, shaft, rotors, brake disc, rubber, tires, etc.
B_4C	High strength to weight ratio, hardness, chemical resistance, and good nuclear properties	Abrasives, nozzle, and ballistic armor
TiC	High wear resistance and good strength	Brake disc, rotor, and cutting tools
WC	Wear and abrasion resistance, high rigidity, impact resistance, and thermal conductivity	Machining tool, ammunition, and surgical instrument

Al_2O_3	High hardness and specific strength	Automotive industries, Aerospace, Aircraft, Refractory material, abrasives, and coatings
TiO_2	High tensile strength, impact strength and hardness	Automotive applications
ZrO_2	Wear and corrosion resistance and high fracture toughness	Ceramic tubes, cylinder liner, connecting rods, and thermal insulation
TiB_2	Wear resistance and high strength	Structural application in aerospace and automobile
ZrB_2	Thermal stability and wear resistance	Structural parts
CNT	Low density, high strength to weight ratio, ductility, and corrosion resistance	Gears, cylinder liners, and sports utilities
Graphene	High strength to weight ratio,	Biomedical application and energy storage
Red mud	Tensile strength, hardness and economical	Drive shaft, bicycle industry, brakes, and fitting
Graphite	Low density, high thermal conductivity, and good mechanical strength	Heat sinks, brake disc, and piston

However, these composites suffer some constraining drawbacks to limit their properties. Among the main limitations, low ductility originating from particle cracking and the formation of voids into aggregates of particles, brittleness of ceramic particles, and significant difference between thermal expansion coefficients of ceramic reinforcements and aluminium matrix is the most important [16],[17]. Other factors such as agglomeration of ceramic particulates and possible interfacial chemical reactions between the reinforcement and the matrix have an important effect on effective load-bearing capacity of the reinforcements and their mechanical properties [18]. To overcome these shortcomings, a high interfacial strength is required to reduce the possibility of interfacial cracking and improve the practical efficiency of particles

loading [2]. To avoid these issues in-situ synthesis can be applied. By using the in-situ synthesis approach, which produces the reinforcing particles within the matrix by chemical reactions occurring during the process, these disadvantages can be mostly eliminated.

Therefore, metal matrix composites reinforced by particles can generally be made using either in situ or ex situ production techniques. The ex situ process inevitably causes several inherent problems, such as a costly and complicated fabrication process, high synthetic temperature, agglomeration of the reinforcements and poor interfacial bonding induced by chemical reactions at the particle-matrix interfaces [19],[20] . It is generally known that agglomeration of ceramic particulates which could occur during processing of ex situ MMCs, could lead to the composites having poorer mechanical strength and toughness. Uniform distribution of ceramic particulates in the matrices of MMCs is essential to achieve effective load-bearing capacity of the reinforcement. Moreover, possible interfacial chemical reactions between the reinforcement and the matrix could also degrade the mechanical properties of ex situ MMCs.

To resolve these issues that occurred during ex situ synthesis, ceramic particles or particles are in situ fabricated to reinforce AMMCs. In in-situ composites, the reinforcing phases are formed within the matrix during composite fabrication and controlled by chemical reactions, transformations, deformation, and type of processing. Recently, particle reinforced AMMCs fabricated by the in situ reactive sintering process have attracted considerable attention from materials scientists. The advantages of such a process include clean particle-matrix interface, small size of particle reinforcements, good particle-matrix strength, and low fabrication cost. The reduction in the particle size is generally known to exhibit a beneficial effect in improving mechanical strength. Also, these reinforcers have a more uniform distribution, a lower average particle size and an interface bearing higher thermochemical stability and lower impurity. Using the preceding approach, AMMCs with a wide range of matrix materials and second-phase particles can be produced[21].

In recent years, novel processing techniques based on the in-situ production of reinforced ceramic particles have been developed. Ultrafine ceramic particulates are formed in situ by the exothermic reaction between the element constituents of composites under hot pressing conditions. So far, the in situ generated particles have been applied in Ti, Mg and Al matrix composites, such as TiB_{2w}/Ti [22],[23], MgO_w/Mg [24] and $MgAl_2O_{4w}$/Al alloys [25], [26]. The reduction in the particle size is generally known to exhibit a beneficial effect in improving

the mechanical strength[27].Using this approach, AMMCs with a wide range of matrix materials and second-phase particles can be produced.

Al_2O_3, TiC, TiB_2, SiC, and Al_3Ti are some of the in situ formed phases that have exceptional physicomechanical characteristics[8]. These characteristics include a low rate of coarsening at high temperatures, a strong interfacial bond with the aluminium alloy matrix, excellent load bearing capacity, and adequate oxidation and corrosion resistance.

High volume fractions of uniformly dispersed ceramic particles used to reinforce in-situ AMMCs show an improvement in hardness and yield strength along with a sizable loss in ductility. The existence of porosity, the development of brittle phases, or the emergence of cracks during deformation, all of which impair the capacity of AMMCs to deform plastically, are often linked to this reduction in ductility. To create high-performance aluminium-based composites, it is still difficult to maintain the excellent flexibility of AMMCs while increasing or optimizing their strength. As an alternative, inhomogeneous microstructure designs the spatial arrangements of microstructures, is one of the potential solutions that has benefited in having an ideal combination of ductility and strength. These composite materials display macroscopically homogeneous but microstructurally inhomogeneous properties.

The types of in situ produced phases for hybrid composites containing Al_2O_3-/Al_3Ti-/TiB_2- are detailed in Table 2.3. Initial materials, additives, and alloying elements employed to produce the in-situ phases are also listed .

Table 2.3 A summary of materials systems by which in situ hybrid AMMCs are fabricated[8]

In situ hybrid composite	Starting materials	Additives and alloying elements	In situ phases
Al-(Al_3Ti+X)	Al–Ti	Zn, Mg, Cu, Graphite, B, Ni	X: Al_2Cu, Al_2CuMg, $MgZn_2$, TiC, Al_3Ti, Al_4C_3, $Ti_2Mg_3Al_{18}$, Mg_2Si, TiB_2, B_4C, Al_3Ni
	Al–TiO_2	C, B, Mg, Si	X: Al_2O_3, Al_4C_3, TiB_2, TiC, MgO, Mg_2Si

	Al–K_2TiF_6	KBF_4, Cu, Si, C	X: TiB_2, Al_2Cu, Si, TiC
	Al–Al_2TiO_5	–	X: Al_2O_3
Al-(Al_2O_3+Y)	Al–CuO	SiO_2, Mg,	Y: Cu, Cu_9Al_4, Al_2Cu, Si, MgO
	Al–SiO_2	C, Mg, Ca, Na	Y: Si, Al_4C_3, SiC, Al_2O_3, MgO, Mg_2Si, $MgAl_2O_4$
	Al–ZrO_2	C, B, C, yttrium	Y: Al_3Zr, Al_4C_3, ZrC, ZrB_2
	Al–TiO_2	C, Si, CuO, B_4C	Y: TiC, Al_4C_3, Al_3Ti, Al_2Cu, TiB_2
Al-(TiB_2+Z)	Al–B	TiO_2, C, CuO, SiC	Z: Al_3Ti, Al_2O_3, TiC, Al_2Cu, Al_4C_3
	Al–B_2O_3	TiO_2, ferrotitanium	Z: Al_2O_3, $Al_{13}Fe_4$, Al_3Ti
	Al–B_4C	TiO_2, Ti	Z: TiC In, Al_2O_3
	Al–KBF_4	K_2TiF_6, K_2ZrF_6, Cu, Mg, Li, Si	Z: ZrB_2, Al_2Cu, Al_2CuMg, $Al_5Cu_6Mg_2$, Al_3Li, Al_3Zr, Al_3Zr, Al_2CuLi, $Al_{20}Cu_2Mn_3$

The in-situ formed phases, including Al2O3, TiC, TiB2, SiC, and Al3Ti, have exceptional physicomechanical qualities, such as a low rate of coarsening at high temperatures, a strong interfacial bond with the aluminium alloy matrix, excellent load bearing capacity, and adequate oxidation and corrosion resistance [28],[29].

Hybrid composites have been designed with two or more types of in situ particles to take advantage of the synergistic effects of several phases in AMMCs. For making Al-based in situ hybrid composites, the most often used in situ produced phases are Al_2O_3, Al_3Ti, and TiB_2 [8].

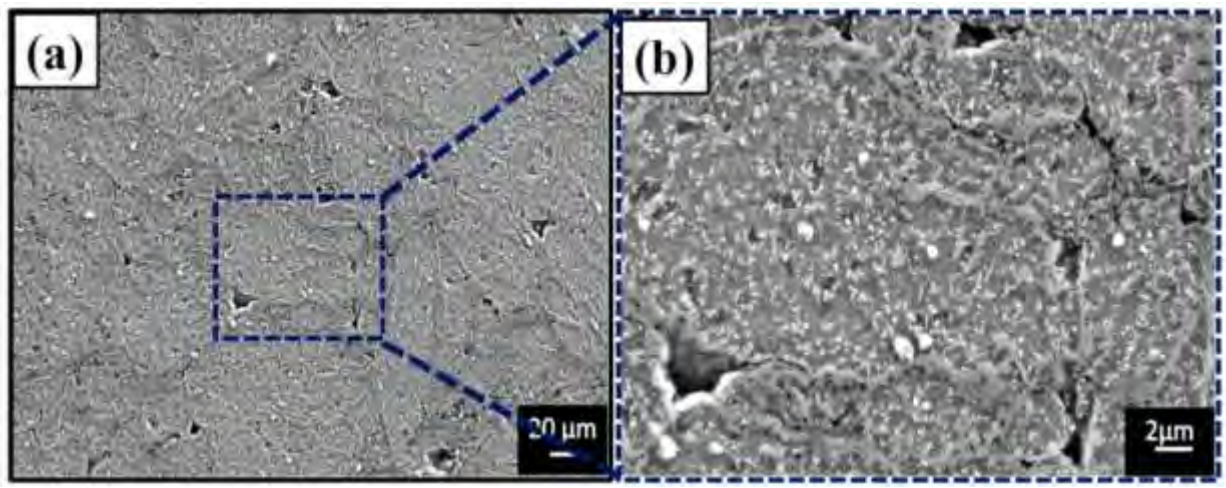

Figure 2.4 SEM micrographs of Single matrix composite [7].

Reinforcements are dispersed homogenously in single matrix composite shown in Figure 2.4. The inhomogeneous form of composites' reinforcement distribution may be lean in some areas and rich in others, as opposed to the homogenous distribution. Such inhomogeneous microstructure design includes the bicontinuous , network [30], [31], and dual matrix microstructure as some intriguing examples.

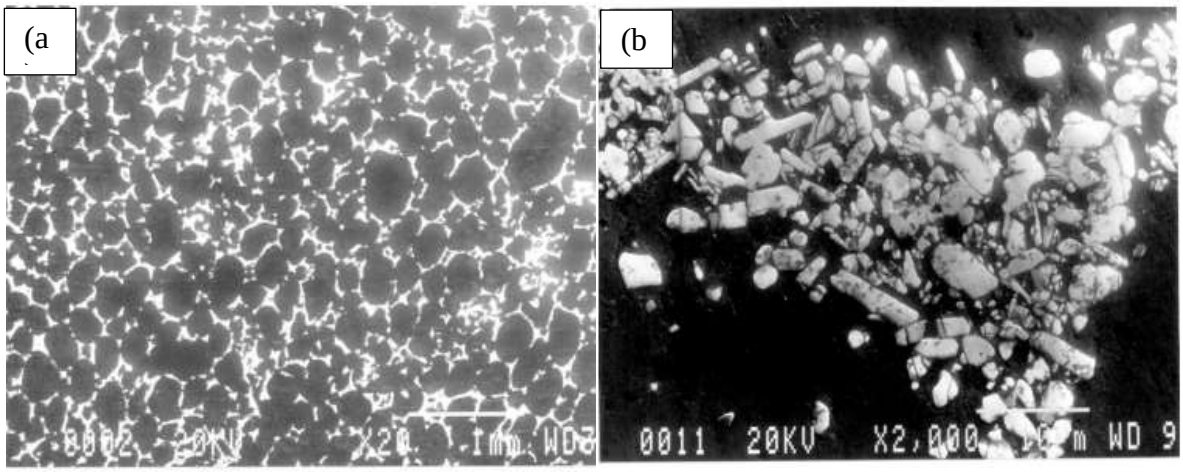

Figure 2. 5 The microstructure of the composite made from the MA130 foam (a) and strut details at high magnification (b)[32].

Bi-continuous alumina/aluminium composites were made by infiltrating an alumina preform which had the structure of a reticulated ceramic foam. The low density preforms were prepared from a polyurethane suspension of alumina powder which was pyrolyzed and sintered after foaming. The microstructure of a partially sintered ceramic foam prepared from polyurethane suspension (MA130) is shown in Figure 2.5 (a) in low magnification and 2.5 (b) in high magnification [32].

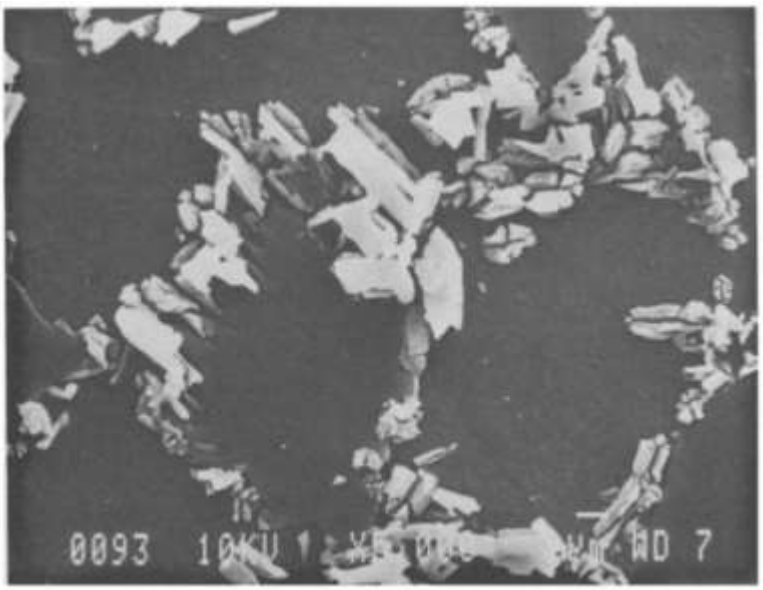

Figure 2.6 Interface of SiC particles in pure aluminium after 5 min at 800°C [30].

Figure 2.6 shows the reaction product at the SiC-matrix interface after 5 min at 800°C, in a pure aluminium matrix. The SiC particles have a high concentration of reaction products at the interface, which energy dispersive X-ray analysis showed to be $A1_4C_3$ and silicon, in agreement with the previous equations. Some of the interaction appears to be occurring along specific planes in the SiC [30].

Network microstructure is where reinforcement-rich regions are continuous in three dimensions to form a grain boundary-like network with isolated reinforcement lean phase as shown in Figure 2.7.

Dual matrix microstructure is where the composite region with a distinct inner matrix (i.e., fine grain size) is present in localized regions within the microstructure separated by a coarse grained ductile unreinforced matrix shown in Figure 2.8, Figure 2.9, Figure 2.10 and Figure 2.11.

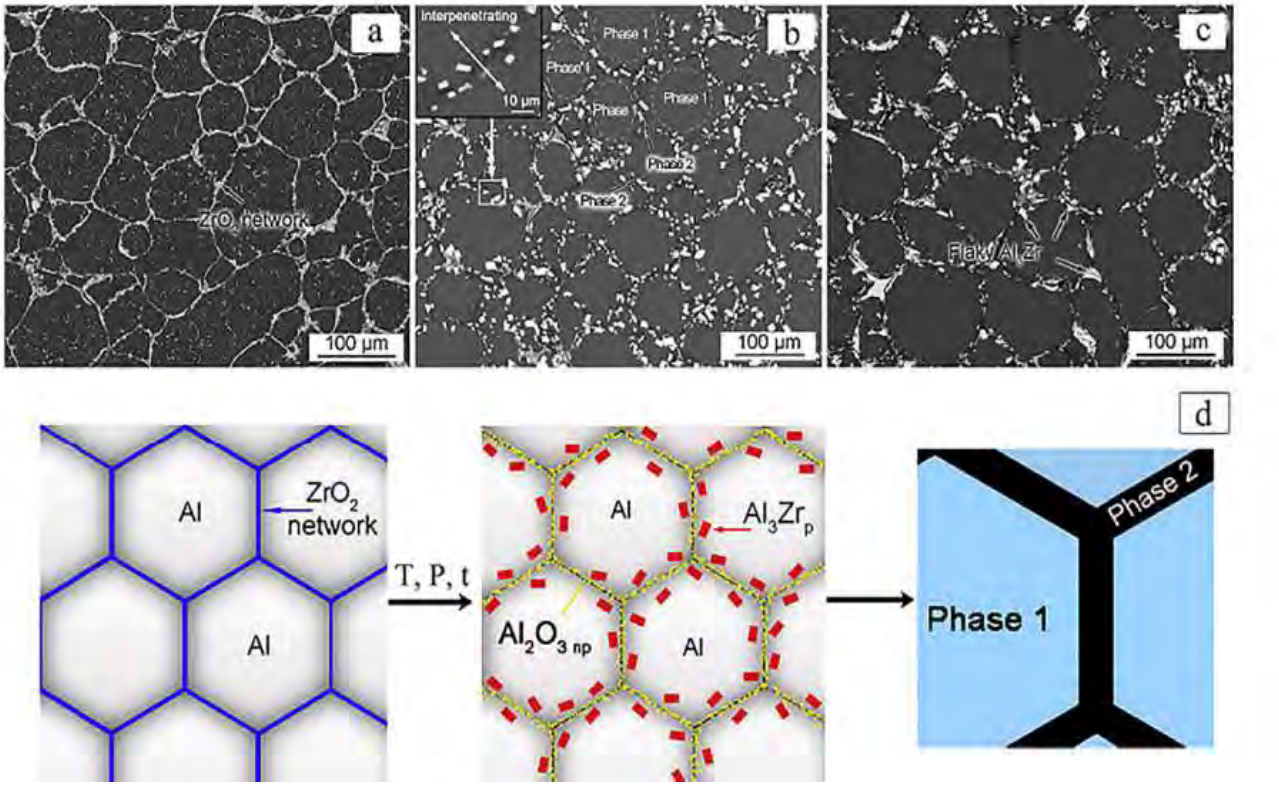

Figure 2.7 SEM micrographs of hybrid 2024Al-(Al_2O_3 + Al_3Zr) composites after a) sintering at 600 C for 1 h under 25 MPa, b) sintering at 840 C for 1 h under 25 MPa, and c) sintering at 900 C for 30 min with no external pressure; and d) a schematic illustration of the relevant phase transformations resulting in the formation of a continuous composite network. Reproduced with permission [31].

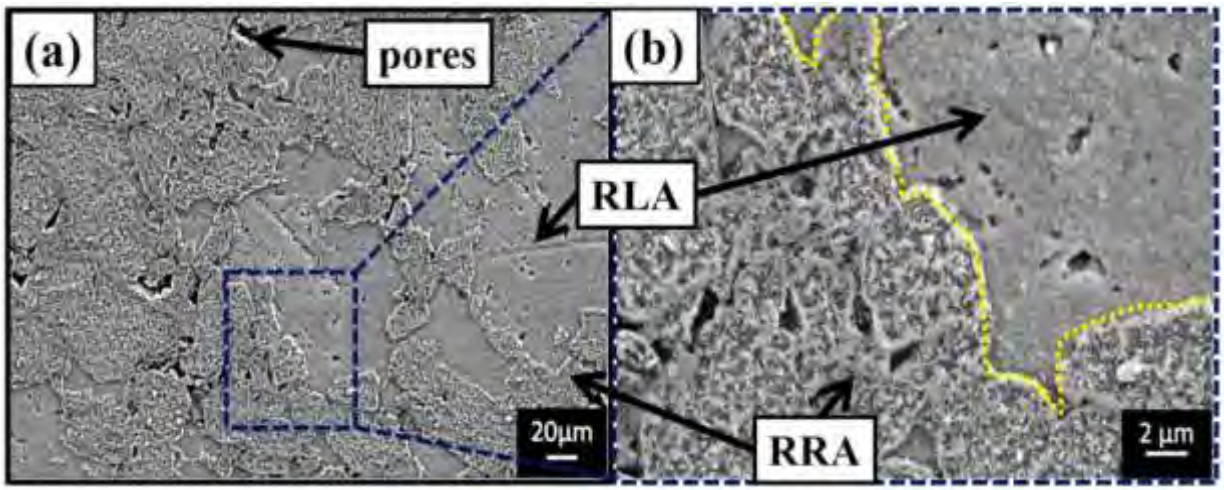

Figure 2.8 SEM micrographs of Dual matrix composites [7].

This unique microstructural concept of "composite within a composite" (i.e., dual matrix composite) has been applied to Al-CNT shown in Figure 2.9 , [33] , Ti-TiBw shown in Figure 2.10, 2.11 [34],[35], Co-WC [39,40], Al6061-SiCp [41], Al-Sn-B4C [42] The main advantage of such composites with inhomogeneous microstructure over the composites with homogeneous microstructure is the significant improvement in toughness and wear resistance.

The aim of the present investigation is to fabricate in-situ dual matrix composite, where the microstructure contains a "hard" composite region comprising of reinforcements embedded in a milled Al matrix, separated by outer "soft" unmilled Al matrix. For comparison, in-situ single matrix composite with a homogeneous distribution of reinforcements in Al matrix was also fabricated.

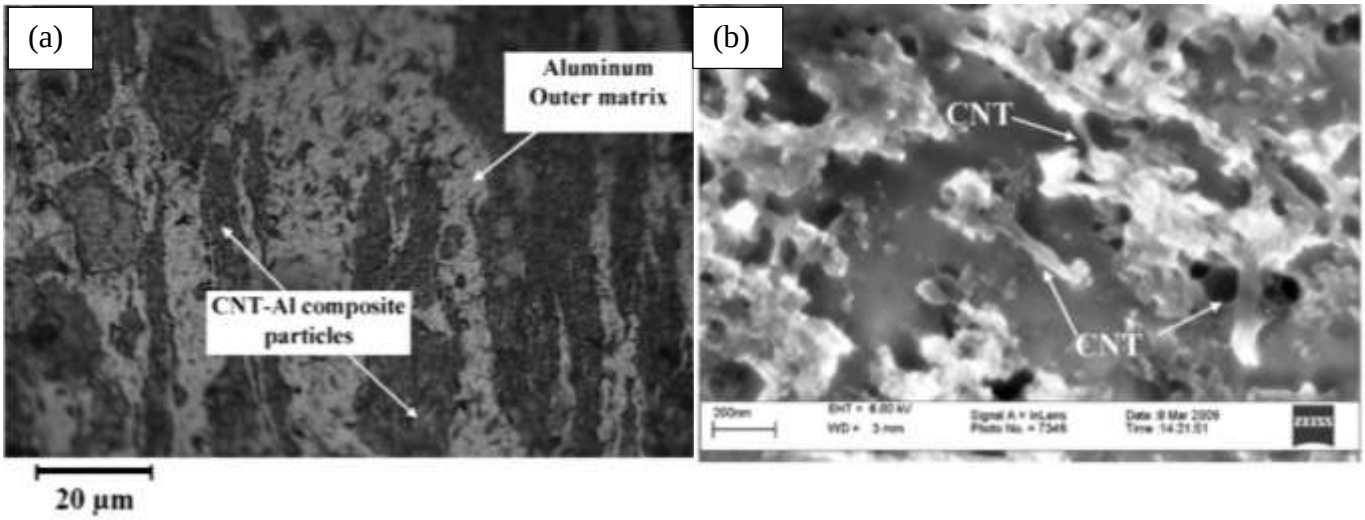

Figure 2.9 (a) Optical image of dual matrix extruded sample (extruded at 442 ◦C) showing the microstructural features along the extrusion direction, (b) FESEM image of the dual matrix composite extruded at 442 ◦C showing CNTs within the Al inner matrix [33] .

A comparative study was done on microstructure evolution, compressive behavior and of both the composites.

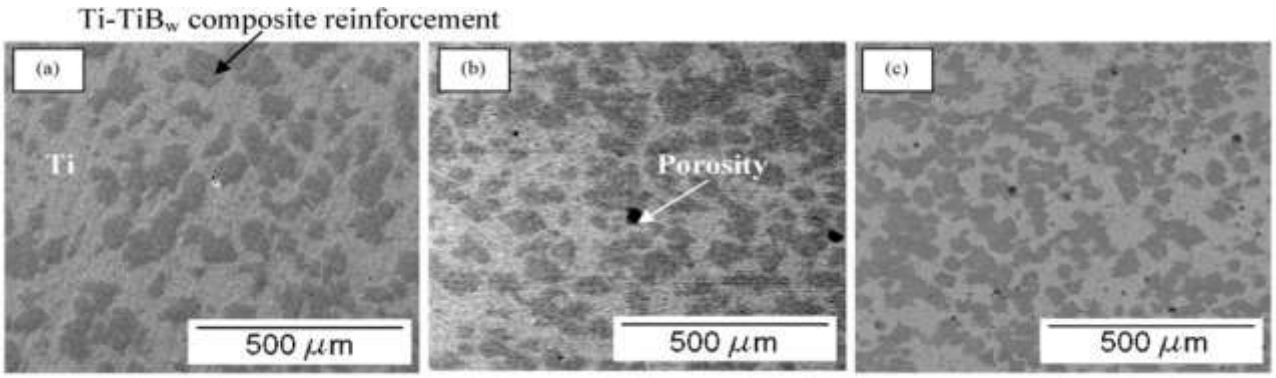

Figure 2.10 Scanning electron micrographs of dual matrix composites with reinforcement composite (Ti–TiBw) particle sizes (dark regions) (a) 90–120 m, (b) 63–90 m and (c) 45–63 m [34] .

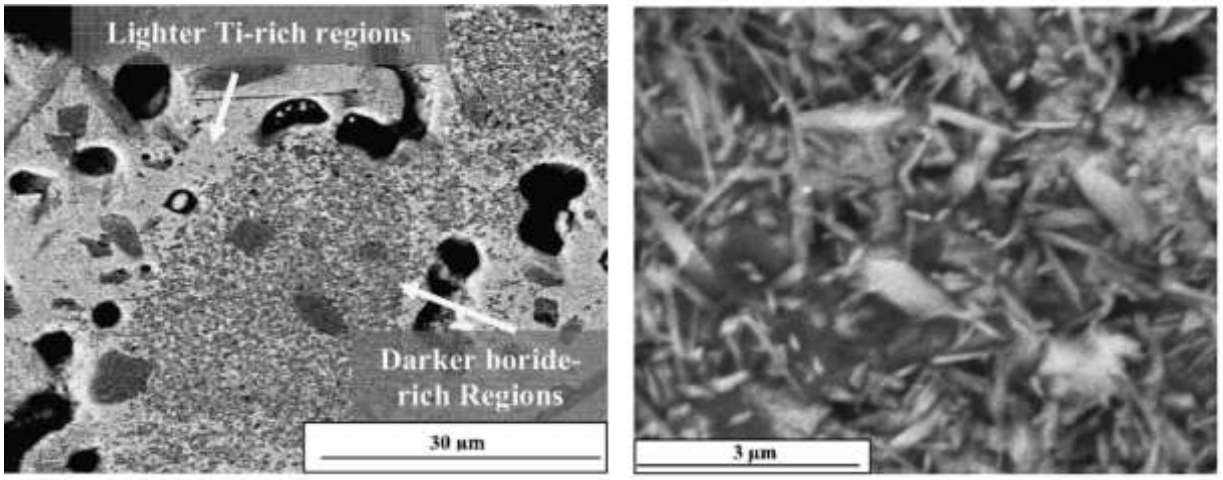

Figure 2.11 (a) Micrograph showing predominantly Ti matrix in between the Ti-boride composite regions, (b) High magnification electron micrograph of the boride-rich region generated in the Ti–TiB2/Ti (composition A) showing whisker interlocking within Ti inner matrix [35] .

AMMCs are manufactured using both liquid and solid fabrication techniques shown in Figure 2. 12 , each of which has advantages and disadvantages of its own. The use of liquid routes, such as casting, is constrained by the low wettability of reinforcement in molten aluminum. Friction stir processing (FSP) and powder metallurgy (PM) are solid approaches that address the wettability problem, but due to their criticality and high cost, researchers must choose another production method. Therefore, choosing a cost-effective processing approach is crucial to supporting the use of synthetic AMMCs. Numerous studies have been published on the

production of AMMCs using various techniques, including as gas pressure infiltration, equal channel angular processing (ECAP), squeeze casting, FSP, and stir casting (GPI)[36].

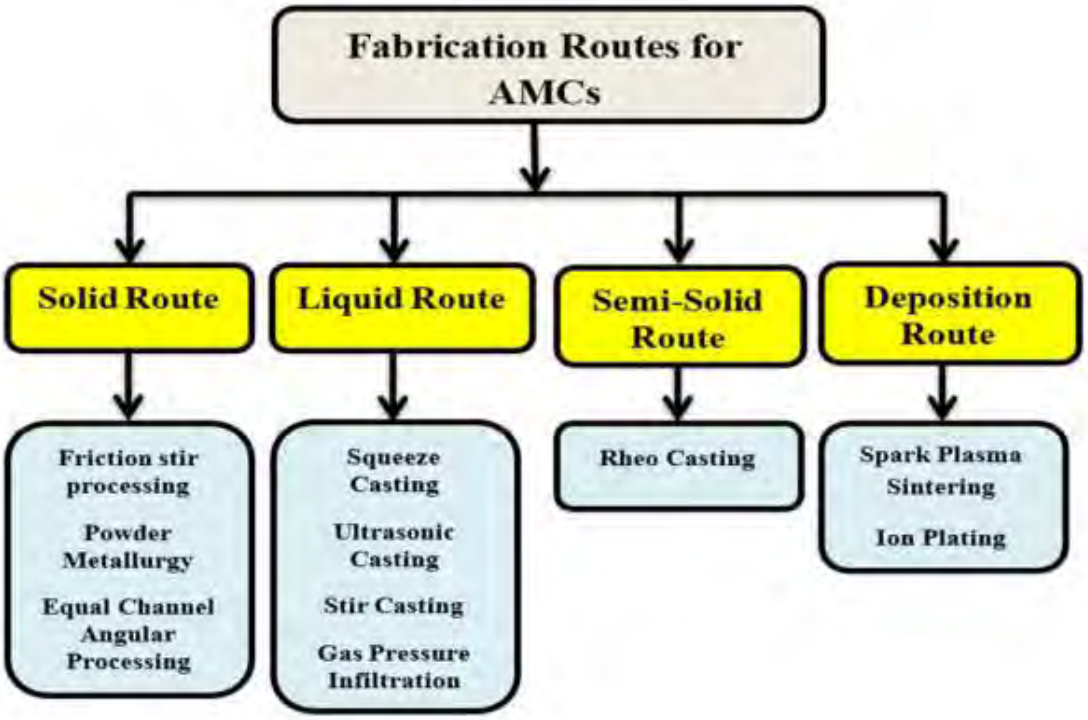

Figure 2.12 Fabrication routes for AMMCs [36].

In solid-state procedures, ceramic reinforcements are introduced into a solid phase and are either left intact or permitted to interact with the matrix. In contrast, liquid-state techniques or solidification-based methods include adding reinforcements to a metal melt while it is being stirred mechanically or electromagnetically. In general, the processes of hot working, cold working, casting, and machining are used to make components to the desired dimensions. The fabrication of components with the appropriate qualities, however, is occasionally difficult because metals and non-metals cannot be blended. By using a process known as powder metallurgy, the aforementioned limitations can be eliminated.

This technique makes it simple to manufacture and combine non-metal and metal powders in the proper ratio. The easiest and best approach for creating AMMCs is through the use of powder metallurgy. It has a number of benefits, including the uniform distribution of reinforcements throughout the matrix and the need for lower temperatures than with other

melting techniques. Because intricate geometries with precise sizes and shapes can be manufactured at high production rates in a cost-effective way, the powder metallurgy technology is well-known[37], [38].

Powder metallurgy

Powder metallurgy is a metal processing technology in which parts are produced from metallic powders by following the sequence of operations, the powders are compressed into desired shape and then heating to temperature below the melting point to cause solid state bonding of the particles into a hard-rigid mass called sintering. The main advantage of powder metallurgy is that the matrix and reinforcement are mixed in the solid state which overcomes the problem of non- wetting between the reinforcements and liquid metal and preventing the formation of any undesirable phases. It is possible to achieve uniform distribution of reinforcement into the matrix and better control of microstructure, unlike in other fabrication processes of MMCs, where agglomeration of particles is the main problem in the fabrication of particulate reinforced metal matrix composites. The powder metallurgy method gives excellent uniformity in microstructure of the composite when compared with other manufacturing techniques. Compared to other manufacturing techniques, powder metallurgy offers unique advantages due to low manufacturing temperatures [39]. This can be achieved due to solid state diffusion of

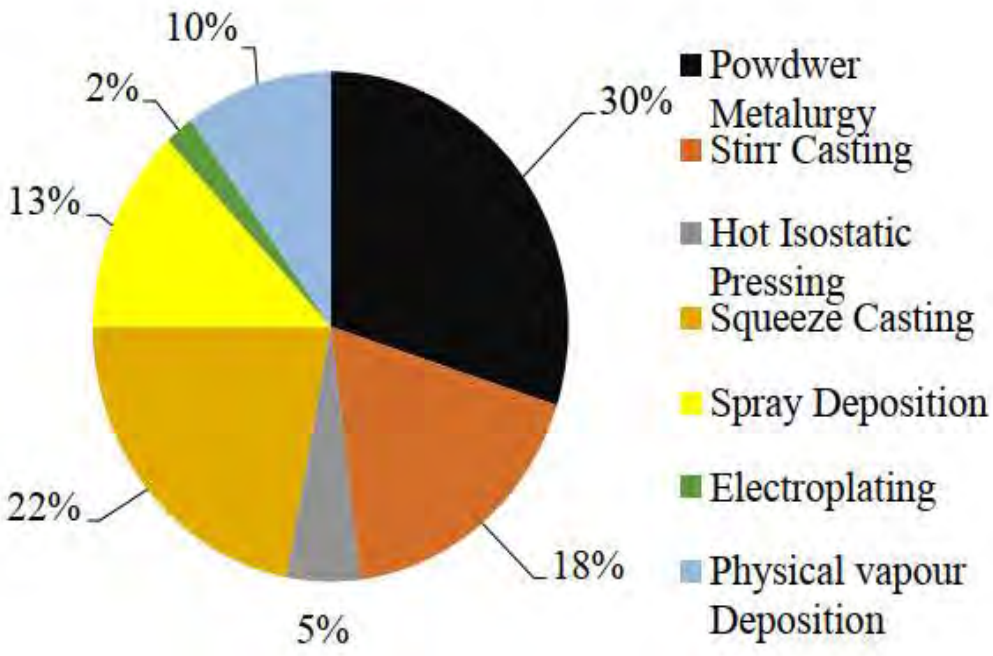

Figure 2.13 Research Studies conducted on fabrication routes of MMCs for the last 10 years [38].

inter particle bonding, whereas the diffusion bonding plays a major role in controlling the microstructure and mechanical properties of the compact [40]. The Reinforcement particle size and shape plays a major role in the fabrication. According to Figure 2.13, over the past decade, approximately 30% of all research studies were carried out through the powder metallurgy approach.

Powder blending

Blending of ceramic particles with matrix is a key step of powder metallurgy, as it facilitates the uniformity in the shapes of powder particles, controls the final distribution of the reinforcement particles and porosity in green compacts after compaction [41]. Proper blending of matrix and ceramic powders reduces the agglomeration of the powder particles. Over mixing leads to reduction in flow characteristic of the mix, leading to poor homogeneity in particle distribution. Before blending (or) mixing, the parameters mainly need to consider are reinforcement shape and size, volume percentage, blending time and speed. The flow characteristics of the particles can be improved by adding lubricants like zinc stearate (or) stearic acid in 0.25 to 5 wt.%[42].

Powder compaction

The principal objective of compaction process is to apply pressurize and bond the particles to form a cohesion among the powder particles. This is usually called green compact. For a good compaction, irregular shaped particles are preferred as they give better interlocking and hence high green strength. The indispensable amount of pressure depends upon the initial shape of the matrix and reinforcement, the matrix and reinforcement material, the method of blending and application of lubricants, additives, and desired density of green compact.

Sintering temperature

The main mechanism involved in sintering is the green compact is heated just above the melting temperature of the matrix, the matrix powder melts and reacts with other elements reinforcement in the powder mixture to form a liquid between the particles that engulfs the more refractory phase [43]. The difficulty is due to the difference in thermal expansion coefficients between the ceramic reinforcement and metallic matrix. This causes thermal mismatch strain over the reinforcement and matrix interface while cooling in processing of MMC. The associated strain is then sufficient to generate local plastic yield in the Al matrix

[44]. If the MMC is then subjected to thermal cycling, microstructural/sub structural damage can accumulate leading instability or under low loads to accelerated creep which amounts to superplastic behavior [45]. The main controlling factor in sintering is sintering temperature. The sintering temperature plays a major role in the structure of the composites, at higher sintering temperatures a close compact structure is obtained due to higher diffusion rates [39], [46]. This can be clearly understood by equation $D = Do\ exp\ (-Q/RT)$, where D is diffusion coefficient, D_o is constant, Q is activation energy, R is Boltzmann's constant and T is temperature. A proper interparticle bonding in composite is necessary for better mechanical properties like strength, magnetic and corrosive properties.

Sintering time

The diffusion in conventional sintering process depends on the sintering time. This can be clearly explained by equation $r = 2.4\sqrt{(Dt)}$ where r is the radial distance, D is the diffusion coefficient and t is the diffusion time. The radial distance is directly proportional to square root of the sintering time which is responsible for the atomic diffusion leading to finer grain structure [47].

Figure 2.14 illustrates the various stages involved in the powder metallurgy process.

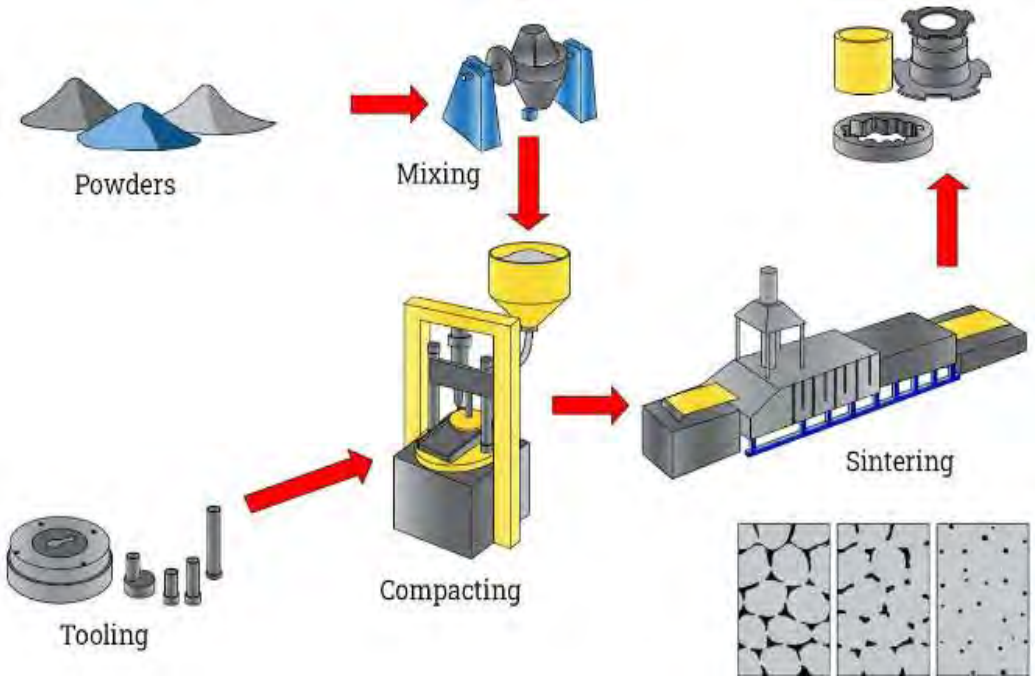

Figure 2.14 Stages of the powder metallurgy process.

Figure 2.15 indicates the schematic process diagram where AMMC is produces following powder metallurgy route [6].

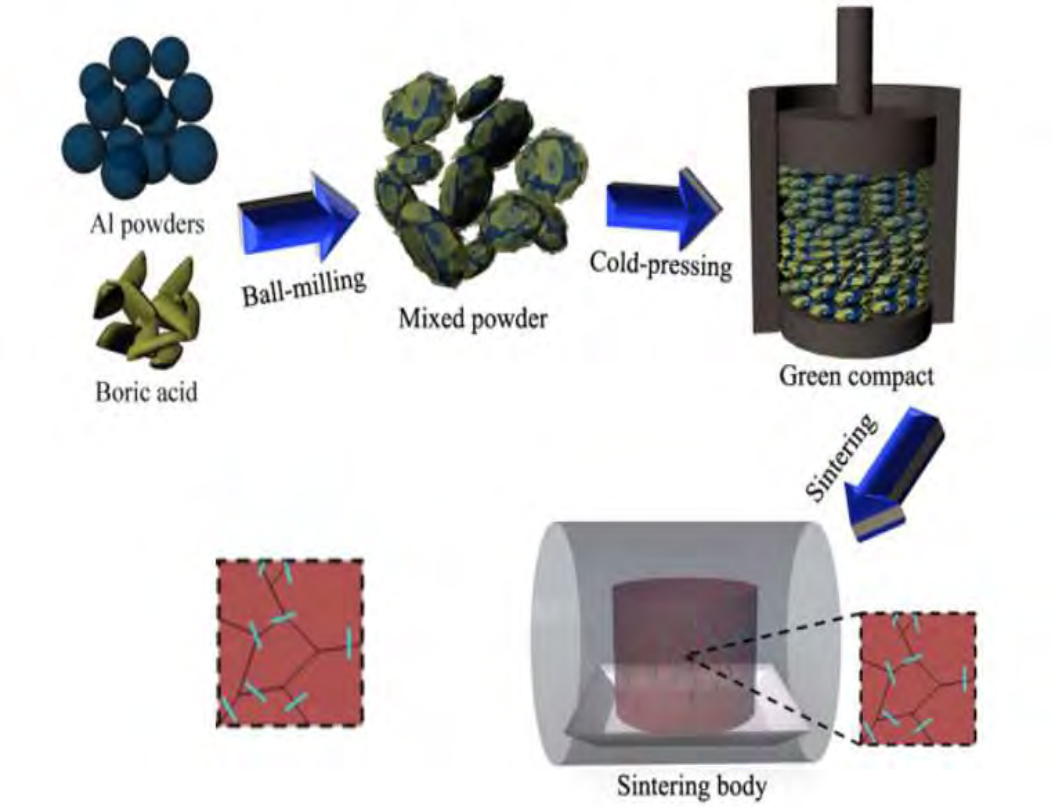

Figure 2.15 Schematic process diagram of AMMC [6] .

Chapter 3: Materials and Method

This chapter will provide a detailed discussion of the production process for an in situ aluminum-based dual matrix hybrid composite intended for automotive industries. The composite was created using the Al-TiO_2-H_3BO_3 system, where aluminum was the matrix. Al_2O_3, Al_3Ti, and TiB_2 were the most prevailing in situ formed phases to fabricate Al-based in situ hybrid composites [8].Therefore, to incorporate these reinforcements into the aluminum matrix, the Al-TiO_2-H_3BO_3 system was used.

3.1 Materials

Aluminium metal matrix composites (AMMC) were produced following powder metallurgy route, which requires all the raw materials to be in powder form.

Aluminium metal powder: Starting materials for the production of the aluminum metal matrix composites (AMMC) consisted of commercial aluminum metal powder obtained from Qualikems in India. The powders had an average size of 75 µm and a purity of 99% and no further purification was necessary prior to use. The mesh size of aluminium powder was 325.

Titanium Oxide Powder:

Titanium oxide powder with 99% purity from Merck India was utilized as depicted in Figure 4.2 (a). The purpose of adding TiO_2 to the mixture was to enable a reaction with aluminum and boric acid, resulting in the formation of in-situ reinforcements.

Boric Acid Powder:

Boric acid powder with a purity of 99% from Research Lab was incorporated into the mixture to facilitate a reaction with aluminum and titanium oxide, resulting in the formation of in-situ reinforcements. Figure 3.2 (b) represents the boric acid powder.

Stearic Acid Powder:

To prevent cold welding of the metal powders during ball milling, stearic acid was included in the mixture as a processing control agent. The stearic acid powder shown in Figure 3.3 was added at a concentration of 0.2% of the total mixture.

.

Reagents Used:

Aluminium metal powder is very sticky to use. During fabrication it was difficult to separate the die components after cold compression. For that reason, mold release reagent spray was used.

Apparatus and Equipment for the fabrication:

(i) Digital Weight Machine (PScale P3.220)
(ii) Planetary Ball Mill (Biobase BKBM V-0.4)
(iii) 10 mm Diameter Compression Die (MTI corporation, USA)
(iv) Cold Pressing Machine (P/O Weber, Germany)
(v) Advanced wire chamber furnace (Lenton laboratory furnace)
(vi) Petri Dish, Conical Flask, Beaker (Pyrex, UK), Spatula
(vii) Aluminium foil (Local Market)

3.2 Fabrication Process:

3.2.1 Al - TiO_2 - H_3BO_3 system

It has been found that Al and TiO_2 react in the temperature range from 650°C to 800°C forming Al_3Ti [50]. In Al-B_2O_3 system,the exothermic peak, in the range of 550–650 °C, is due to the reaction of B_2O_3 and Al to form gamma-Al_2O_3 [27],[51],[52], [53],[54],[55], [56].

$2H_3BO_3 = 3H_2O + B_2O_3$

$2Al + B_2O_3 = Al_2O_3 + 2B$

$3TiO_2 + 4A1 = 2Al_2O_3 + 3\ [Ti]$

$[Ti] + 3A1 = A1_3Ti$

$[Ti] + 2B = TiB_2$

$Al + 2B = AlB_2$

3.2.2 Experimental Details

The following process diagram in Figure 3.1 shows how the dual matrix composites were synthesized following powder metallurgy route. First powders are weighted using precision weight machine. Then the powders of calculated ratio are ball milled for a 12-hour period. Then for the dual matrix composites production, ball milled powders mixed with unmilled Aluminium powder. To produce the green product, cold compression using a hydraulic press and a 10 mm diameter die were used. Finally sintering was done to get the finished product.

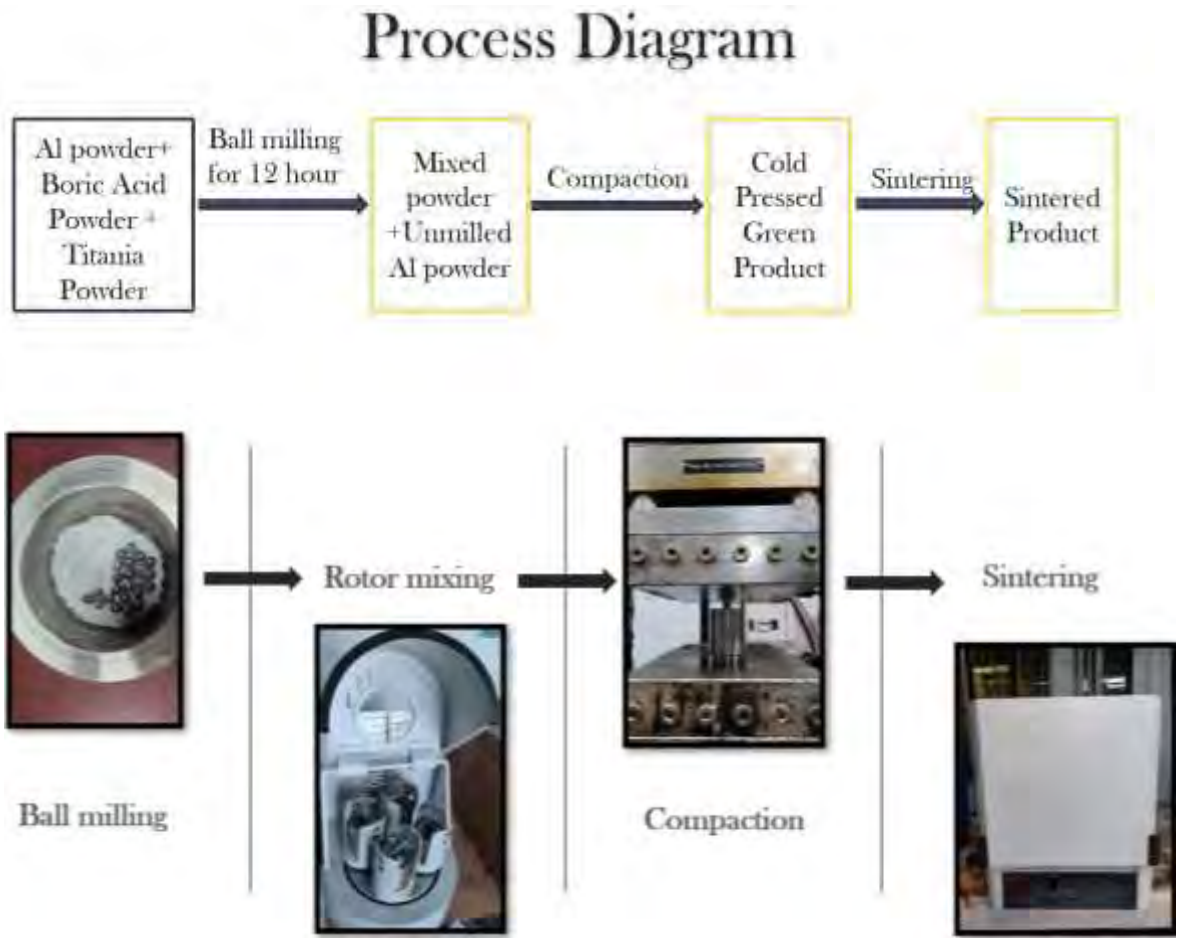

Figure 3.1 Processing route

3.2.2.1 Ball Milling Parameters

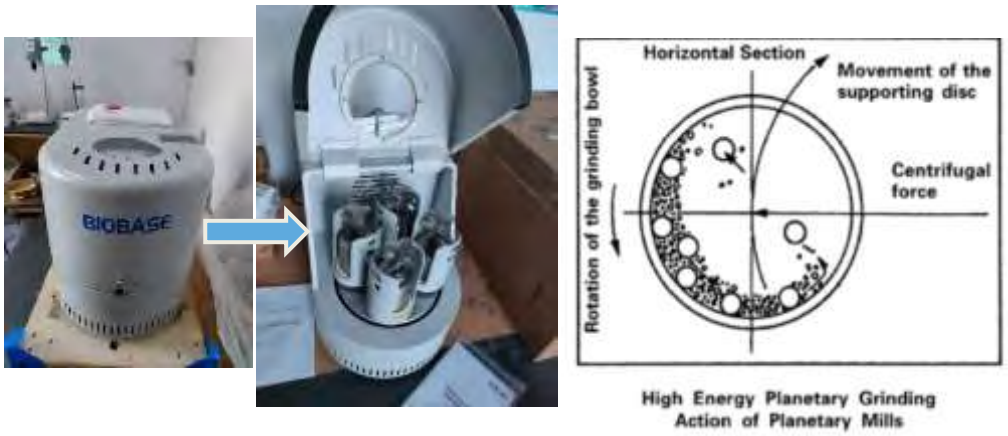

Figure 3.2 Ball milling of powders

The ball milling machine (Model: Biobase BKBM V- 0.4) shown in Figure 3.2 was used. High-energy ball milling is a ball milling process in which a powder mixture placed in a ball mill is subjected to high-energy collisions from the balls. It is a ball milling process where a powder mixture placed in the ball mill is subjected to high-energy collision from the balls. The above figure shows the motions of the balls and the powder. Since the rotation directions of the bowl and balls are opposite, the centrifugal forces are alternately synchronized. Thus, friction resulted from the hardened milling balls and the powder mixture being ground alternately rolling on the inner wall of the bowl and striking the opposite wall.

The jar of the ball milling machine can be made of Zirconia , Tungsten ,Stainless steel ,PTFE and so on. In my experiment , jar and balls are made of Stainless steel . In Table 3.1 the ball milling parameters are enlisted.

Table 3.1 Ball milling parameters

Ball milling parameters	
Jar and balls material	Stainless Steel
The ball-to powder mass ratio	10:1
Rotation speed	400 rpm
Ball milling time	12 h
Ball diameter	10 mm

Figure 3.3 Well dispersed TiO_2, H_3BO_3 within Al particles

12-hour ball milling ensures the generation of Al-TiO_2-H_3BO_3 mixed powders shown in Figure 3.3 , which would react during sintering.

3.2.2.2 Rotor Mixing Parameters

To produce dual matrix composites, the milled powder was mixed with unmilled aluminium powder. After ball milling the powders were ready to mix with unmilled powders. For this purpose, I used a planetary ball mill without balls shown in Figure 3.4 .

Figure 3.4 Planetary ball mill was used for rotor mixing.

External unmilled aluminium was added to the mixture in three different percentages:

(i) 25% unmilled aluminium to 75% milled powder.

(ii) 50% unmilled aluminium to 50% milled powder.

(iii) 75% unmilled aluminium to 25% milled powder.

Table 3.2 indicates the rotor mixing parameters.

Table 3.2 Rotor mixing parameters.

The rotor mixing parameters	
Used jar material	Stainless steel
Rotation speed	100 rpm
The mixture mixing time	30 minutes

3.2.2.3 Composition of the samples

Table 3.3 Composition of the 12 types of samples

SAMPLE NO	H_3BO_3	TIO_2	MILLED AL	UNMILLED AL
S1	7.78%	15.07%	77.15%	0%
S2	7.78%	15.07%	77.15%	0%
S3	7.78%	15.07%	77.15%	0%
S4	5.84%	11.30%	57.86%	25%
S5	5.84%	11.30%	57.86%	25%
S6	5.84%	11.30%	57.86%	25%
S7	3.89%	7.54%	38.58%	50%
S8	3.89%	7.54%	38.58%	50%
S9	3.89%	7.54%	38.58%	50%
S10	1.95%	3.77%	19.29%	75%
S11	1.95%	3.77%	19.29%	75%
S12	1.95%	3.77%	19.29%	75%

S1, S2, S3 have the same composition but they differ by sintering temperature.

3.2.2.4 Cold compression Parameters

Obtained Al-TiO_2-H_3BO_3 composite powders were cold pressed in a steel mould of 10 mm diameter under a pressure of 510 MPa.

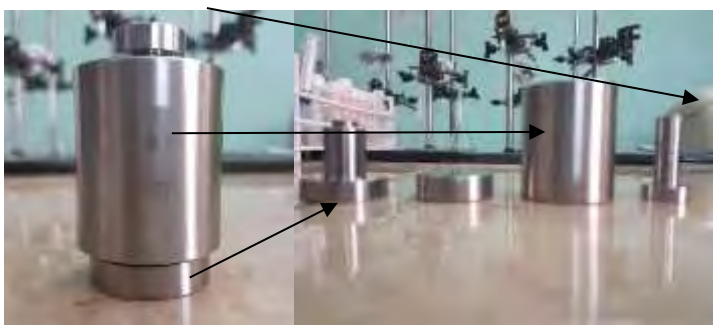

Figure 3.5 10 mm diameter Compression die (MTI Corporation)

In Figure 3.5 the die which was used for compression is shown. The die was cleaned with acetone after every green tablet sample production. Initially, it was difficult to separate the parts of the die. Then mold releasing reagent (dry molelube) was used before cold compression process. After using this mold release agent, the problem was solved. After every piece synthesis, the die was washed with acetone.

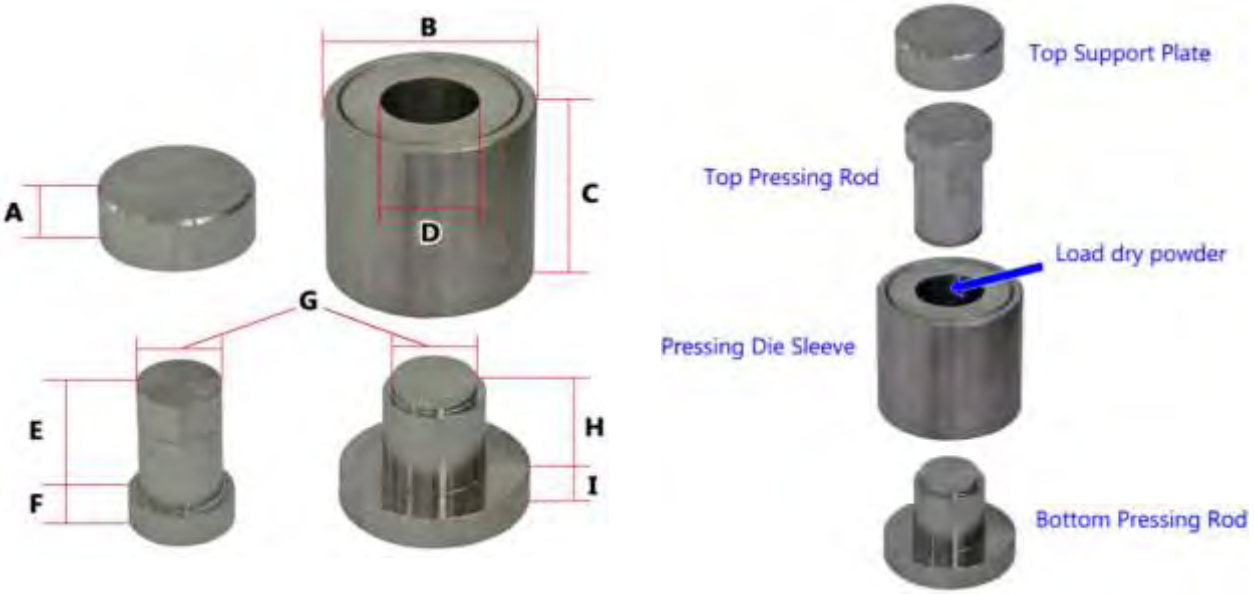

Figure 3.6 Different parts of die

Dimension of the die:

Dimension of the die is shown in Figure 3.6.

A: Support Plate Thickness: 11.5mm

B. Sleeve O.D.: ⌀40mm

C. Die Sleeve Height: ⌀47mm

D. Sleeve I.D.: ⌀10 mm + 0.03-0.05mm

E. Top Pressing Rod Body Length: 28.6mm

F. Top Pressing Rod Head Thickness: 5.4mm

G. Pressing Rod Diameter: ⌀10 ± 0.1mm

H. Bottom Pressing Rod Body Length: 20mm

I. Bottom Pressing Rod Head Thickness: 8.2mm

Material of the die:

HRC 60 - 62 hardened steel

Maximum Load:

8 metric Ton (at room temperature) 1000 MPa

Figure 3.7 Cold Compression in a die using hydraulic press (P O/ Weber).

Figure 3.7 represents the cold compression process using hydraulic press.

Figure 3.8 shows the flow chart of cold compression .

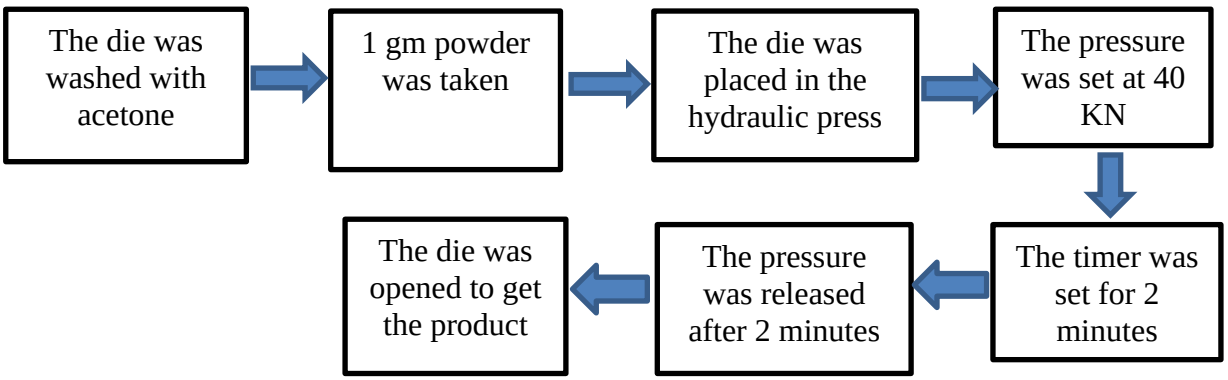

Figure 3.8 Flow chart of cold compression

The pressure is shown in the following equation.

$\sigma = F/A$ = 40000N / (π* $5mm^2$) = 510 MPa

The pressure was applied for two minutes.

Here σ indicates compressive strength in MPa. Force and Area are indicated by F and A respectively. After this stage, green samples are found shown in Figure 3.9.

Figure 3.9 Green samples before sintering

GREEN SAMPLE PARAMETERS
Cylindrical shape
10 mm diameter
5 mm height
1 gm weight

3.2.2.4 Sintering Parameters

Sintering of samples were done using Lenton laboratory furnace (advanced wire chamber furnace) . Figure 3.10 shows the sintering process.

3.2.2.4.1 Sintering Time & Temperature Selection

Sintering time: One hour

With increasing the sintering time more than one hour, the incomplete chemical reactions tend to terminate and increase the released gas volume thereby escalate the volume fraction of microcracks and porosities [2]**.**

Sintering temperature Range: 600℃ - 800℃

The density values increase with more Al_2O_3 particles nucleate and grow at Al/TiO_2 interfaces along the preferred crystal orientation sintering above 630℃. The amorphous oxide layers predominantly transformed to crystalline Al_2O_3 phases at 630℃ [57].

Approximate temperature for TiB_2 formation was 750℃ [38]. Sintering of the samples were done at 600℃ - 800℃ temperature range for one hour.

Figure 3.10 Sintering of samples using Lenton laboratory furnace (advanced wire chamber furnace)

Both side panels shown in Figure 3.11 have some heating elements. Rapid heating and maximum temperature uniformity are ensured by these wires.

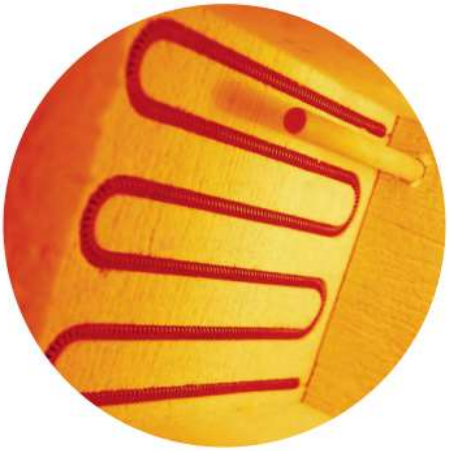

Figure 3.11 Rapid heating and maximum temperature uniformity are provided by two side panel heating elements.

3.2.2.4.2 Probable Reactions during Sintering

Orthoboric acid undergoes a dehydration reaction at 100℃, resulting in the formation of metabolic acid. Further heating to 160℃ converts metabolic acid into tetraboric acid. Upon heating tetraboric acid to high temperatures, it decomposes to yield Boron trioxide, which is the anhydrous form of orthoboric acid.

At 100 ℃ , $4H_3BO_3 = 4HBO_2 + 4H_20$

At 160 ℃ , $4HBO_2 = H_2B_40_7 + H_20$

From 162 ℃ to 430 ℃, $H_2B_40_7 = 2B_20_3 + H_20$

From 550 ℃ to 650 ℃, $2Al + B_2O_3 = \gamma Al_2O_3 + 2B$

At 500 ℃ , $Al + 2B = AlB_2$

From 550 ℃ to 600 ℃,

$3TiO_2 + 2Al = 3TiO + \gamma\ Al_2O_3$

$3TiO + 2Al = 3[\ Ti] + \gamma Al_2O_3$

$Ti + Al = TiAl_3$

At 750 ℃ , $Ti + 2B = TiB_2$

Sintering temperature was selected between 600 ℃ to 800 ℃ .

3.3 Sample Types

In my experiment, for dual matrix preparation, I had added 0% , 25%, 50% and 75% external aluminium. 0% external aluminium actually represents single matrix composite. For each percentage of external aluminium , sintering temperature varies from 600 ℃ to 800 ℃. Eventually, I synthesized 12 types of sample shown in Figure 3.16.

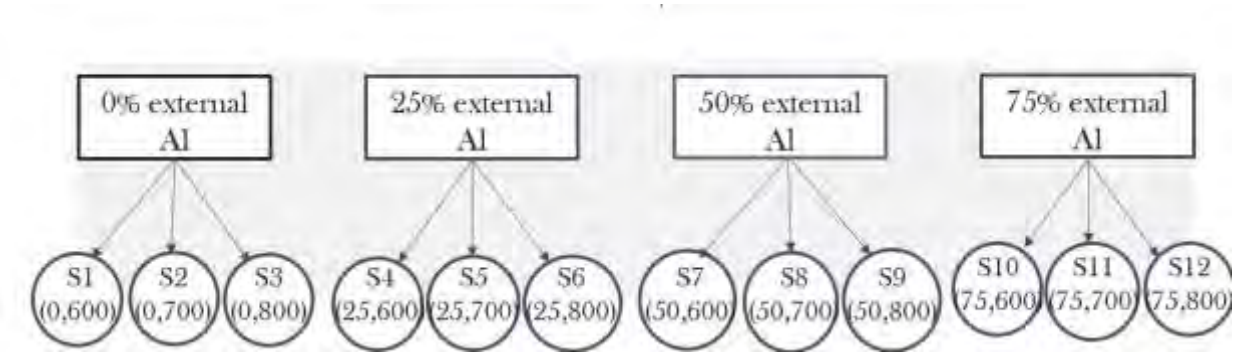

Figure 3.12 12 Types of Samples

S1(0,600) indicates that this sample has 0% external aluminium, and it is sintered at 600℃.

3.3.1 Sample Storage

After synthesis , the samples are stored as shown in Figure 3.13 for further characterization.

Figure 3.13 Samples after sintering

3.4 Characterization

Thermogravimetric analysis and Differential thermal analysis were performed using green samples.

Phase identification and crystal structure were determined by X-ray diffractometer (Rigaku, Model: SmartLab)

Morphology of the sintered samples were evaluated by Field Emission Scanning Electron Microscopy (JSM-7600F, Tokyo, Japan) and Optical Microscopy.

Diametral Compression test and Vickers Hardness tests were done on sintered samples.

3.4.1 Thermogravimetric analysis and Differential thermal analysis

To determine the sintering temperature for producing in-situ composites, thermal analysis was performed using an alumina crucible under N_2 atmosphere with a flow rate of 60 ml/min. The analysis was carried out over a temperature range of 50-800°C with a heating rate of 10 ℃/min.

3.4.2 X- Ray Diffraction Analysis

XRD analysis was carried out using Bruker [Bruker D8 advanced model] as shown in Figure 3.14. For XRD, Cu-Kα radiation with wavelength of 0.15478 nm was used for the inspection.

Figure 3.14 X-Ray Diffractometer (Bruker D8 Advance, Germany)

3.4.3 Microstructure Analysis

The mirror-like surfaces were made ready for etching after polishing and grinding. Keller's reagent was used as an etchant to analyze the microstructures.

3.4.3.1 Sample Preparation for Optical & Scanning Electron Microscopy

Sintered samples need to be prepared for morphological analysis. The following stages were followed for sample preparation.

Grinding

Silicon carbide grinding papers were used sequentially (320,600,800,1200 and 1500).

Polishing

Two step polishing was done until mirror like polished surface.

First step polishing followed by finer polishing cloth.

Etching

Keller's reagent was used for etching.

Keller's reagent formula:

95 mL water, 2.5 mL HNO_3, 1.5 mL HCl, 1.0 mL HF.

3.4.3.2 Scanning Electron Microscopy Analysis

To observe the grain size and morphology of the samples, Field Emission Scanning Electron Microscope [FESEM: JEOL JSM 7600F] was used shown in Figure 3.15.

Figure 3.15 Field Emission Scanning Electron Microscope (JEOL JSM 7600F)

3.4.4 Mechanical Properties Analysis

3.4.4.1 Vickers Hardness Testing

The Vickers hardness test measured the microhardness of the samples.

In this test, a diamond pyramid indenter is pressed into the surface of the material under a specific load for a fixed period of time. The size of the indentation is then measured under a microscope, and the hardness value is calculated based on the dimensions of the indentation.

In this case, the Vickers hardness tester was used with a load of 1 kg for 10 seconds. This test provides a quantitative measure of the hardness of the AMMC samples .

3.4.4.2 Indirect Tensile Strength

The diametral compression test is a method used to indirectly assess the tensile strength of a material. In this test, the material is compressed diametrically, causing a tensile stress to develop perpendicular to the applied force. By measuring the load and deformation during the test, the indirect tensile strength of the material can be determined. Figure 3.16 indicates the diametral compression test setup used for the testing of samples indirect tensile test.

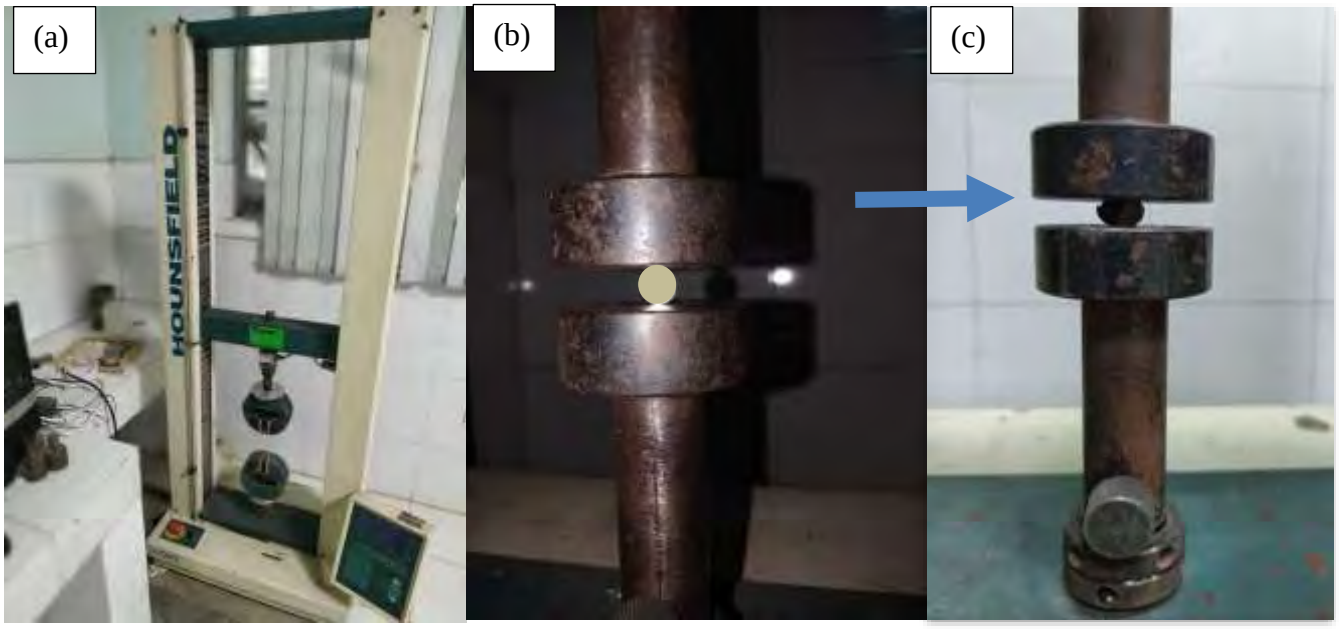

Figure 3.16 (a) Diametral compression test setup (H100KS HOUNSFIELD UTM was used) (b) before starting diametral compression test (c) during diametral compression test.

3.4.4.3 Toughness

Toughness is a measure of a material's ability to absorb energy before it breaks or fails. It is an important mechanical property of materials, particularly for applications where the material may be subjected to dynamic loads or impact. The toughness of a material can be determined from the stress-strain curve, which plots the stress (force per unit area) experienced by the material as a function of the strain (deformation) it undergoes. By analyzing the shape of the stress-strain curve, the toughness value can be calculated as the energy absorbed by the material before failure.

The diametral compression test shown in Figure 3.20 provided information on the toughness of the AMMCs.In this case, the toughness value of the AMMC samples was calculated from the stress-strain curve. This provides a more comprehensive understanding of the behavior of the material under loading conditions and helps to assess its suitability for different applications.

Chapter 4: Results and Discussion

4.1 Thermal Analysis

4.1.1. Thermogravimetric Analysis of Green Sample

.

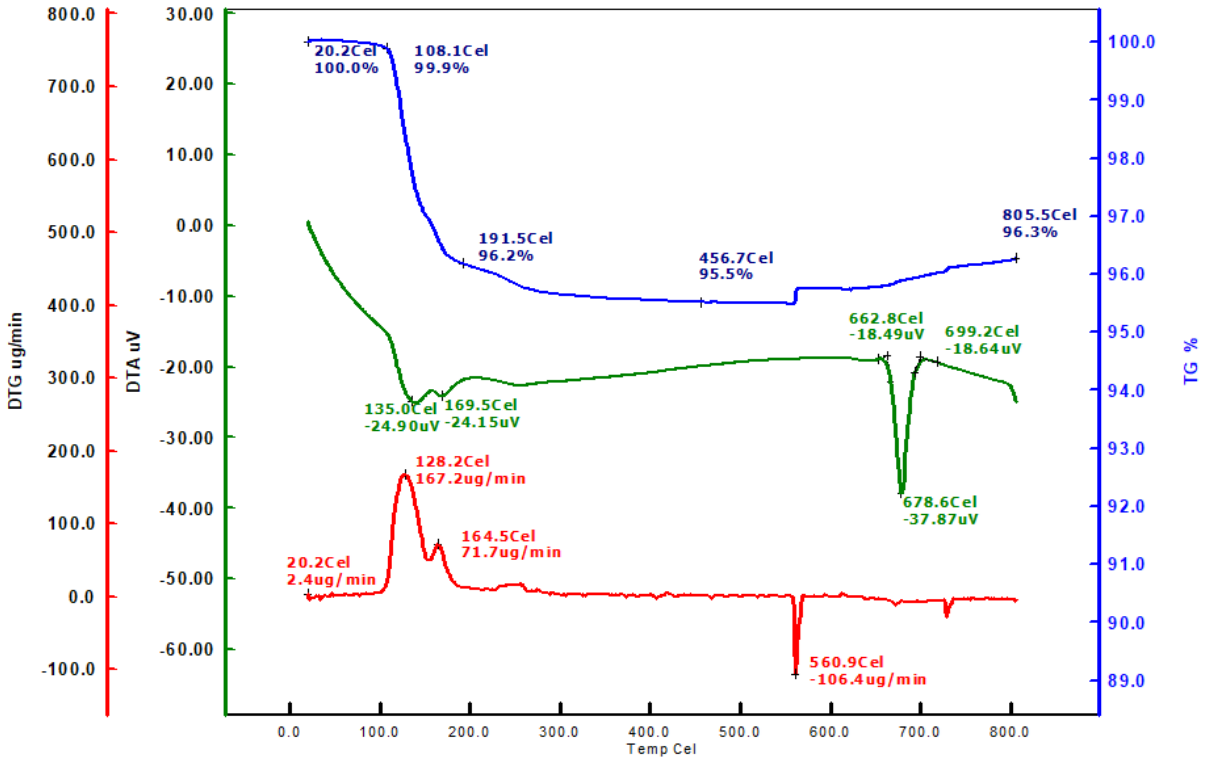

Figure 4.1 Thermogravimetric Analysis

If we observe the blue thermogravimetric analysis curve in Figure 4.1 , we can notice significant weight loss at about 100 ℃. At this temperature , the boric acid powder which is known as orthoboric acid loses water molecule to give metaboric acid which on heating 160℃ give tetraboric acid. From 162℃ to 430 ℃ , tetraboric acid is converted to boron trioxide i.e. the anhydrous form of orthoboric acid.

At 100 ℃ , $4H_3BO_3 = 4HBO_2 + 4H_20$

At 160 ℃ , $4HBO_2 = H_2B_40_7 + H_20$

From 162 ℃ to 430 ℃, $H_2B_40_7 = 2B_20_3 + H_20$

Near 550℃ , the curve indicates weight gain due to oxidation. Weight gaining started with the formation of in situ reinforcements. The probable in-situ reinforcements formation reactions are:

From 550 ℃ to 650 ℃ , $2Al + B_2O_3 = \gamma Al_2O_3 + 2B$

Near 500 ℃ , $Al + 2B = AlB_2$

From 550 ℃ to 600 ℃,

$3TiO_2 + 2Al = 3TiO + \gamma\ Al_2O_3$

$3TiO + 2Al = 3Ti + \gamma Al_2O_3$

$Ti + Al = TiAl_3$

$Ti + 2B = TiB_2$

So, the probable in-situ reinforcements are γAl_2O_3 , $TiAl_3$, TiB_2 , AlB_2 .

4.1.2 Derivative Thermogravimetry Analysis

The red derivative thermogravimetry curve in Figure 4.1 provides information about the onset and completion of reactions that occur during sintering. Boric acid decomposition initiates at approximately 110℃ and finishes at around 162℃. The formation of in-situ reinforcements, on the other hand, commences at about 550℃ and 750℃. Based on these findings, the sintering temperature range of 600℃ to 800℃ was selected.

4.1.3. Differential Thermal Analysis of Green Sample

The green curve displayed in Figure 4.2 illustrates the Differential Thermal Analysis (DTA) results of the green sample, covering a temperature range from 50°C to 800°C.

The first peak, indicated by 1, represents the melting of boric acid at around 100°C. The second peak, indicated by 2, occurs at approximately 150°C and corresponds to the decomposition of boric acid. The third peak, indicated by 3, occurs at 660°C and corresponds to the melting of aluminum. The dashed line on the graph indicates the range of the exothermic peak, which occurs between 550°C - 650°C and is attributed to the formation of reinforcements.

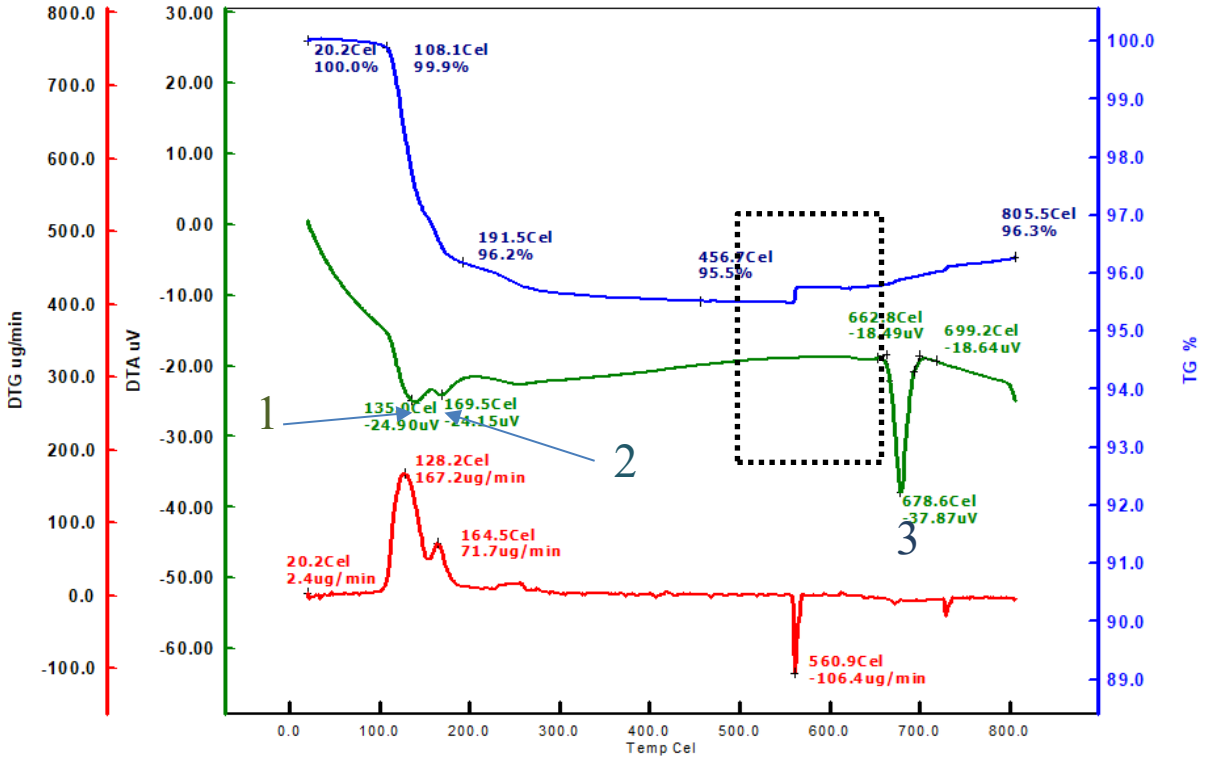

Figure 4.2 Differential Thermal Analysis

4.2 X-Ray Diffraction Analysis

4.2.1. XRD Analysis for Temperature Variation

The XRD results show that the sintering temperature plays a critical role in the formation of in-situ reinforcements in AMMC.

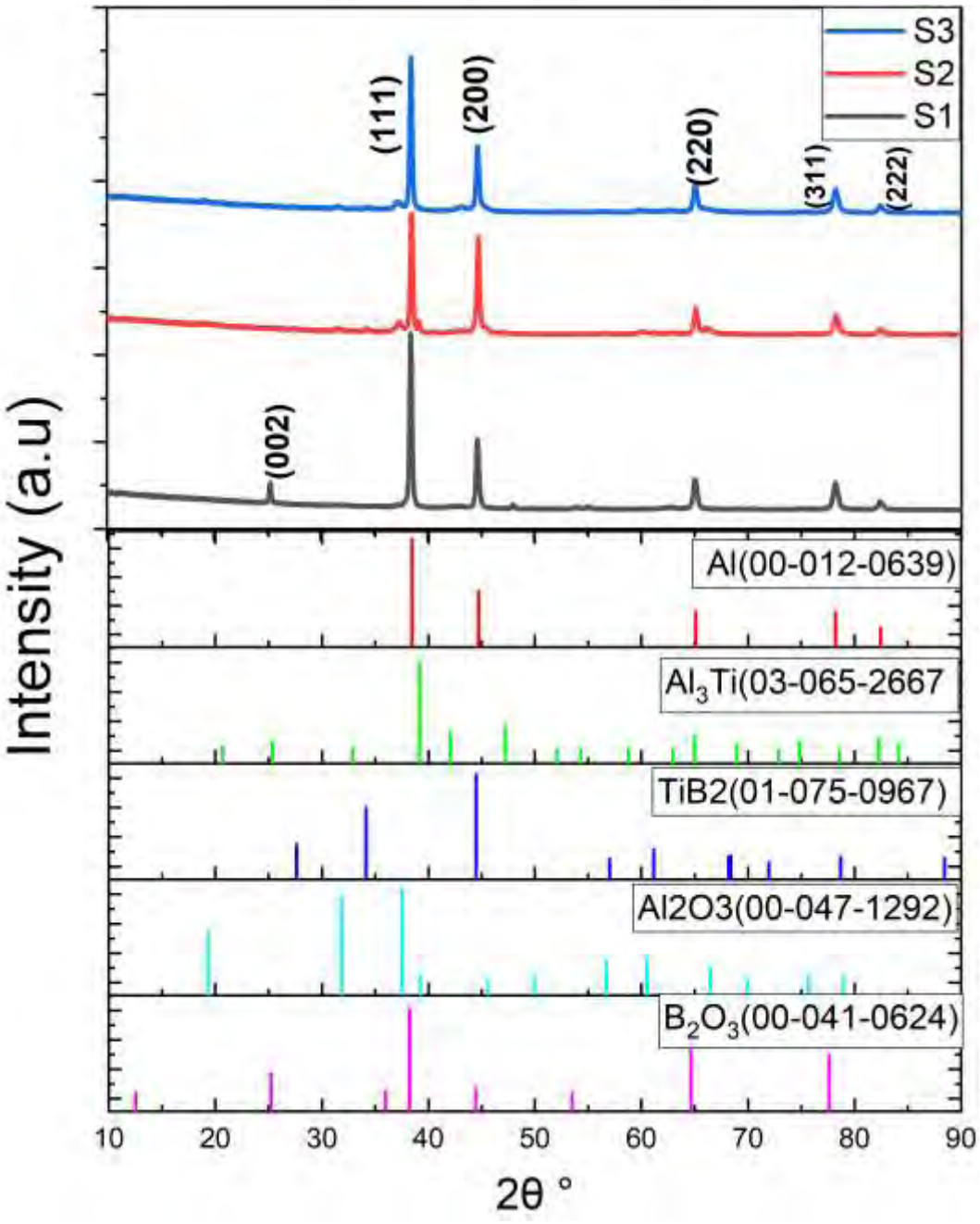

Figure 4.3 XRD Analysis at three different sintering temperature 600°C, 700°C, 800°C.

In Figure 4.3 ,the X-ray diffraction (XRD) results reveal that the sintering temperature significantly impacts the formation of in-situ reinforcements in AMMCs. The data was obtained by scanning an angular range of 10° to 90° using X- ray diffractometer (Bruker), with a fixed composition of the composites. The three samples, S1, S2, and S3, were subjected to sintering temperatures of 600℃, 700℃, and 800℃, respectively.

The XRD data was presented in Figure 4.3 that compares the XRD peaks of the samples with reference peaks. The observed peaks in the pattern, including (111), (200), (220), (311), and (222), indicate the presence of Aluminium in all three samples. However, the peak at 2θ = 25.275℃, which is only present in S1, suggests the existence of B_2O_3. This peak's absence in S3 indicates that B_2O_3 reacts with aluminium to produce in-situ reinforcements.

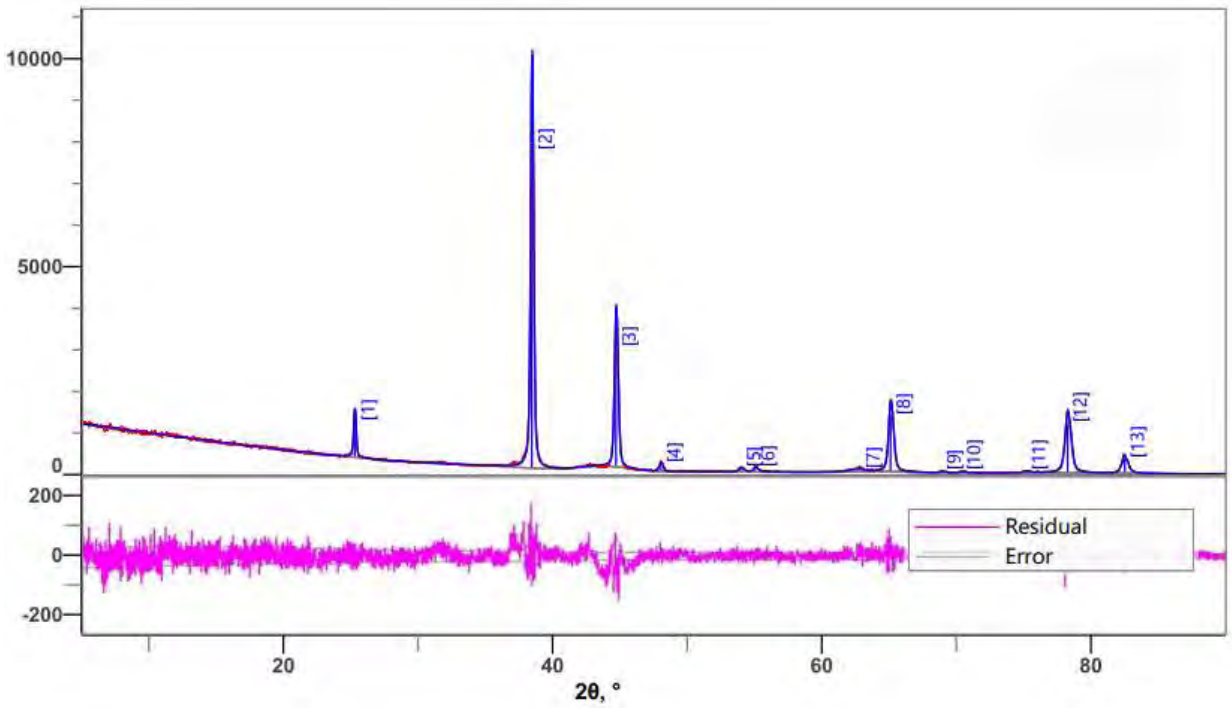

Figure 4.4 XRD peak analysis of S1

According to XRD analysis shown in Figure 4.4 , it was found that sintering at 600℃ led to the formation of crystalline aluminium matrix. The in-situ phases observed in the sample were γAl_2O_3, B_2O_3, and TiAl. Peaks at 3, 4, 11, and 13 indicated the presence of γAl_2O_3, while peaks at 1, 2, 3, 5, 6, 8, 12, and 13 indicated the presence of B_2O_3. Peaks at 2, 3, 8, 12, and 13 indicated the presence of TiAl, which had a tetragonal structure [62] .

So , when sintering temperature is 600℃ , the matrix is Aluminium and the major in-situ phases are B_2O_3 , γAl_2O_3 and TiAl structure.

B_2O_3 crystallizes in the trigonal P3_121 space group. B^{3+} is bonded in a trigonal planar geometry to three O^{2-} atoms. [58].

Crystal System	**Trigonal**
Lattice System	Hexagonal
Hall Number	P 31 2"
International Number	152
Symbol	P3_12$\bar{1}$
Point Group	32

The structure of γ-Al_2O_3 has historically been described as a spinel similar to a traditional AB_2O_4 spinel, where the oxygen atoms are arranged in a cubic close-packed lattice while the A and B cations occupy the tetrahedral and octahedral interstitial sites (spinel sites) of the lattice, respectively [59], [60]. However, in the case of spinel γAl_2O_3, 8/3 cation vacancies must be introduced into each unit cell to maintain the correct stoichiometry [61].

(TiAl) has the tetragonal $L1_0$ structure, point Group 4/mmm [62].

Crystal System	Tetragonal
Lattice System	Tetragonal
Hall Number	-P 4 2
International Number	123
Symbol	P4/mmm
Point Group	4/mmm

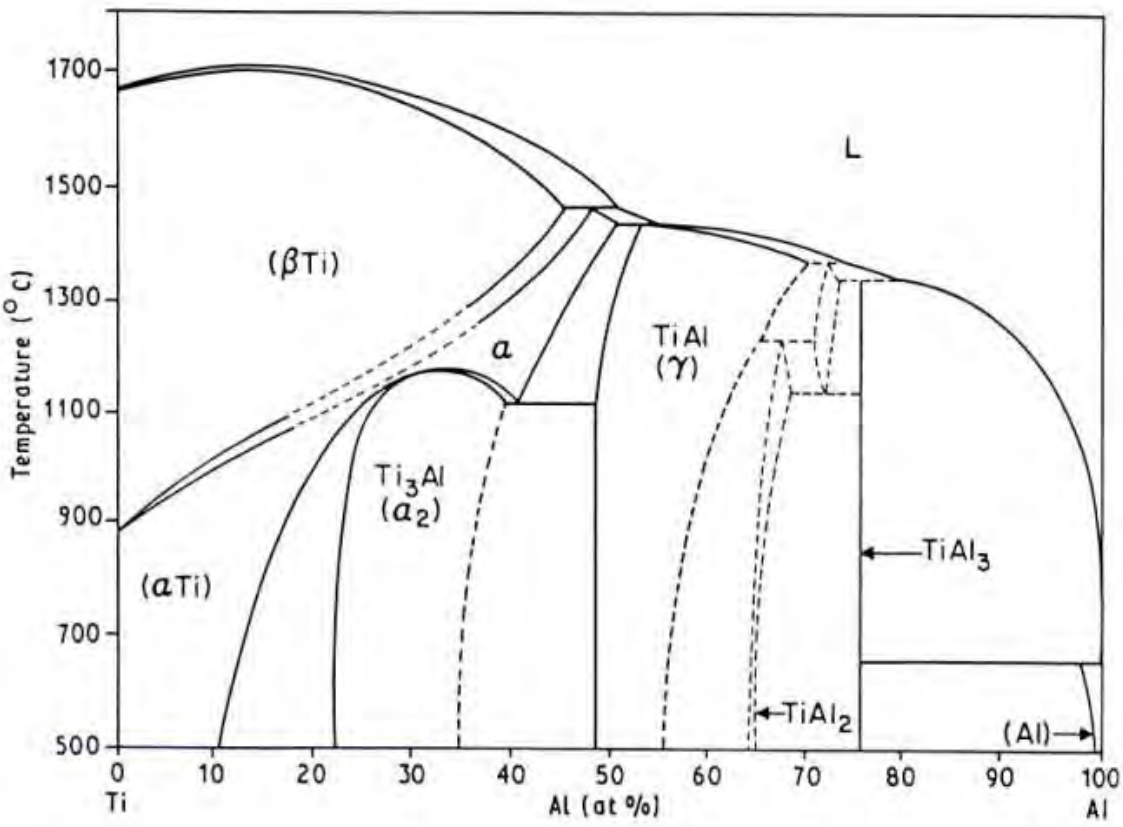

Figure 4.5 Schematic binary Ti-Al phase diagram [63]

In the Ti-Al binary phase diagram shown in Figure 4.5 , TiAl (γ) phase was found [63].

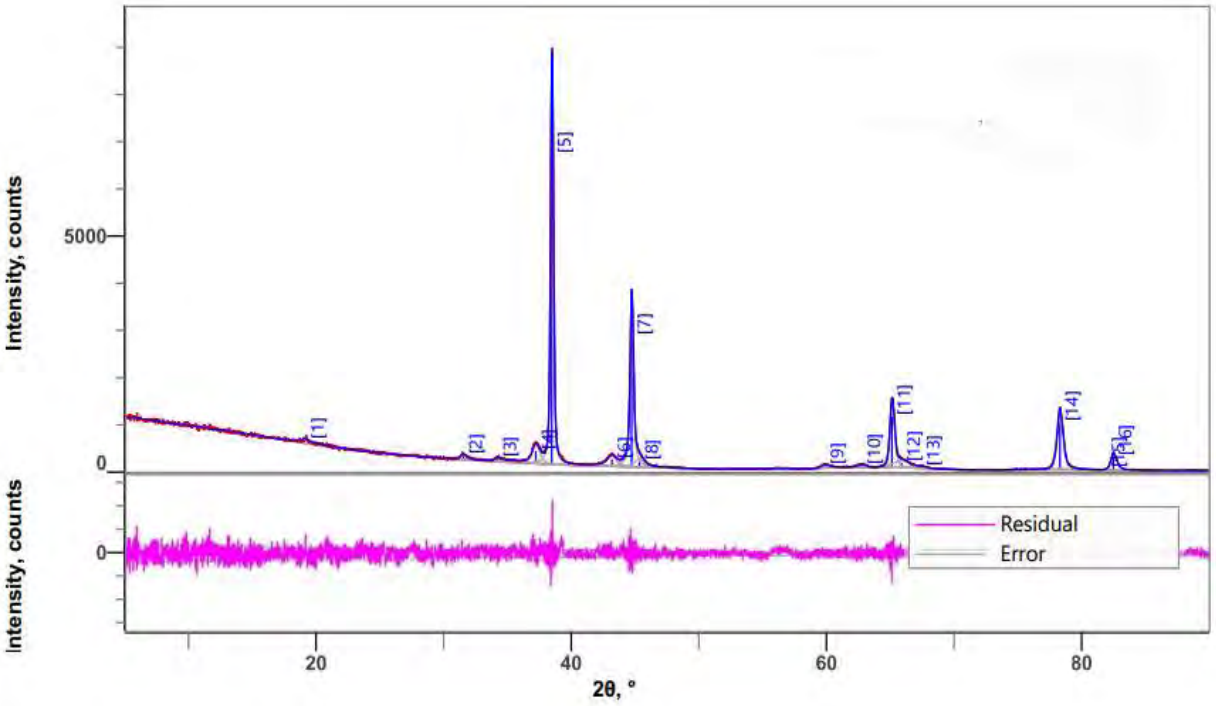

Figure 4.6 XRD peak analysis of S2

The XRD analysis conducted on sample S2 shown in Figure 4.6 revealed several important findings. Firstly, the presence of aluminium was confirmed by the observed peaks at 5, 7, 11, and 14.

Secondly, the sample was found to contain in-situ reinforcements of TiAl, as evidenced by the peaks observed at 2, 5, 7, 11, 14, and 16. The presence of Al_2O_3 was also detected, confirmed by the peaks at 2, 4, 7, 10, and 15.

Thirdly, the peaks at 7 and 13 suggested the existence of AlB_2.

Overall, the XRD analysis of sample S2 demonstrated the presence of TiAl, Al_2O_3 and AlB_2 as the primary in-situ reinforcements.

AlB_2 is hexagonal omega structure structured and crystallizes in the hexagonal P6/mmm space group [64].

Crystal System	Hexagonal
Lattice System	Hexagonal
Hall Number	-P 6 2
International Number	191
Symbol	P6/mmm
Point Group	6/mmm

In Figure 4.7 ,the XRD analysis conducted on the sample S3 sintered at 800℃ revealed interesting findings.

Firstly, the number of peaks had increased compared to samples S1 and S2, suggesting that the higher sintering temperature resulted in more in-situ reinforcements.

The presence of aluminium was confirmed by the observed peaks at 6, 10, 16, 21, and 22. The peaks at 3, 6, 9, 11, 17, 20, and 22 indicated the presence of TiAl, while Al_2O_3 was detected and confirmed by the peaks at 1, 6, 10, 16, 19, 21, and 22.

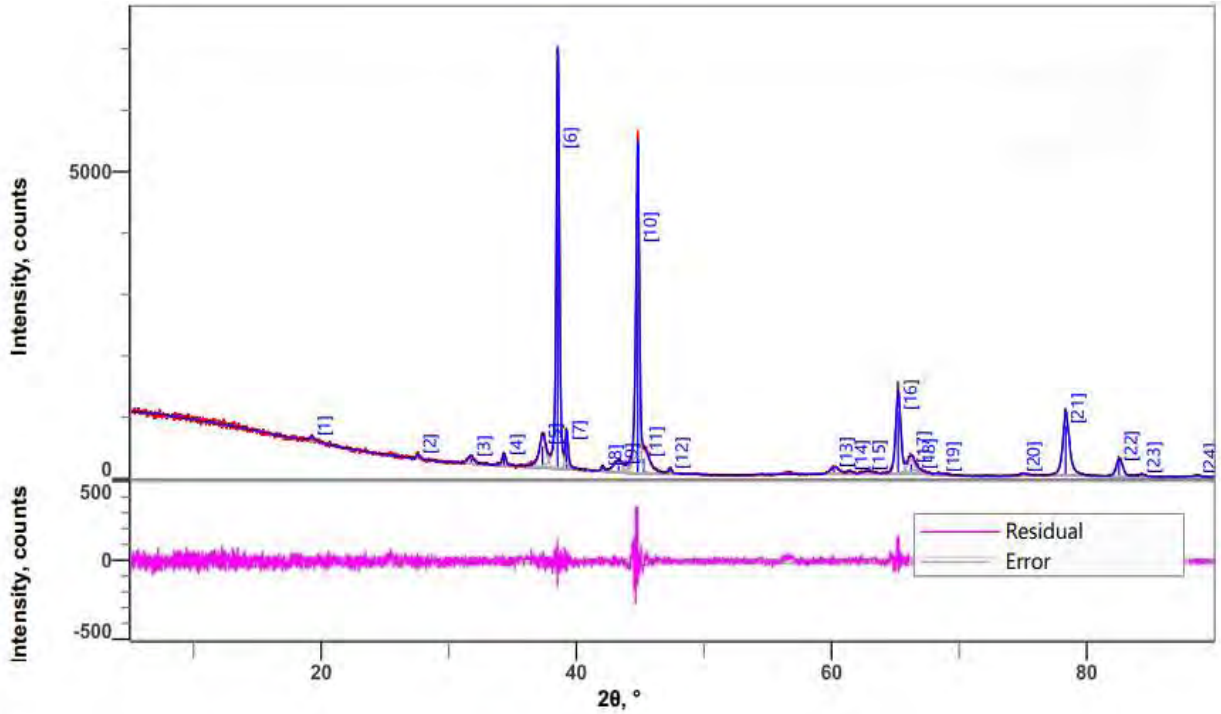

Figure 4.7 XRD peak analysis of S3

Furthermore, the peaks at peaks at 2, 4, 10, 14, 19, and 24 indicated the presence of TiB_2. This suggests that TiB_2 is present as an in-situ reinforcement in the sample sintered at 800℃ , which is the most stable reinforcement found at this temperature.

Importantly, the absence of B_2O_3 peaks at 800℃ indicated that it had completely reacted with aluminium to produce γ Al_2O_3.

In summary, the XRD analysis of the sample sintered at 800℃ showed the presence of several in-situ reinforcements, including TiB_2, TiAl, and γ Al_2O_3.

$$2Al + B_2O_3 = \gamma Al_2O_3 + 2B$$

$$3TiO_2 + 2Al = 3TiO + \gamma\ Al_2O_3$$

$$3TiO + 2Al = 3Ti + \gamma Al_2O_3$$

$Ti + Al = TiAl$

$Ti + 2B = TiB_2$

TiB_2 is hexagonal omega structure structured and crystallizes in the hexagonal P6/mmm space group. [65]

Crystal System	Hexagonal
Lattice System	Hexagonal
Hall Number	-P 6 2
International Number	191
Symbol	P6/mmm
Point Group	6/mmm

The results of the XRD analysis show that the sintering temperature has a significant impact on the in-situ reinforcements. The higher sintering temperature at 800°C resulted in the presence of TiB_2 reinforcement. The results emphasize the importance of controlling the sintering temperature in achieving desired in-situ reinforcements.

4.2.2. XRD Analysis for Different External Aluminium Percentages

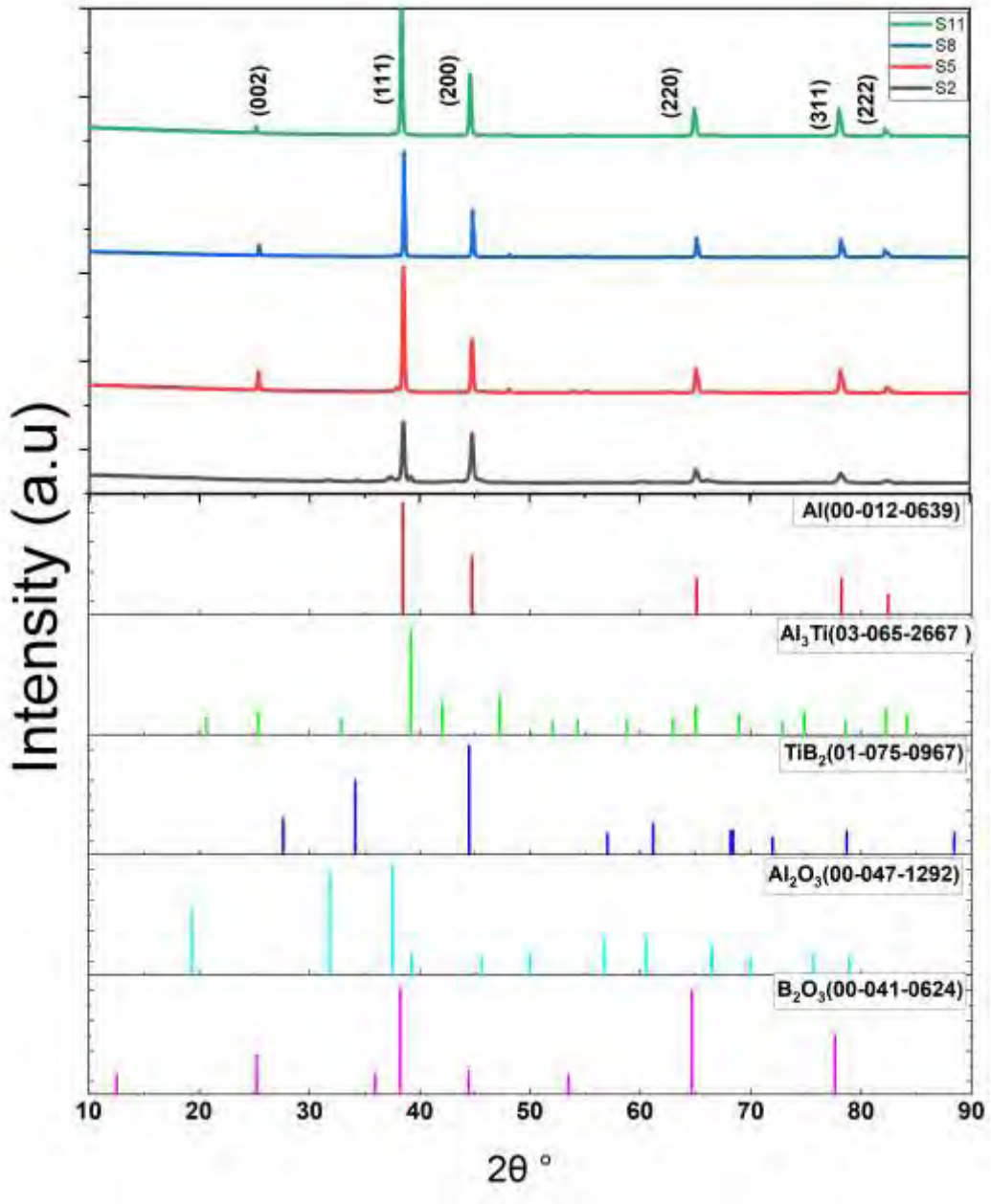

Figure 4.8 The XRD pattern comparison for same sintering temperature but different external aluminium percentages

In Figure 4.8 , the sintering temperature was kept constant at 700°C for four samples, namely S2, S5, S8, and S11. These samples were prepared with varying percentages of external Aluminium, specifically 0%, 25%, 50%, and 75%, respectively. While most of the XRD peaks in these samples are observed at the same positions, the intensity of the peaks varies due to the changes in the percentage of external Aluminium.

The XRD analysis of sample S2 (external aluminium 0%) demonstrated in Figure 4.6 the presence of TiAl, Al_2O_3 and AlB_2 as the primary in-situ reinforcements.

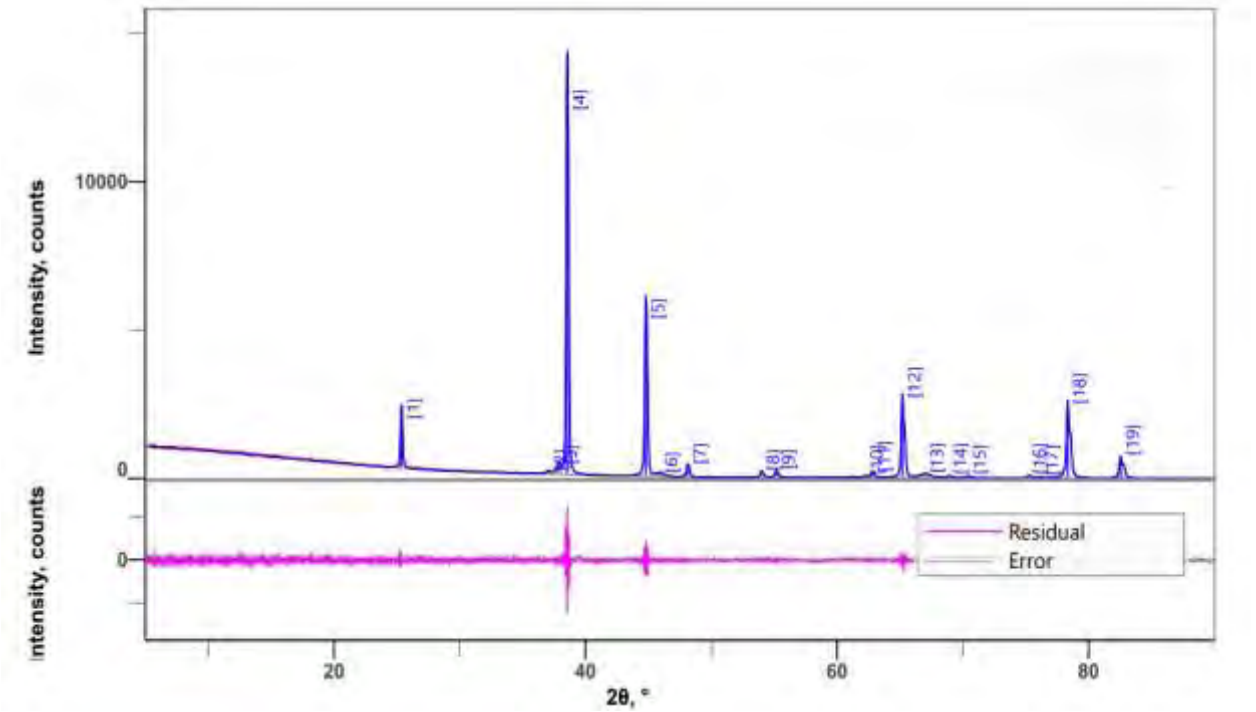

Figure 4.9 XRD peak analysis of S5

In Figure 4.9 , the XRD analysis of sample S5 (external aluminium 25%) reveals the presence of multiple reinforcements in aluminium matrix including aluminum oxide (Al_2O_3), titanium aluminum (TiAl), aluminum boride (AlB_2), and boric oxide (B_2O_3). The diffraction peaks observed at 4, 5, 12, 18, and 19 suggest the presence of aluminum oxide, while the peaks at 4, 12, 14, and 19 indicate the presence of aluminum titanium. Moreover, the peaks at 6, 11, and 15 suggest the presence of aluminum boride, and the peaks at 1, 4, 5, 8, 12, 18, and 19 indicate the presence of boric oxide.

Based on XRD analysis shown in Figure 4.10 , sample S8 (external aluminium 50%) contains aluminum, boric oxide (B_2O_3), aluminum oxide (Al_2O_3), titanium aluminum (TiAl), and aluminum boride (AlB_2). The peaks at 3, 4, 10, and 16 indicate the presence of aluminum and aluminum oxide, while the peaks at 1, 4, 6, 10, and 16 indicate the presence of boron oxide. Furthermore, the peaks at 3, 10, and 11 indicate the presence of titanium aluminum, and the peaks at 9 and 12 indicate the presence of aluminum boride.

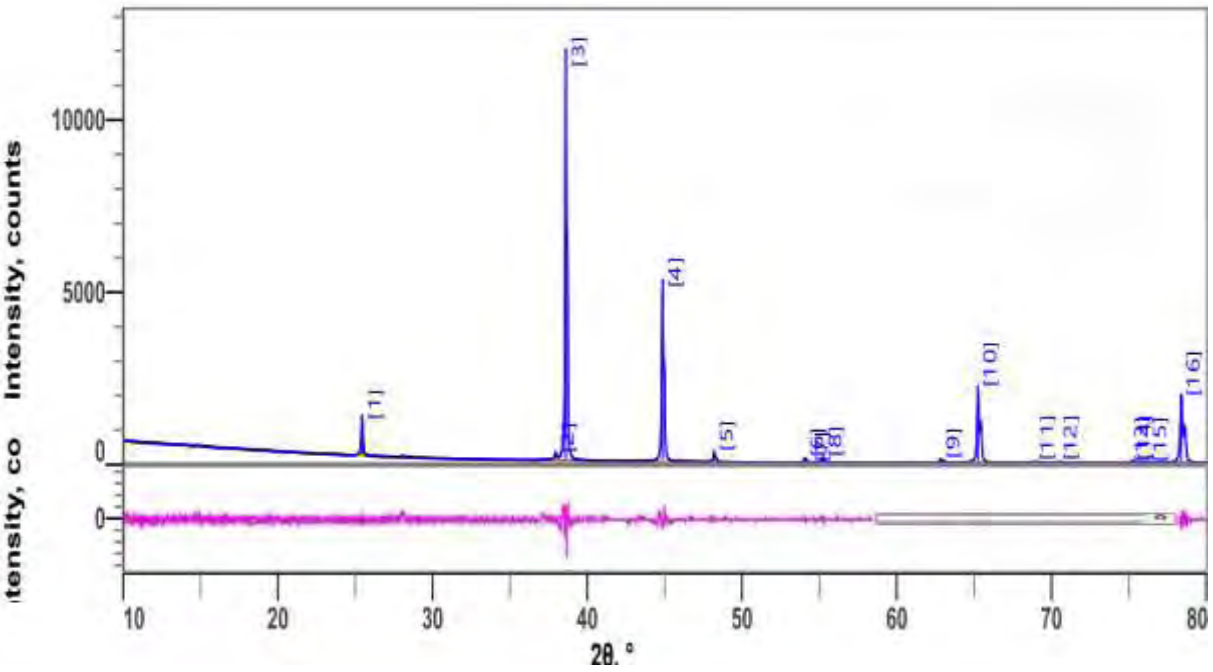

Figure 4.10 XRD peak analysis of S8

Sample S11 XRD analysis is shown in Figure 4.11 and the results indicate the presence of aluminum, aluminum oxide (Al_2O_3), and titanium aluminum (TiAl). The peaks at 3, 4, 9, 14, and 15 indicate the presence of titanium aluminum, while the peaks at 3, 6, and 15 indicate the presence of aluminum oxide.

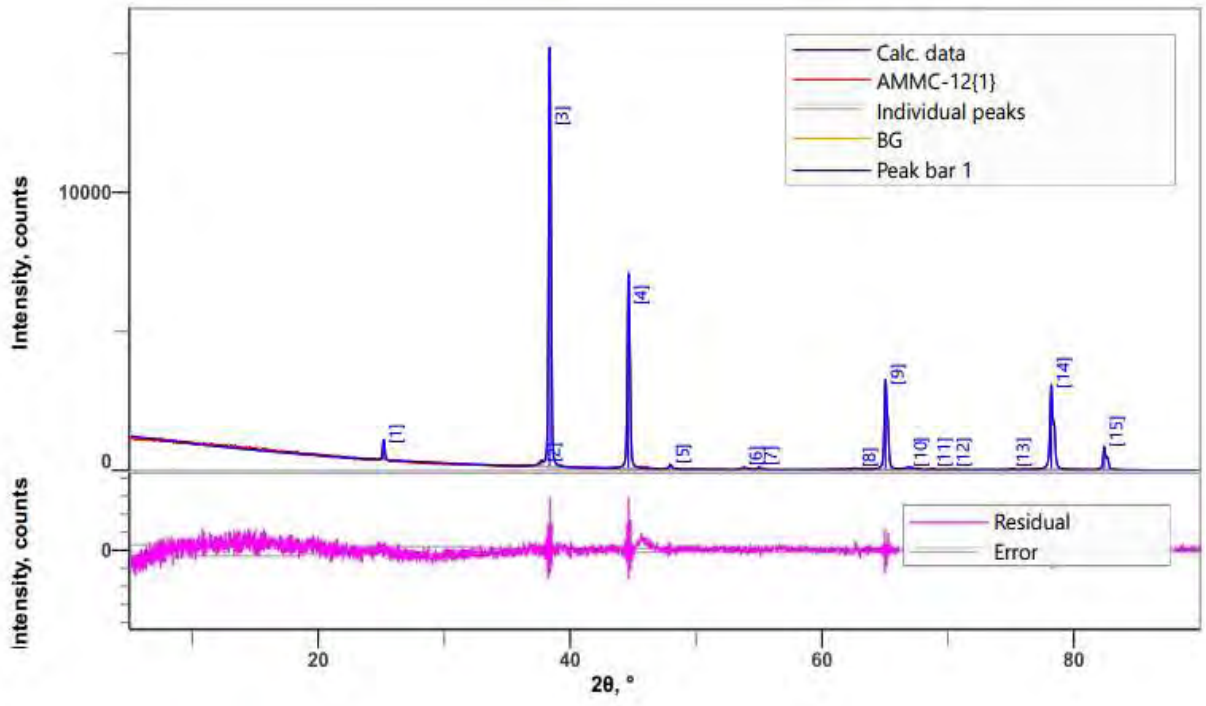

Figure 4.11 XRD peak analysis of S11

4.2.3 XRD Result Comparison Table

Table 4.1 XRD Results Analysis of S1, S2, S3 (sintering temperature variable)

Sample No	Composition	Sintering Temperature	Phases present			
S1	H_3BO_3 = 7.78 % TiO_2 = 15.07 % Milled Al = 77.1 5% Unmilled Al = 0 %	600℃	Al (matrix)	γAl_2O_3	B_2O_3	TiAl
S2		700℃	Al (matrix)	γAl_2O_3	AlB_2	TiAl
S3		800℃	Al (matrix)	γAl_2O_3	TiB_2	TiAl

Table 4.2 XRD Results Analysis of S2 , S5, S7 and S11 (composition variable)

Sample No	Composition	Sintering Temperature	Phases present			
S2	H_3BO_3 = 7.78 % TiO_2 = 15.07 % Milled Al = 77.1 5% Unmilled Al = 0 %	700℃	Al (matrix)	γAl_2O_3	AlB_2	TiAl
S5	H_3BO_3 = 5.84 % TiO_2 = 11.30 % Milled Al = 57.86 % Unmilled Al = 25 %		Al (matrix)	γAl_2O_3	AlB_2 , B_2O_3	TiAl
S7	H_3BO_3 = 3.89 % TiO_2 = 7.54 % Milled Al = 38.58 % Unmilled Al = 50 %		Al (matrix)	γAl_2O_3	AlB_2 , B_2O_3	TiAl
S11	H_3BO_3 = 1.95 % TiO_2 = 3.77 % Milled Al = 19.29 % Unmilled Al = 75 %		Al (matrix)	γAl_2O_3		TiAl

4.3 Morphological and Elemental Analysis

The samples were prepared initially to investigate their morphology and microstructure.

4.3.1 Optical Microstructure Analysis

All microstructures analyzed using optical microscopy are presented at two different magnifications.

4.3.1.1 Sintering Temperature Effect

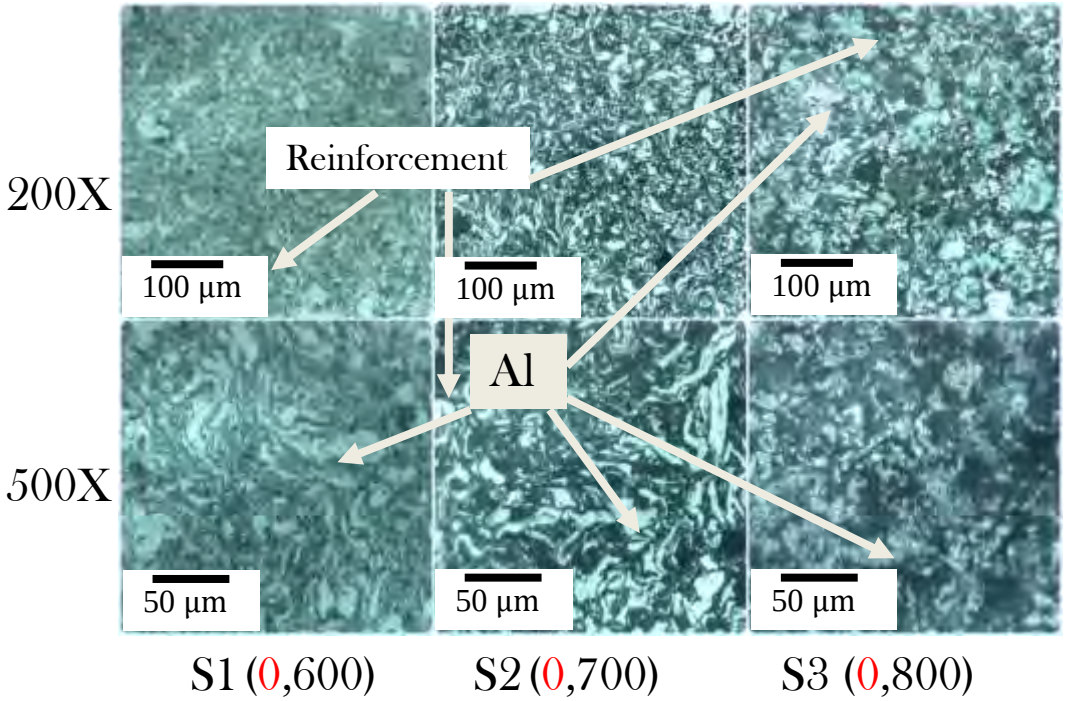

Figure 4.12 Optical microstructure comparison of S1, S2 and S3.

Figure 4.12 illustrates the microstructural changes observed at different temperatures sintered samples S1, S2, and S3, all of which have an external aluminum content of 0%. As a result, these samples are considered to be single matrix composites. The micrographs show an increase in the amount of reinforcements present in the aluminum matrix as the temperature increases.

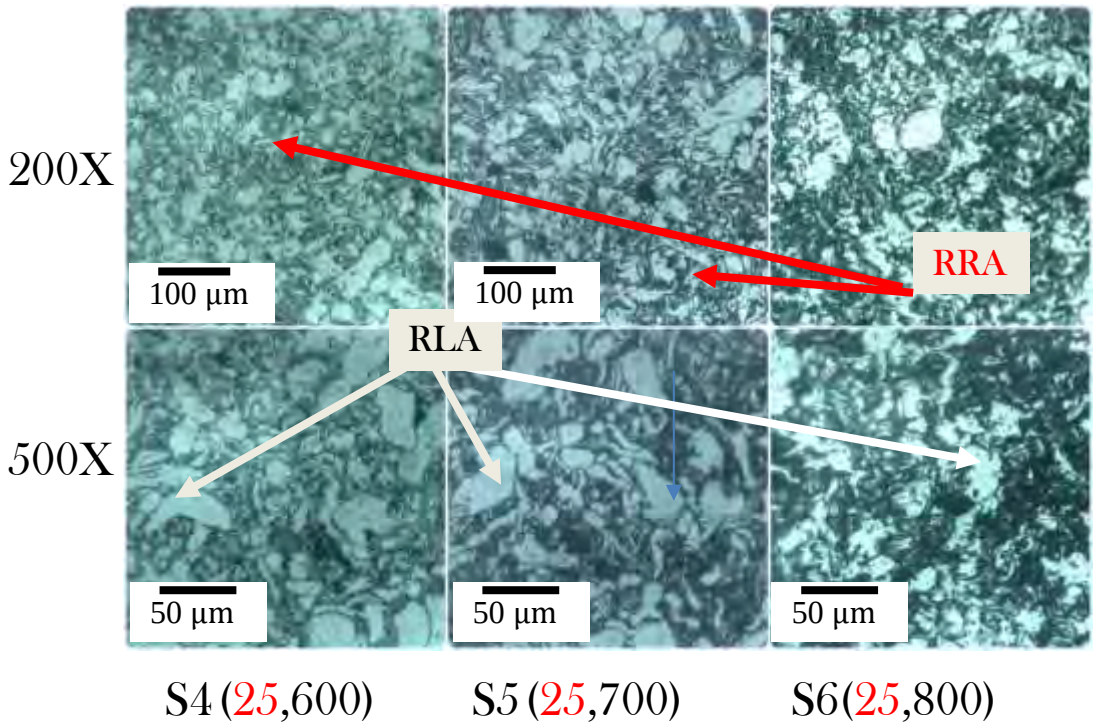

Figure 4.13 Optical microstructure comparison of S4, S5 and S6.

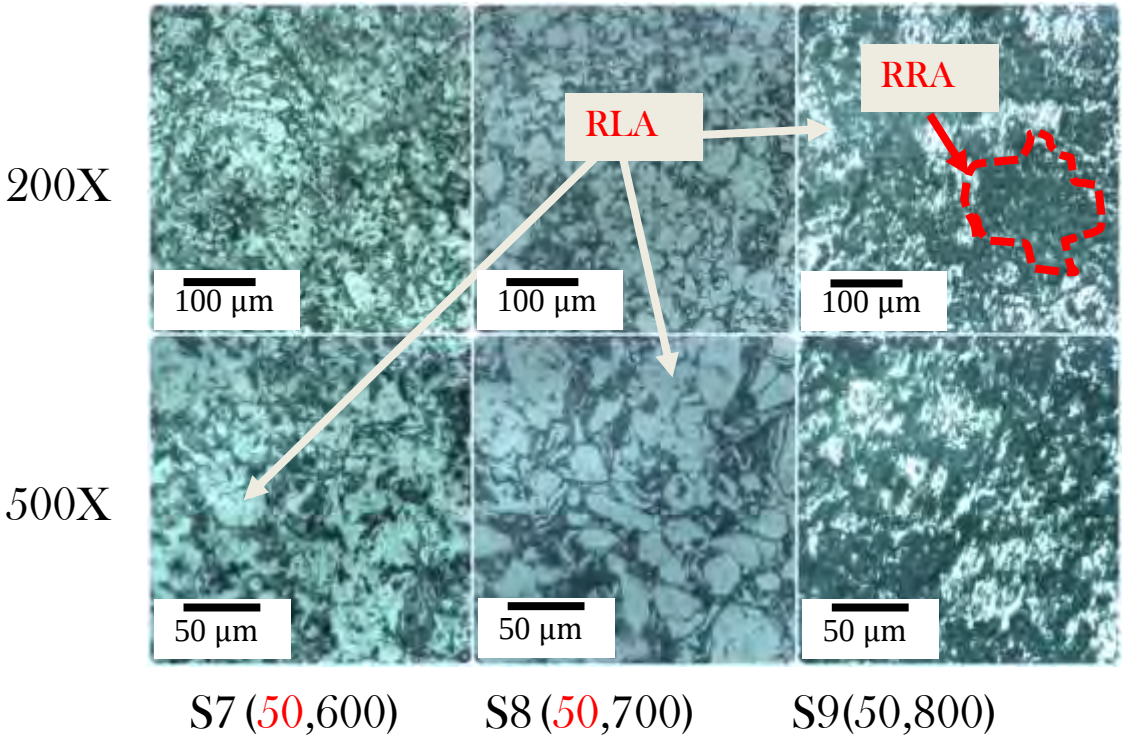

Figure 4.14 Optical microstructure comparison of S7, S8 and S9.

Figure 4.13 shows a microstructure with 25% external aluminum added to the initial mixture of 75%. The microstructure is divided into two regions: reinforcements lean area (RLA) and reinforcements rich area (RRA). RRA appears to have a normal microstructure like single matrix composites, while RLA represents the external aluminum portion. The composite region with a distinct inner matrix is present in localized regions within the microstructure, separated by an outer ductile unreinforced matrix. The inner matrix is rich in reinforcements. In the Figure 4.13, the whitish portions represent the unreinforced outer matrix, while the composite regions with reinforcements in the matrix are noted as RRA.

In Figure 4.14, as the percentage of external aluminum increases from 25% to 50%, the amount of the outer ductile unreinforced matrix also increases from 25% to 50%. At a sintering temperature of 800℃, significant changes in the microstructure are observed. The Figure 5.14 shows that the amount of in-situ reinforcements increases with increasing sintering temperature, leading to an increase in the RRA portion at 800℃.

In Figure 4.15, with an external aluminum percentage of 75%, the unreinforced external matrix of aluminum is interconnected. Sintering temperature plays the most significant role in the microstructure as well properties of these composites.

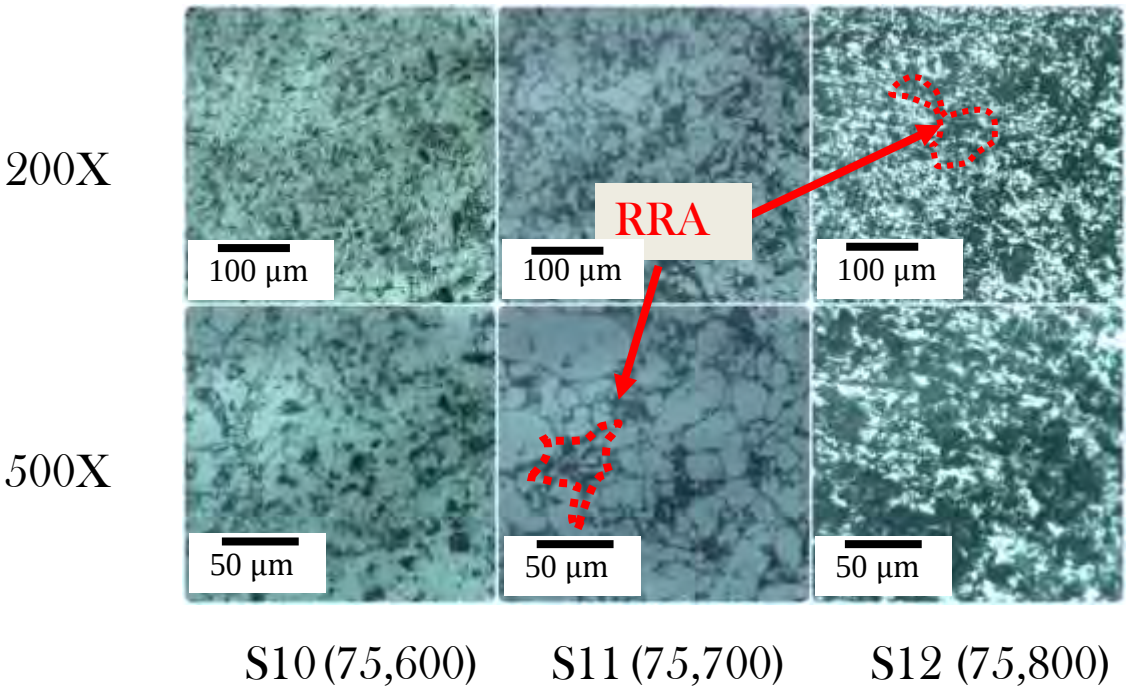

Figure 4.15 Optical microstructure comparison of S10, S11 and S12.

4.3.1.2 External Aluminium Percentage Effect

To prepare the dual matrix, the external Aluminium percentage is categorized into four groups ranging from 0% to 75%, including 0%, 25%, 50%, and 75%. The following figures illustrate how the morphology changes with increasing external aluminium percentages at the same temperature.

Figure 4.16 shows the change in microstructure with varying external aluminium percentages at a sintering temperature of 600℃. As the external aluminium percentage increases, there is a significant increase in the reinforcement lean area (RLA).

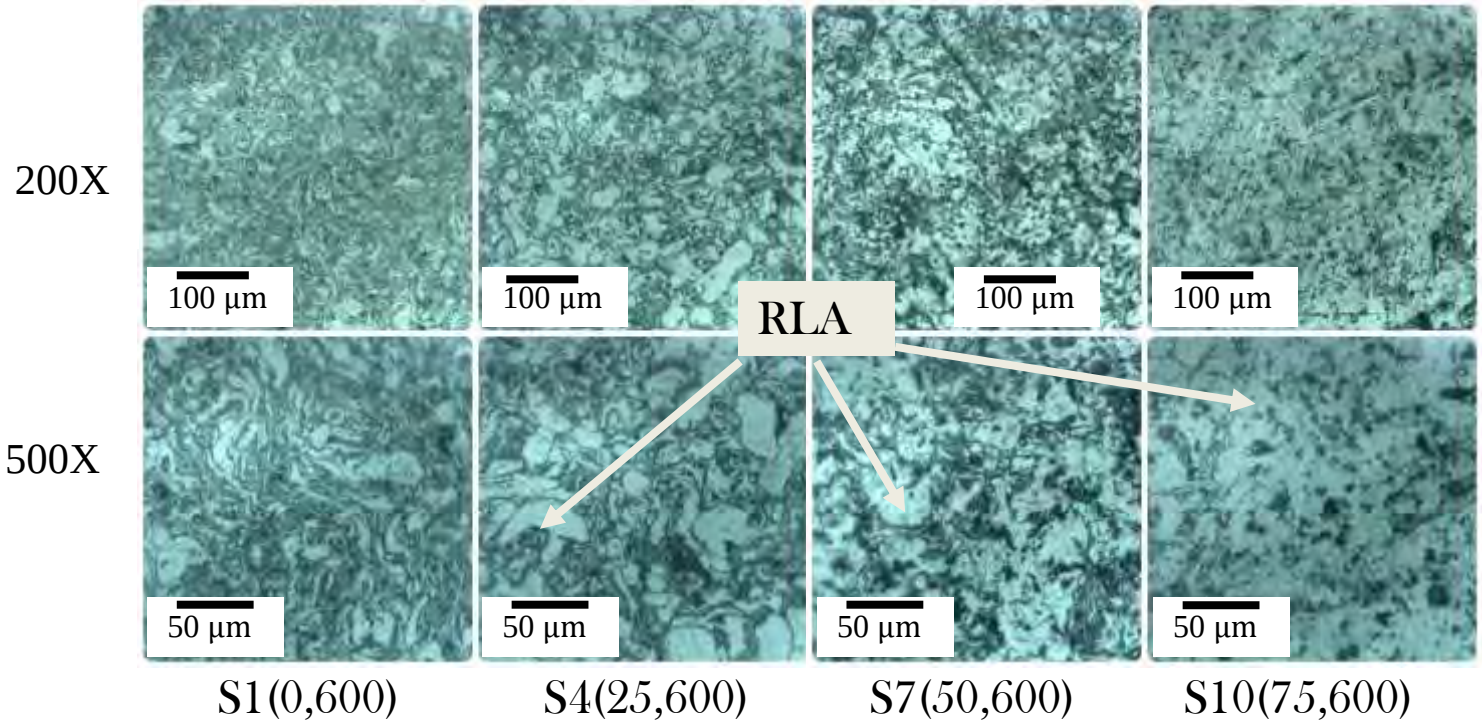

Figure 4.16 Microstructure analysis for samples sintered at 600℃

Figure 4.17 demonstrates that the morphology changes with increasing aluminium percentages of samples sintered at 700℃. At lower external percentages of aluminium, the external matrix is discrete and not connected, while at higher percentages of external aluminium, the outer matrix becomes interconnected.

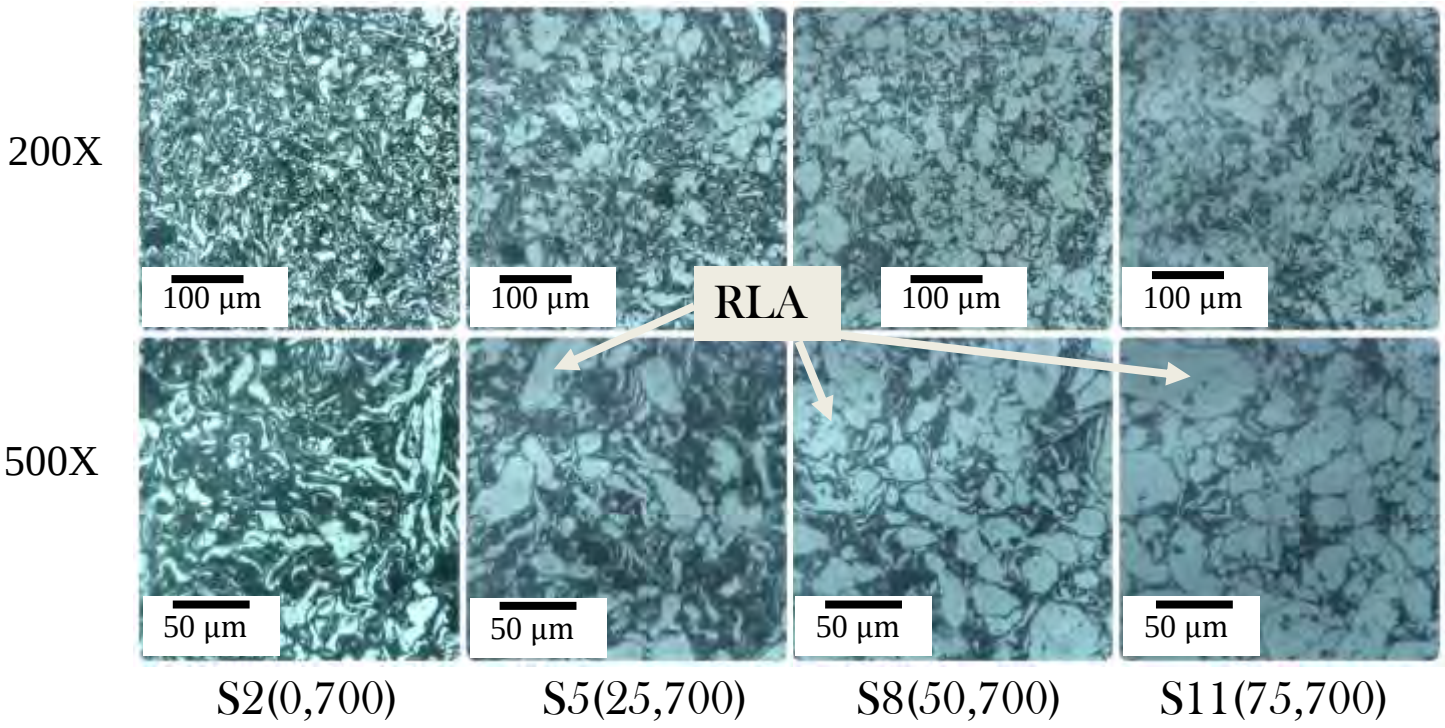

Figure 4.17 Microstructure analysis for samples sintered at 700℃

In Figure 4.18, there is a sharp difference in morphology when samples are sintered at 800℃ compared to the previous samples sintered at 600℃ and 700℃. XRD results confirmed that the in-situ reinforcements are higher at 800℃ compared to the other two temperatures. The Figure 4.18 shows that the area rich in reinforcements accumulates more reinforcements.

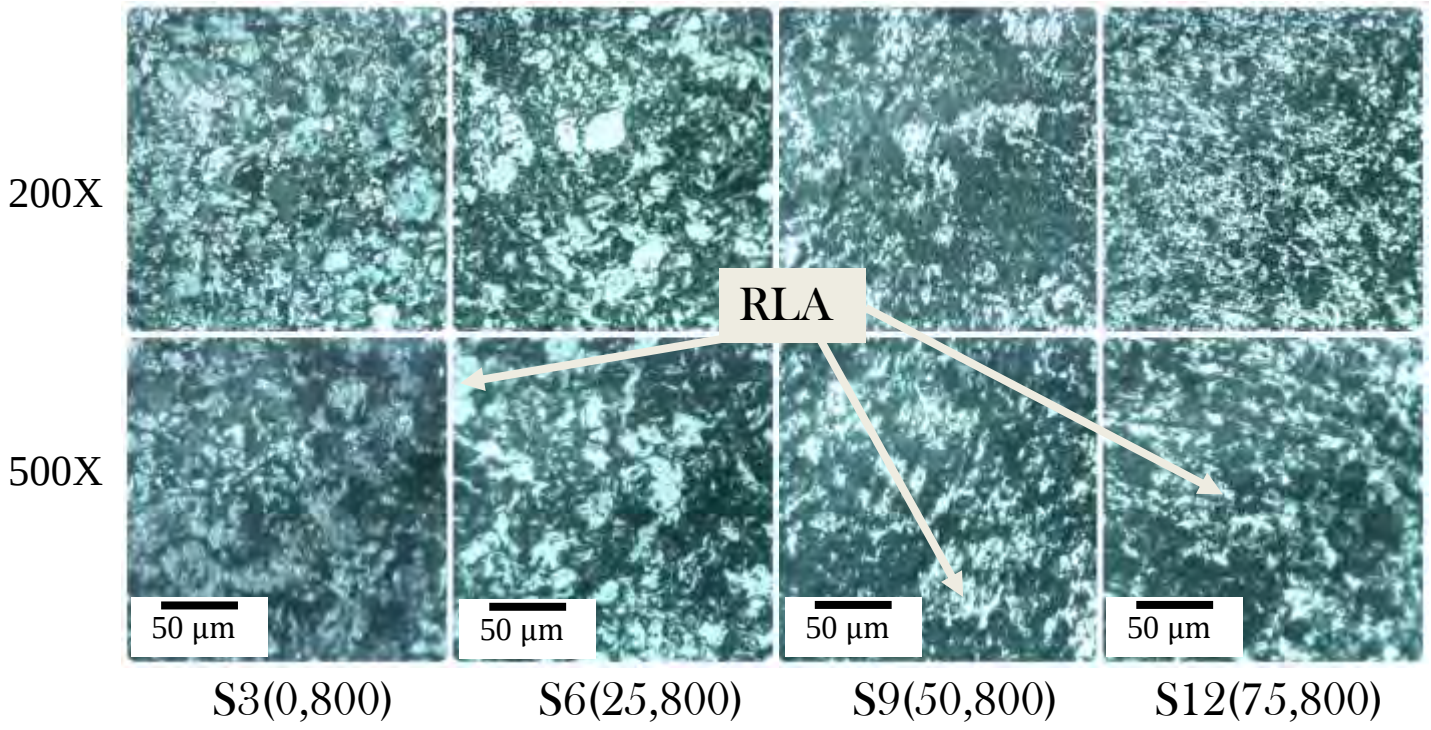

Figure 4.18 Microstructure analysis for samples sintered at 800℃

4.3.2 Field Emission Scanning Electron Microstructure Analysis

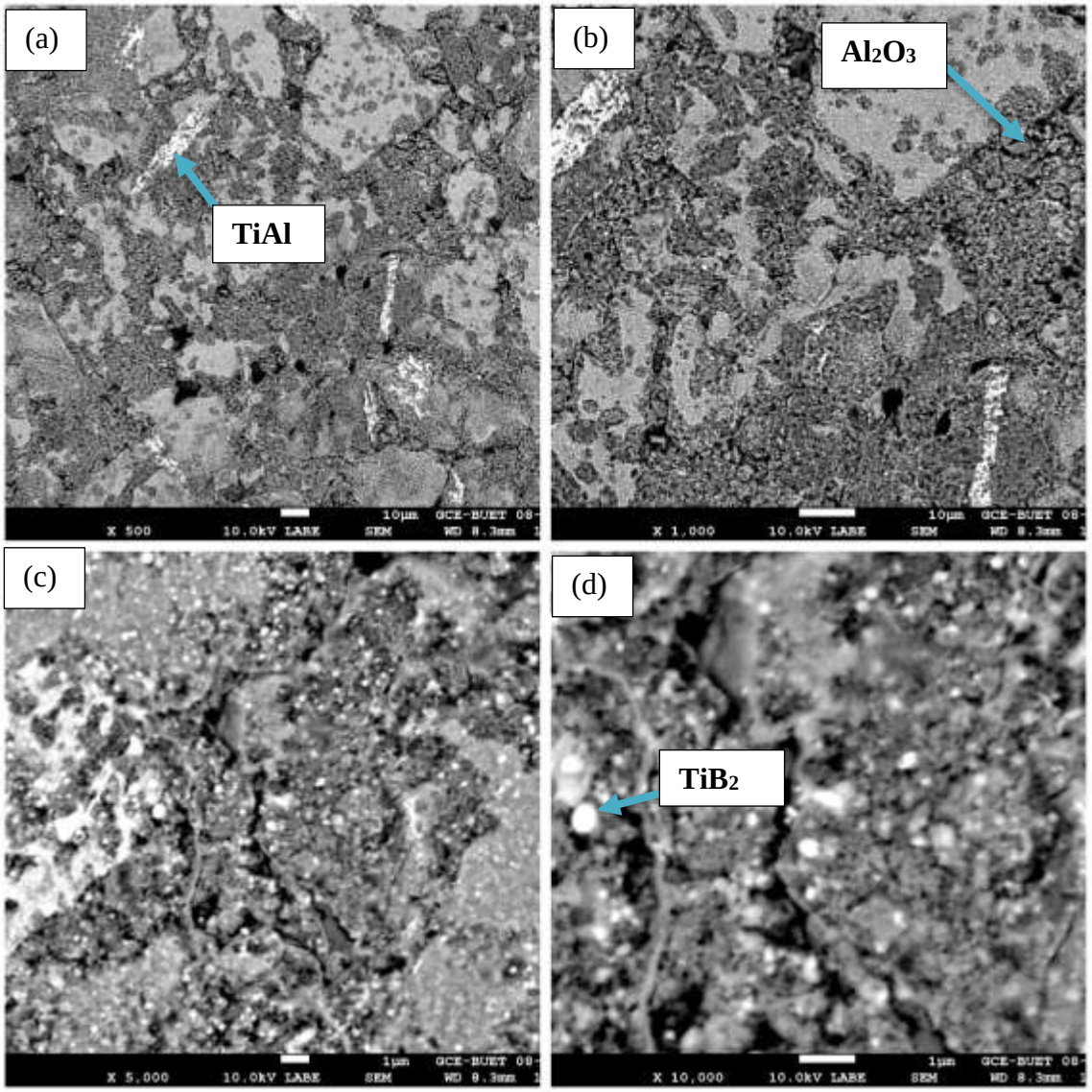

Figure 4.19 S3 SEM images (a) x 500 (b) x 1,000 (c) x 5,000 (d) x 10,000

The S3 sample underwent sintering at 800°C without the addition of external aluminium. The above Figure 4.19 shows that the aluminium matrix contains TiAl, Al_2O_3, and TiB_2 particles that are distributed within it.

According to Figure 4.20 , the EDS analysis of the S3 sample matrix shows an aluminium percentage of 73.36%. In the matrix portion , aluminium is not 100%. So, the matrix is not completely devoid of reinforcements.

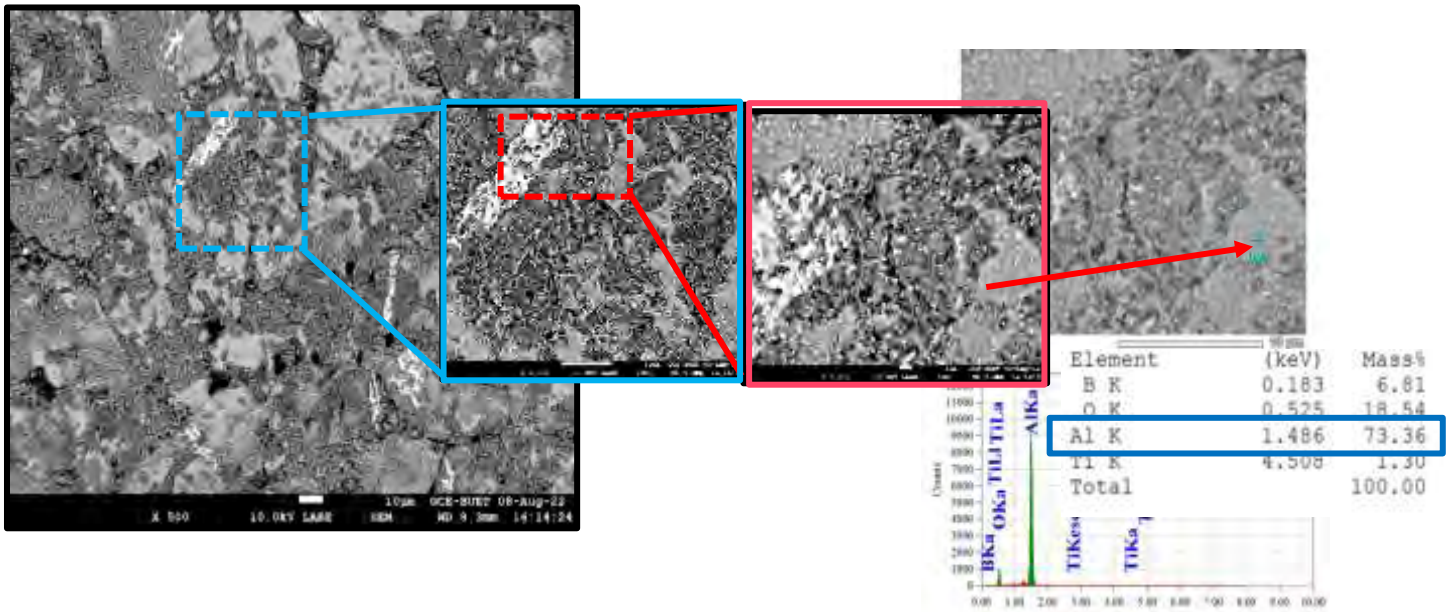

Figure 4.20 S3 (0,800) structure and composition

The microstructures of S6 samples at different magnifications (x 500, x 1000, x 2000, and x 5000) are shown in Figure 4.21. At x 5000, the dispersed Al_2O_3, TiB_2, and TiAl can be seen in the aluminum matrix. At x 500, t 25% external aluminum is visible.

The dashed line in Figure 4.21 (b) marks the reinforcement lean area (RLA) and reinforcement rich area (RRA). The RRA contains the reinforcements within the aluminium matrix, while the RLA primarily comprises the outer external aluminium matrix.

Figure 4.22 illustrates that the outer matrix of this composite consists of 98.53% aluminium, indicating that it is mainly an aluminium matrix. Additionally, the outer external matrix contains only a small percentage of reinforcements.

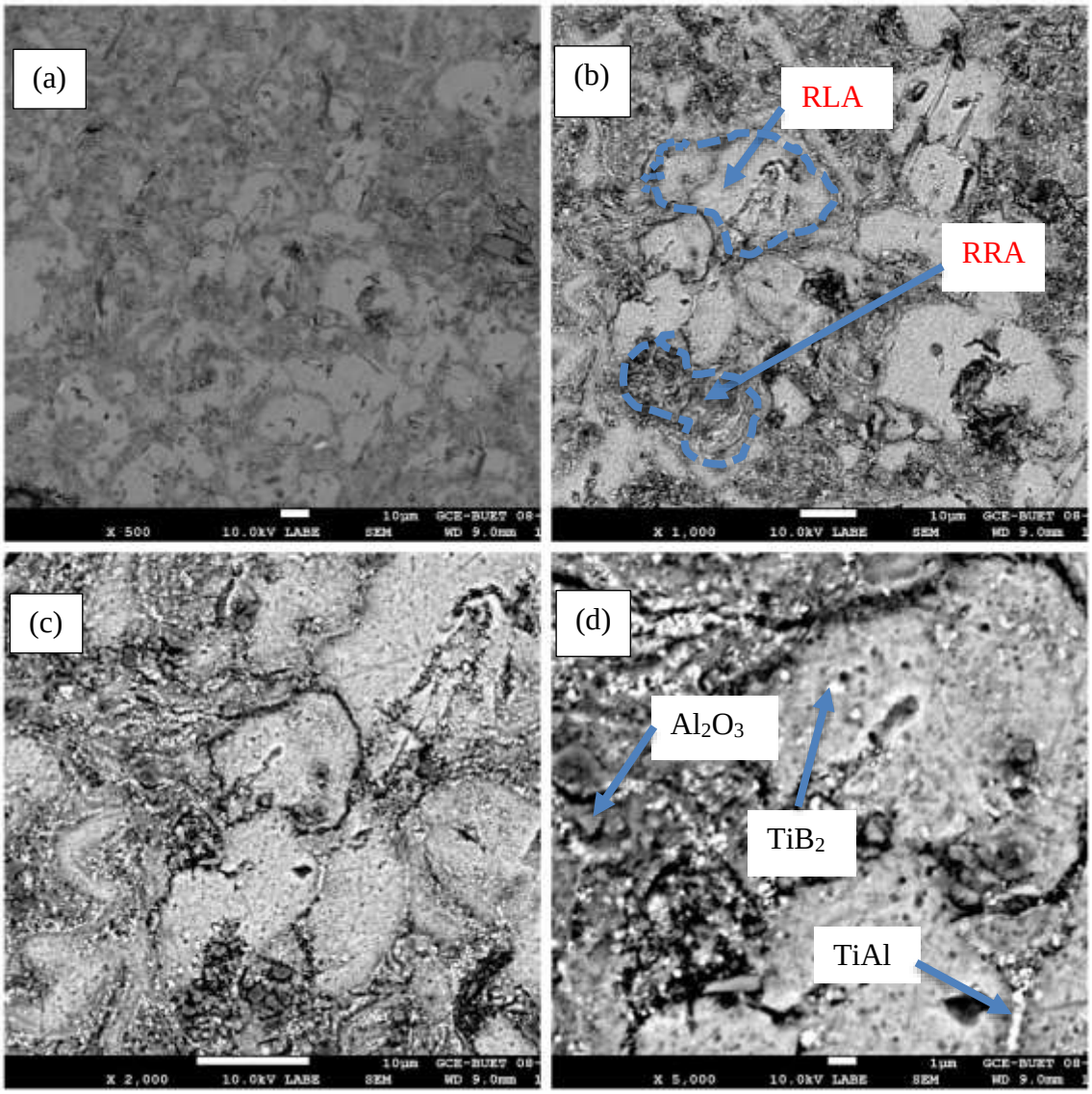

Figure 4.21 S6 SEM images (a) x 500 (b) x 1,000 (c) x 5,000 (d) x 10,000

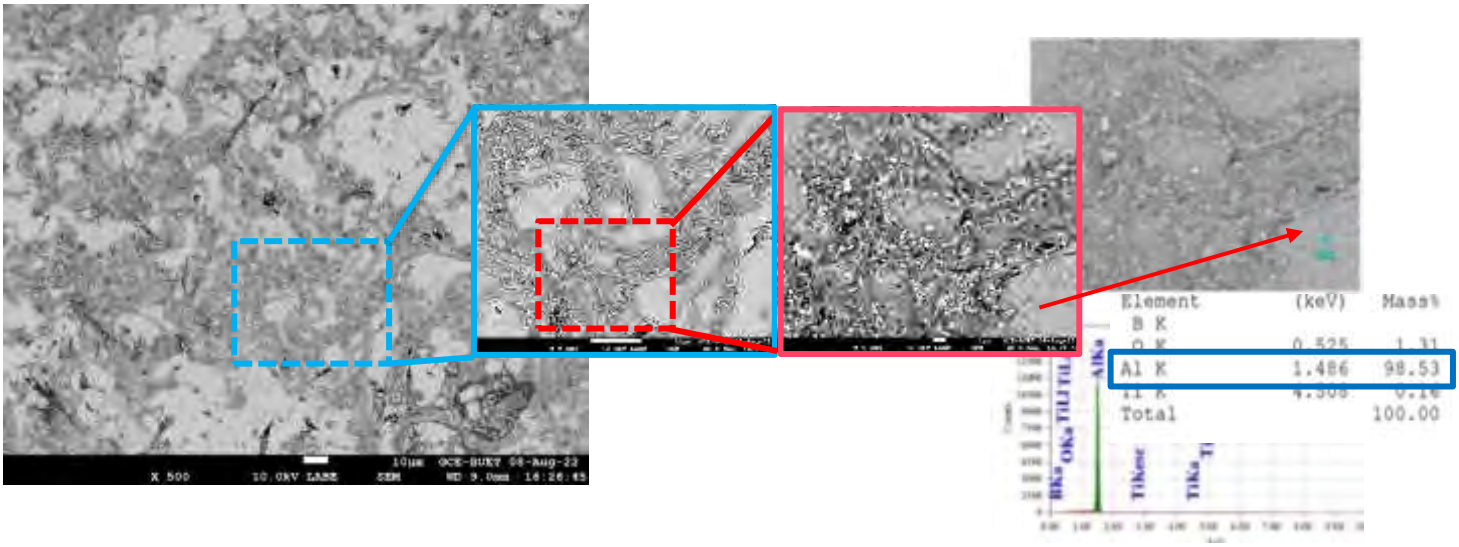

Figure 4.22 S6 (25,800) structure and composition.

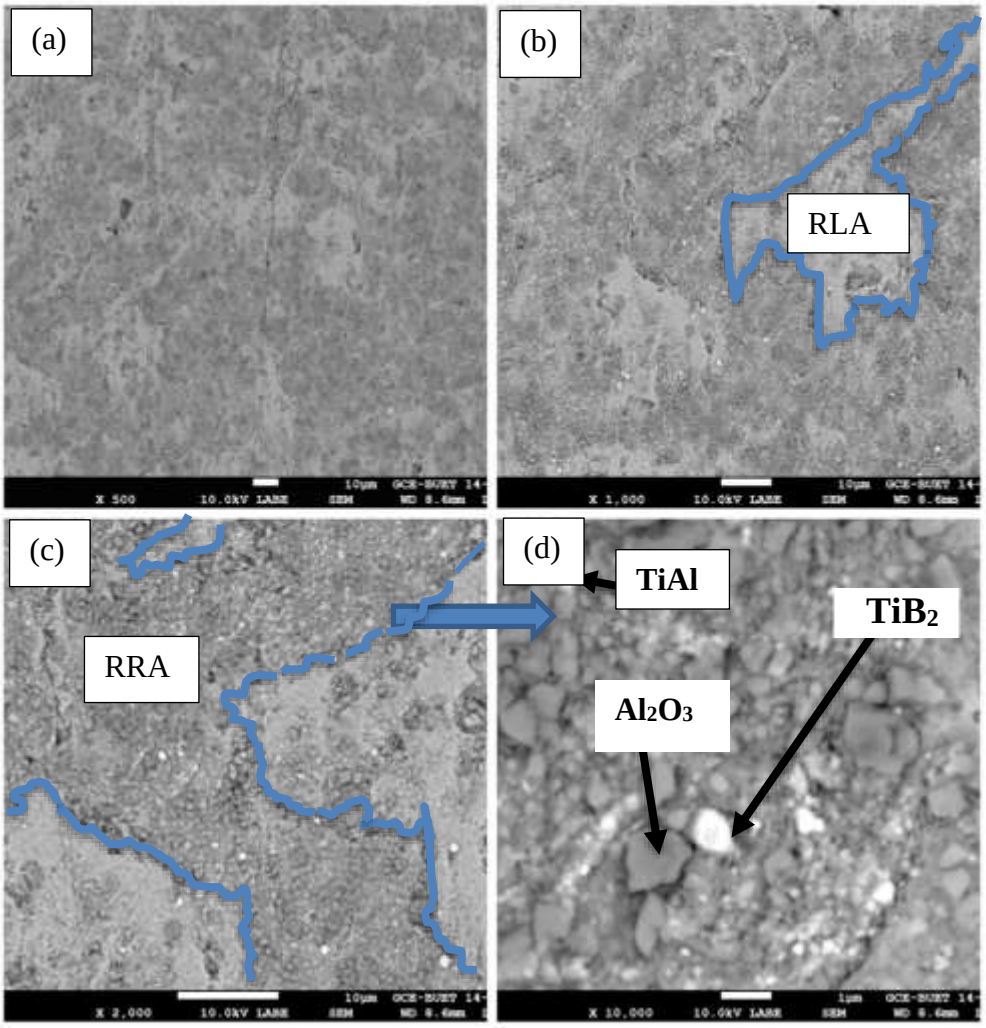

Figure 4.23 S9 SEM images (a) x 500 (b) x 1,000 (c) x 5,000 (d) x 10,000

Figure 4.23 displays the scanning electron microstructure of the S9 sample at four different magnifications (a) x 500, (b) x 1,000, (c) x 5,000, and (d) x 10,000. The external aluminium content in the sample is 50%, resulting in an increase in RLA compared to samples containing 0% and 25% external aluminium.

In Figure 4.24 , the reinforcement-rich area (RRA) of sample S9 is magnified at x5000. Figure 4.24 depicts the presence of Al_2O_3, TiAl, and TiB_2 phases in the aluminium matrix.

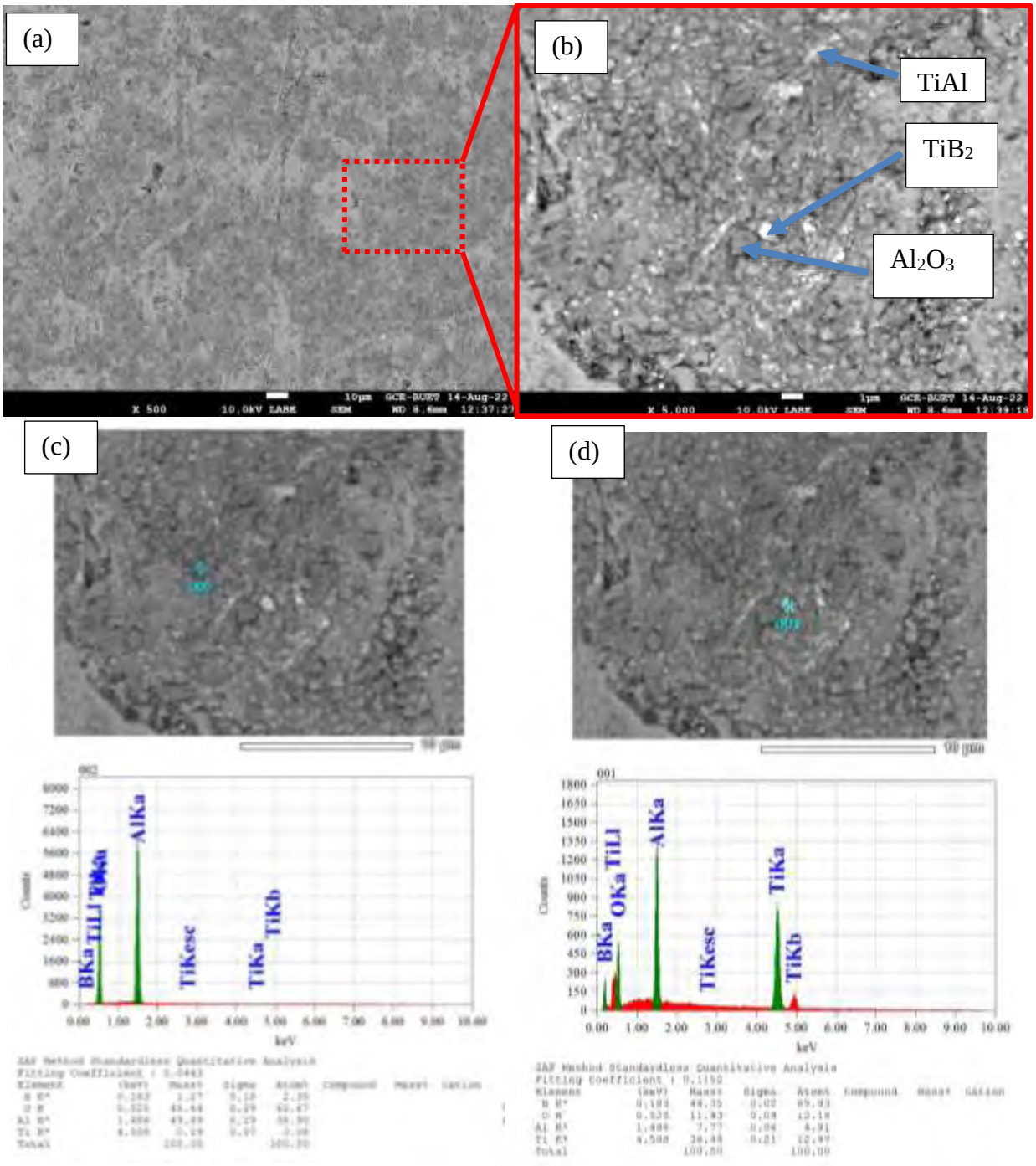

Figure 4.24 (a) x 500 magnified image of S9 (b) x 5, 000 magnified image of S9 (c) EDS analysis of S9 (d) EDS analysis of S9

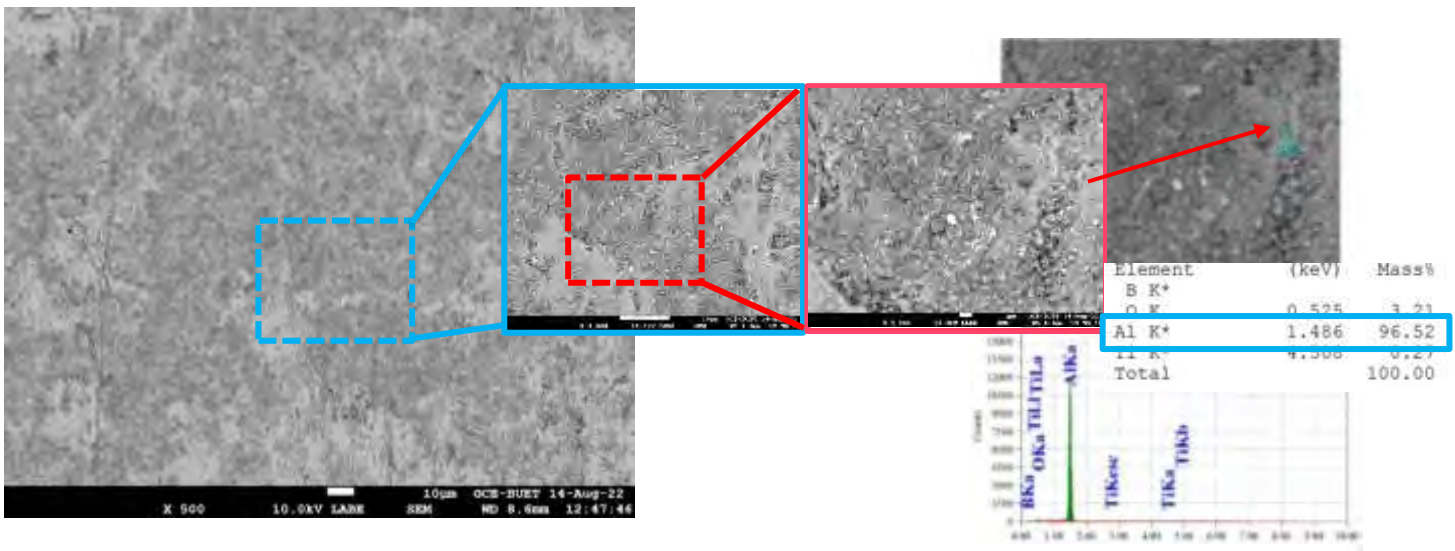

Figure 4.25 S9 (50,800) structure and composition

The reinforcement-rich area contains a higher concentration of dispersed reinforcements within the matrix, while the reinforcement-lean area comprises the outer aluminium matrix. The mass percentage of aluminium in this RLA region is 96.52%, as indicated in Figure 4.25.

The scanning electron microscopic images of S12 are presented in Figure 4.26 , which illustrates that the external aluminum matrix percentage is the highest. Here, it can be observed that the external aluminium percentage is highest so that the highest external matrix. This matrix is reinforcement leaned . However, the internal matrix is rich with reinforcements.

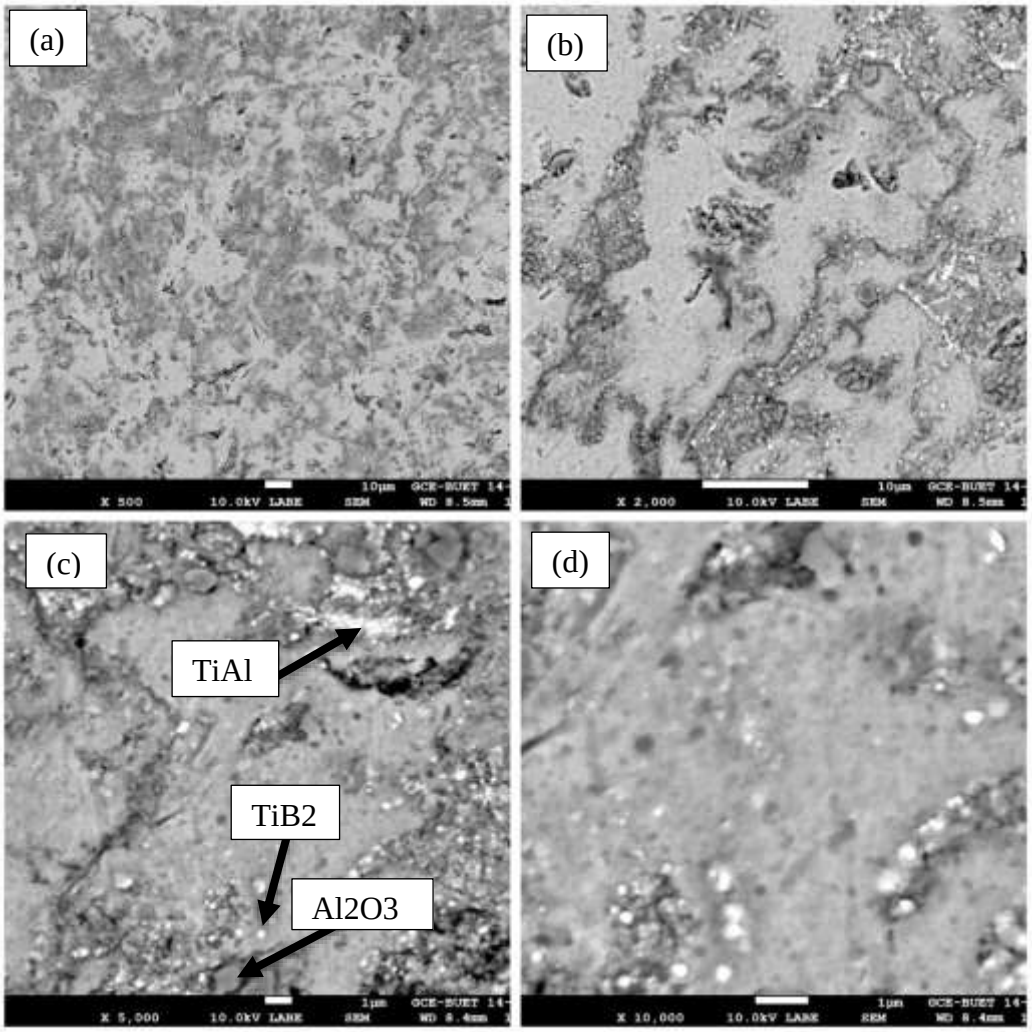

Figure 4.26 S9 SEM images (a) x 500 (b) x 2,000 (c) x 5,000 (d) x 10,000

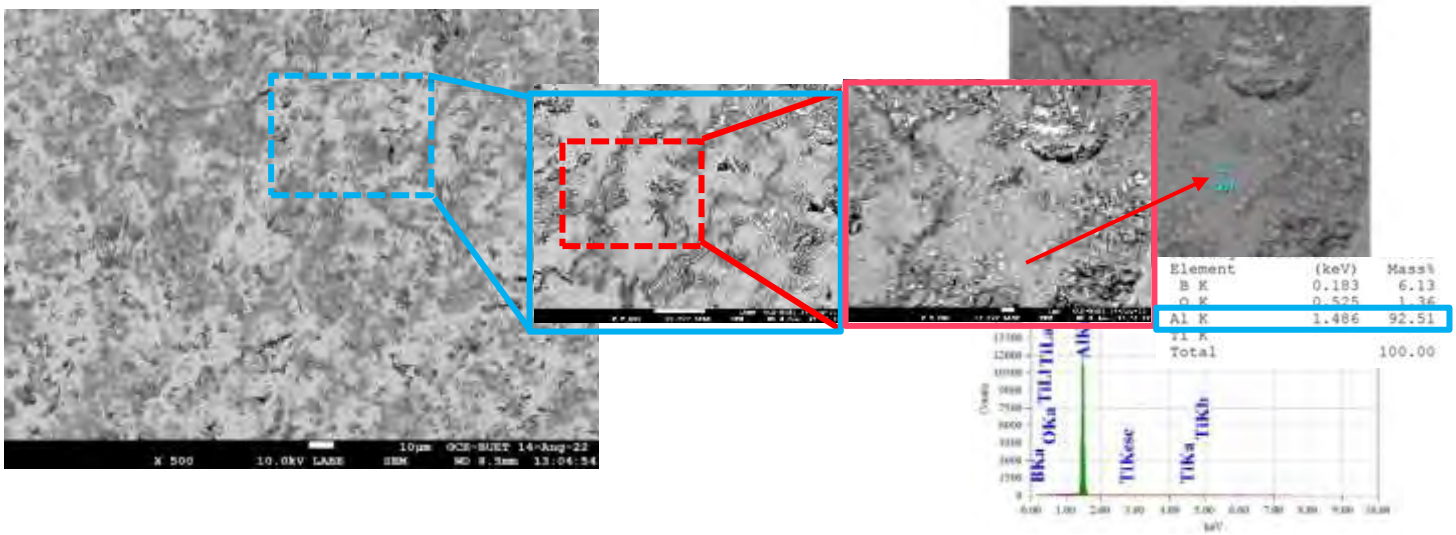

Figure 4.27 S12 (75,800) structure and composition

In Figure 4.27, the microstructures of S12 sample is shown . In the external matrix , aluminium percentage is about 92.51 %. Additionally, the outer external matrix contains only a small percentage of reinforcements.

With increasing the percentages of external aluminium, the outer ductile aluminium matrix is become more connected . In Figure 4.28, the continuous outer aluminium matrix is shown.

It is also observed that the outer aluminium matrix is not completely devoid of reinforcement. Some reinforcements can be seen, especially closer to the interface of composite region and outer aluminium matrix. This may be due to the fact that TiO_2 and H_3BO_3 present at the surface of the ball milled Al-TiO_2 -H_3BO_3 powder agglomerates has entered the aluminium outer matrix powder during the rotator mixing stage and reacted to form the reinforcements during sintering.

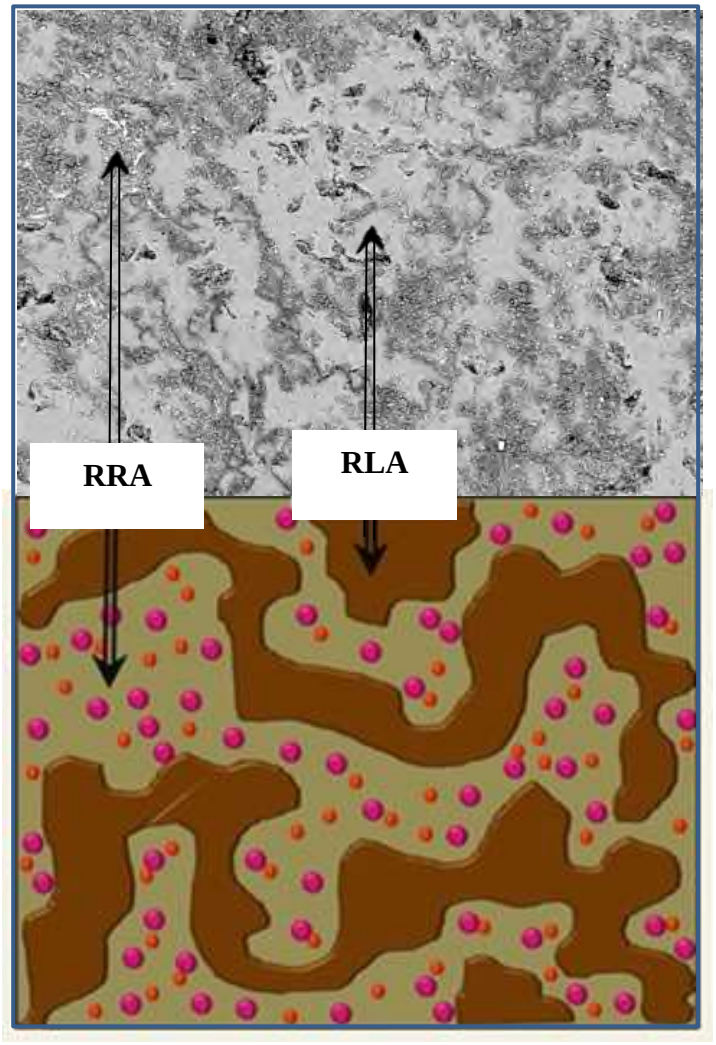

Figure 4.28 S12 Dual matrix composite

4.4 Mechanical Properties Analysis

To evaluate the mechanical properties of the AMMCs, two different testing were used: Vickers hardness testing and diametral compression testing. Both of these tests were utilized to obtain a comprehensive understanding of the mechanical characteristics of the AMMC samples.

4.4.1 Vickers Hardness Test

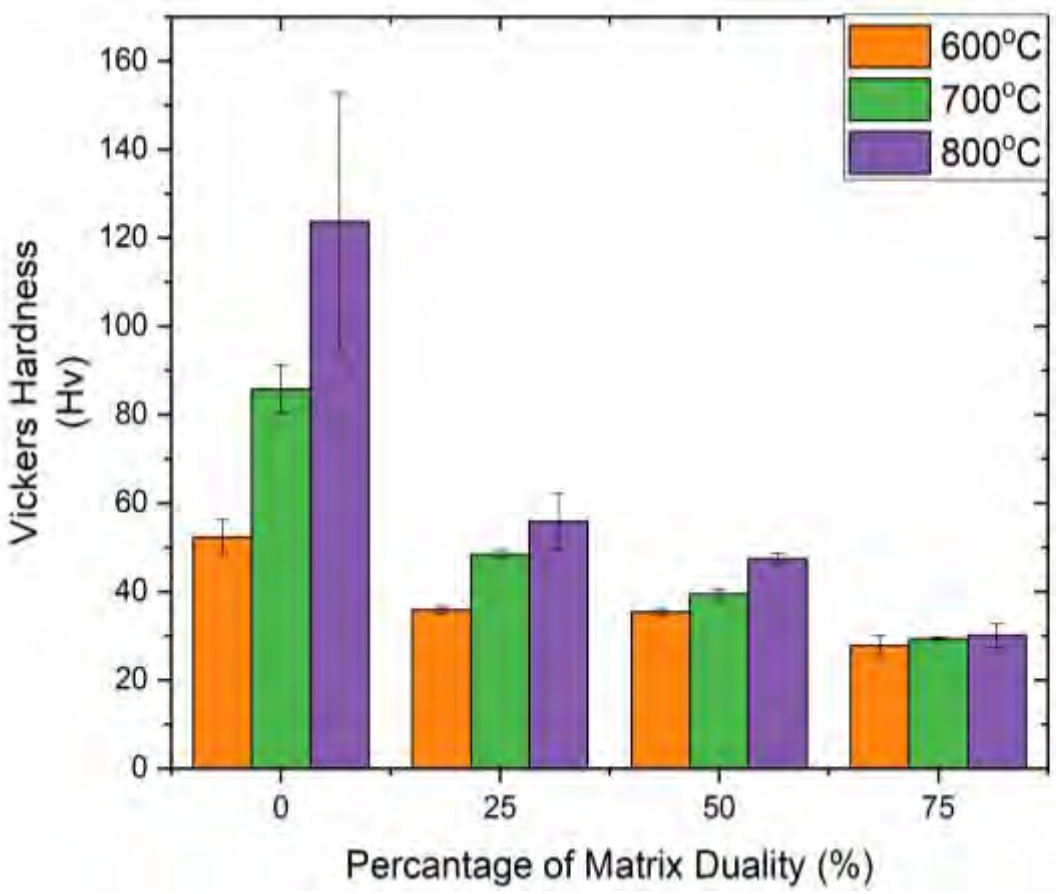

Figure 4.29 Hardness values with percentage of external aluminium and temperature.

Figure 4.29 displays the correlation between sample hardness and temperature, as well as the influence of external aluminum matrix on hardness. The graph illustrates that the samples sintered at 800℃ show the highest hardness, while the samples sintered at 600℃ demonstrate the lowest hardness. Furthermore, as the proportion of external aluminum in the matrix increases, the hardness of the samples decreases. The most substantial reduction in hardness occurs at a sintering temperature of 800℃. Conversely, at 600℃, the decline in hardness is more gradual as the external aluminum percentage increases.

For samples that lack any external aluminum (S1, S2, S3), the average Vickers hardness values for samples sintered at 600℃, 700℃, and 800℃ are approximately 53 HV, 86 HV, and 125 HV, respectively. The rise in hardness with increasing sintering temperature is remarkable.

However, for samples containing 25% external aluminum, the average hardness declines from 125 HV to about 60 HV when the sintering temperature is 800℃. Beyond this point, the decline in hardness becomes less pronounced. For samples containing 75% external aluminum and sintered at 800℃ , the hardness value is approximately 32 HV.

Overall, Figure 4.29 accurately represents the relationship between sample hardness, temperature, and the proportion of external aluminum in the matrix. Specifically, for samples sintered at 800℃, the addition of external aluminum substantially affects hardness, while for samples sintered at 600℃, the effect is less noticeable.

4.4.2 Tensile Strength Analysis

Figure 4.30 illustrates the tensile strength of the samples. Sample S3, sintered at 800℃ without any external aluminum, exhibits the highest tensile strength of approximately 94 MPa. However, the addition of 25% external aluminum reduces the tensile strength to around 55 MPa and increasing the proportion of external aluminum beyond 25% does not significantly affect the tensile strength. Moreover, the external aluminum has a minor impact on the tensile strength when samples are sintered at 600℃ and 700℃.

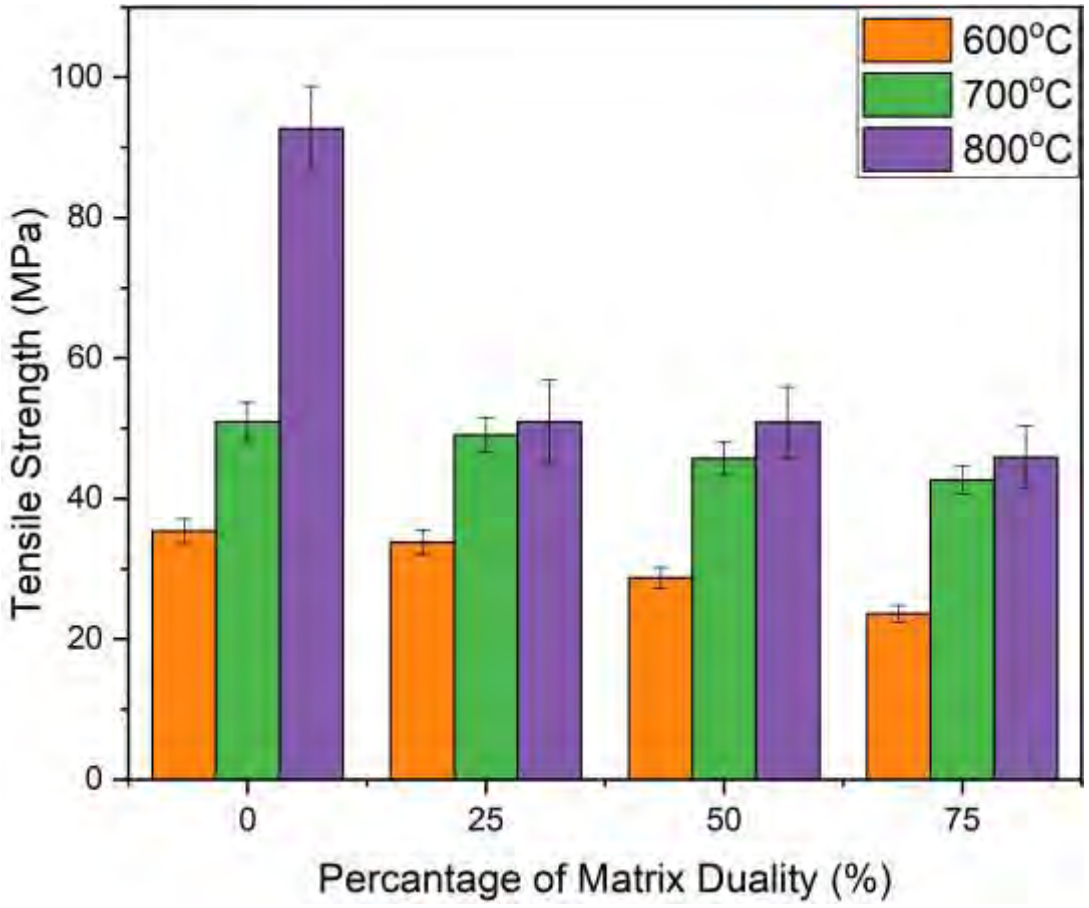

Figure 4.30 Temperature and external aluminium effect on tensile strength

4.4.3 Comparison Between the Tensile Strength and Hardness

Figure 4.31 displays the changes in hardness and tensile strength with increasing external aluminum percentage for samples sintered at 600℃. Both the tensile strength and hardness decrease with increasing external aluminum proportion, but the reduction is more pronounced for hardness than for tensile strength.

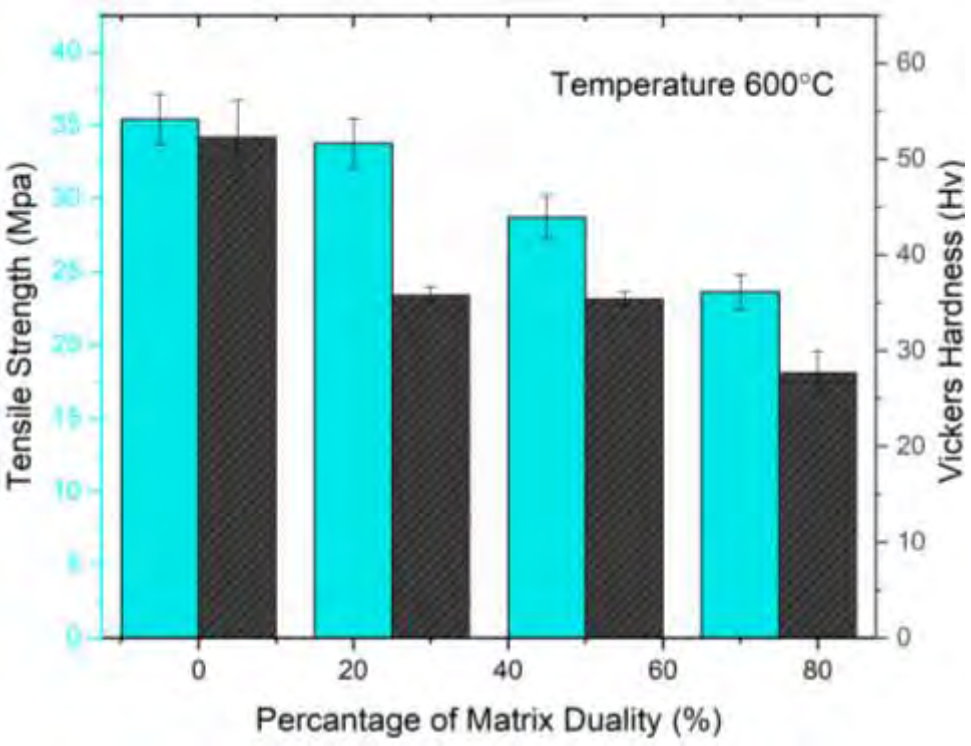

Figure 4.31 Tensile strength and hardness change with increasing external aluminium at 600℃

In Figure 4.32, the changes in tensile strength and hardness with external aluminum addition are shown for samples sintered at 700℃. The tensile strength decreases steadily, while the hardness decreases more rapidly.

Figure 4.33 depicts the highest changes in both tensile strength and hardness with external aluminum addition, observed for samples sintered at 800℃. At this temperature, more in situ reinforcements, including TiB_2, are formed, which play a significant role in increasing both the tensile strength and hardness.

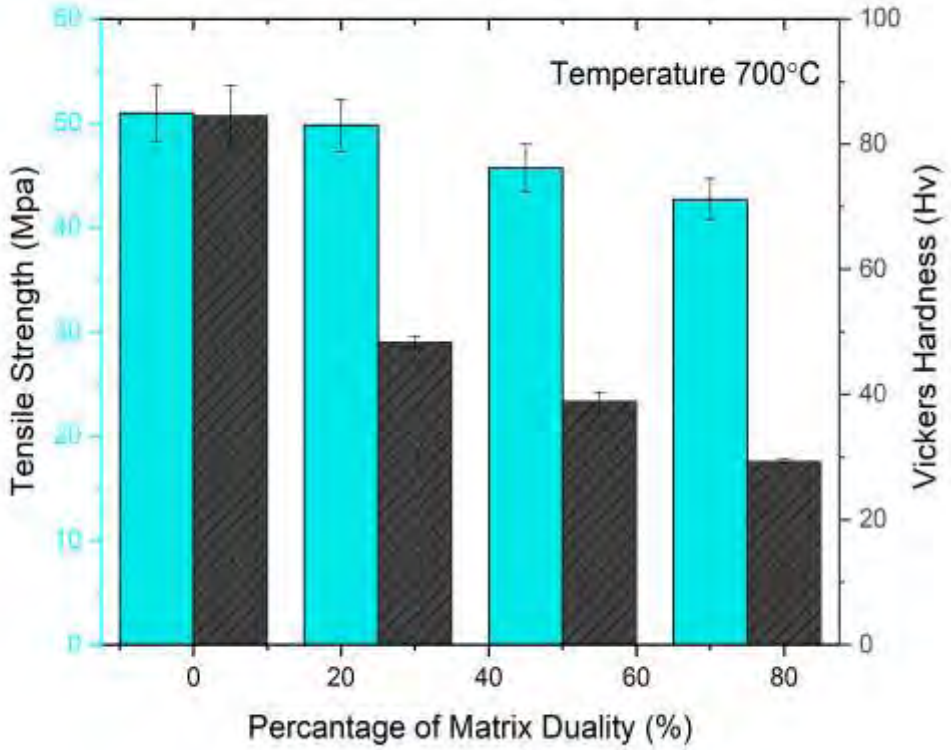

Figure 4.32 Tensile strength and hardness change with increasing external aluminium at 700℃

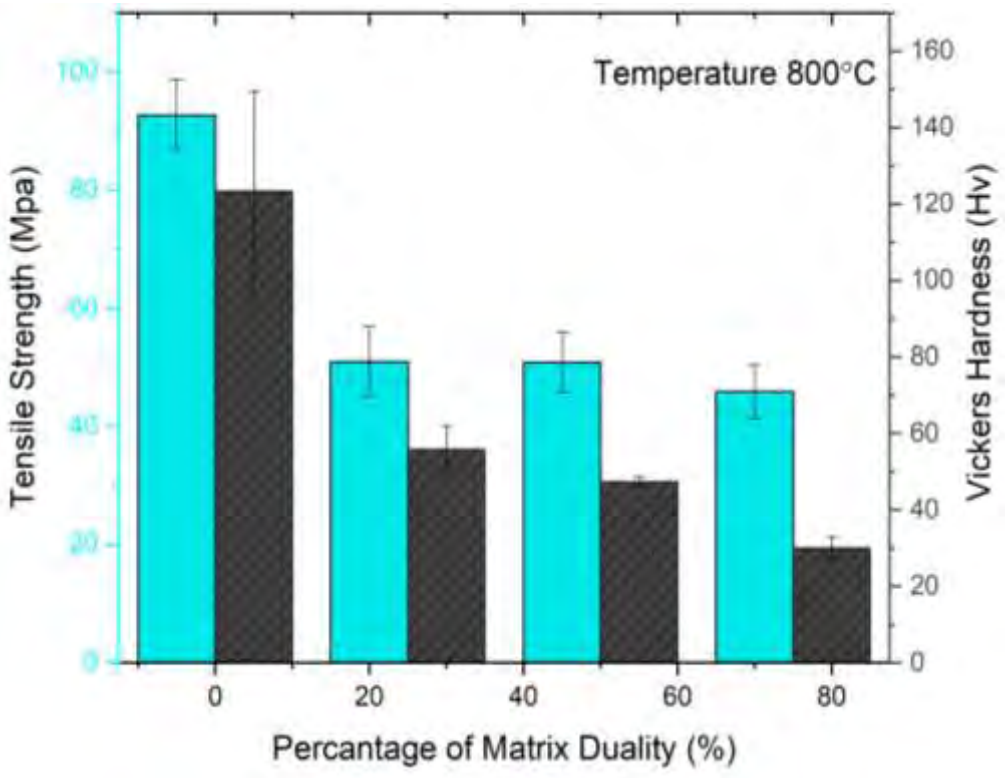

Figure 4.33 Tensile strength and hardness change with increasing external aluminium at 800℃

4.4.4 Toughness Analysis

4.4.4.1 Effect of Sintering Temperature

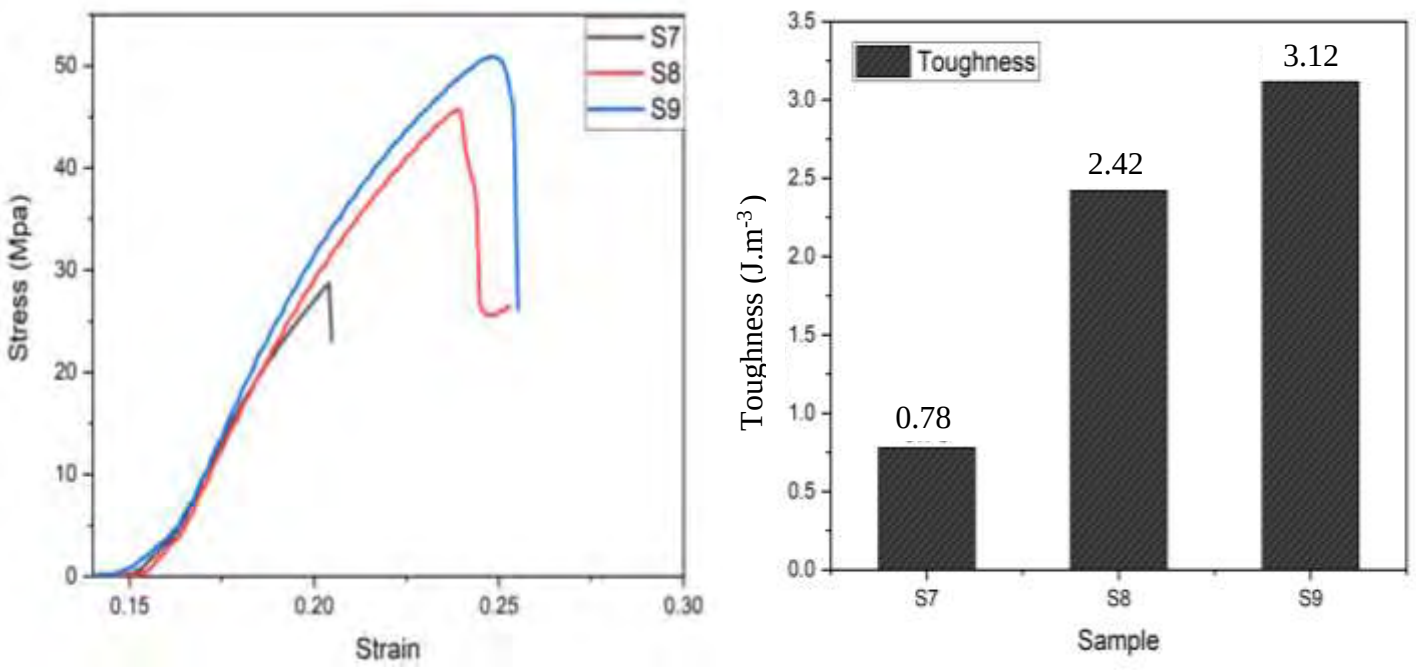

Figure 4.34 Toughness of sample S1, S2, S3

In Figure 4.34, stress-strain curves of three samples with 50% external aluminum are analyzed to understand the effect of sintering temperature on the samples with a fixed composition. The results show that the toughness of the samples increases with increasing temperature, and sintering temperature has a significant effect on the toughness. This is because at higher sintering temperatures, more in-situ reactions can occur, which were not possible at lower sintering temperatures. As a result, the formation of reinforcements was affected by temperature, which significantly changed the toughness of the samples.

The tensile strength was mainly affected by sintering temperature, as seen in Figure 4.30. The change in toughness for the three samples was primarily due to the change in tensile strength.

4.4.4.2 Effect of External Aluminium Percentage

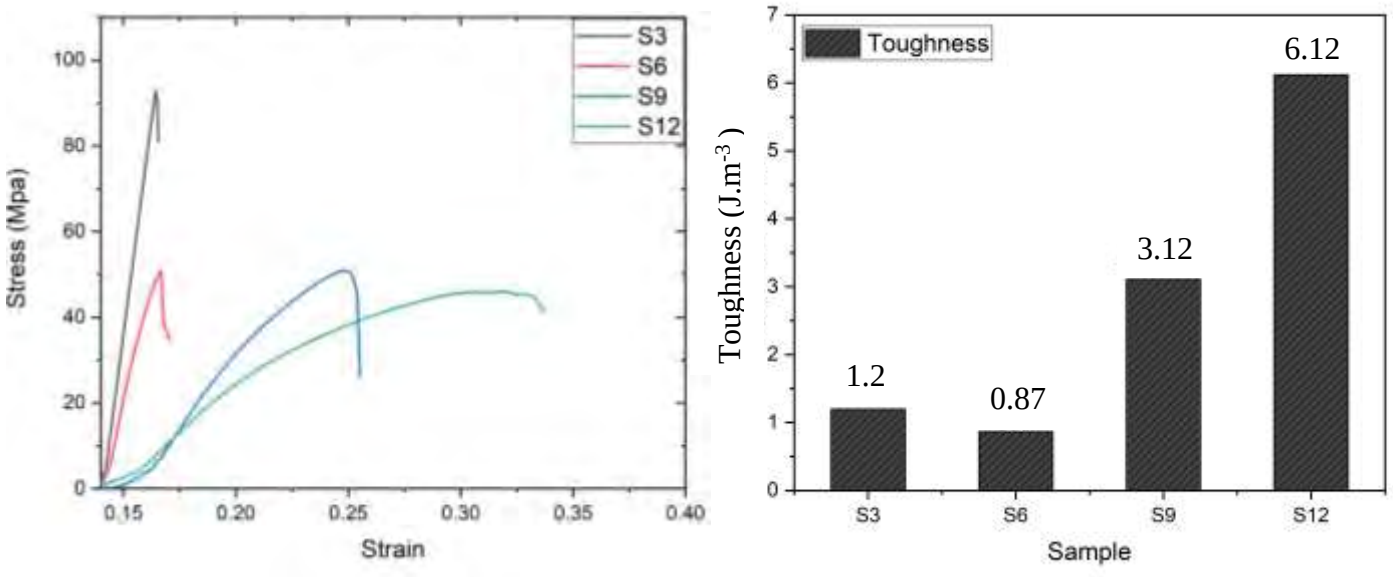

Figure 4.35 Toughness of samples S3, S6, S9 and S12 sintered at 800℃

In Figure 4.34, the sample sintered at 800 ℃ showed the highest toughness. In Figure 4.35, the toughness of all four samples sintered at 800 ℃ was analyzed, where each sample had a different external aluminum percentage: sample S3 has 0%, sample S6 has 25%, sample S9 has 50%, and sample S12 has 75%. Sample S3 exhibited very high strength but low strain compared to the other three samples. The ultimate tensile strength values for the other three samples were not significantly different, but the area under the curve values varied greatly. The toughness values were analyzed based on the area under the curve values, and the highest toughness was observed for sample S12, which was approximately 6.12 $J.m^{-3}$.

The outer aluminium matrix plays a great role in increasing the toughness value shown in Figure 4.36 . The external ductile matrix can improve the toughness of a material in two ways, known as Type I and Type II toughening mechanisms.

Type I toughening mechanism involves the crack propagating through the composite region and coming in contact with the outer aluminum matrix. The matrix deforms and absorbs energy, delaying crack propagation and shielding the crack tip.

Type II toughening mechanism involves the crack being generated in the particle-rich composite region, which is more susceptible to cracking. The crack is then deflected by the matrix near the composite region and propagates along the interface between the composite region and the outer aluminum.

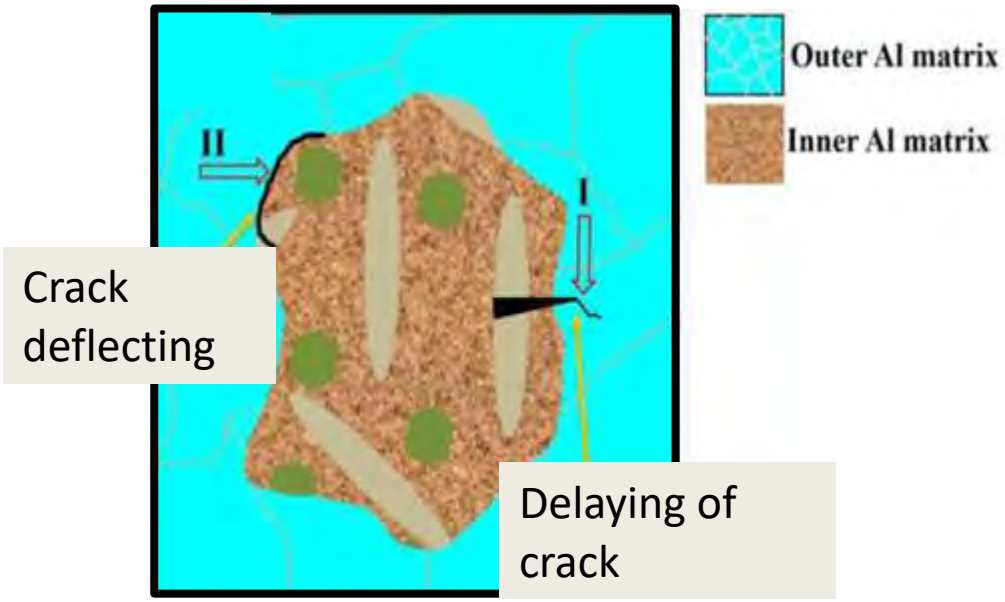

Figure 4.36 schematic of crack propagation in DMC [7]

4.5 Analyzing How the Research Aligns or Differs from Other Works

Pure aluminium showed micro hardness value of 25.9HV [67]. Table 4.3 indicates how the hardness of the AMMC changes with increasing the percentages of Al_2O_3 and TiO_2. The hybrid composite (Al-Al_2O_3-TiO_2) was prepared by mechanical stir casting with equal proportion of reinforcement (2.5, 5.0, 7.5 and 10 wt.%).

Table 4.3 Vickers hardness of AlAlT (Al-6351-Al_2O_3-TiO_2) hybrid single metal matrix composite samples [68]

Sample No.	**Al-6351 (Wt. %)**	**Al_2O_3 (Wt. %)**	**TiO_2 (Wt. %)**	**Vickers Hardness**
1	95	2.5	2.5	49
2	90	5	5	55
3	85	7.5	7.5	68
4	80	10	10	79

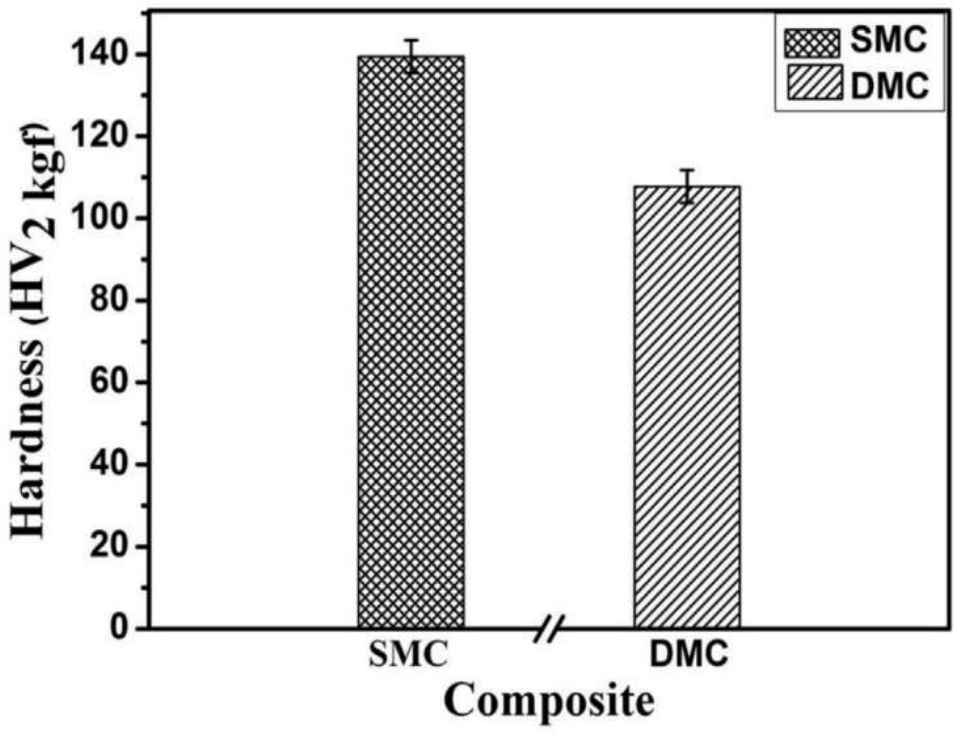

Figure 4.37 Variation of bulk hardness of SMC and DMC [7]

In Figure 4.37 Single matrix composite (SMC) composition is $Al + Al_3Ti + Al_2O_3$ and dual matrix composite (DMC) composition is ($Al + Al_3Ti + Al_2O_3$) + 50% external aluminium .

Figure 4.38 indicates the hardness of dual and single-matrix CNT–Al composites and milled aluminum processed via Spark Plasma Extrusion (SPE) . Here the composition of single matrix composite is aluminium + 5% CNT. The composition of dual matrix composite is (aluminium + 5% CNT)+ 50% external aluminium of total sample.

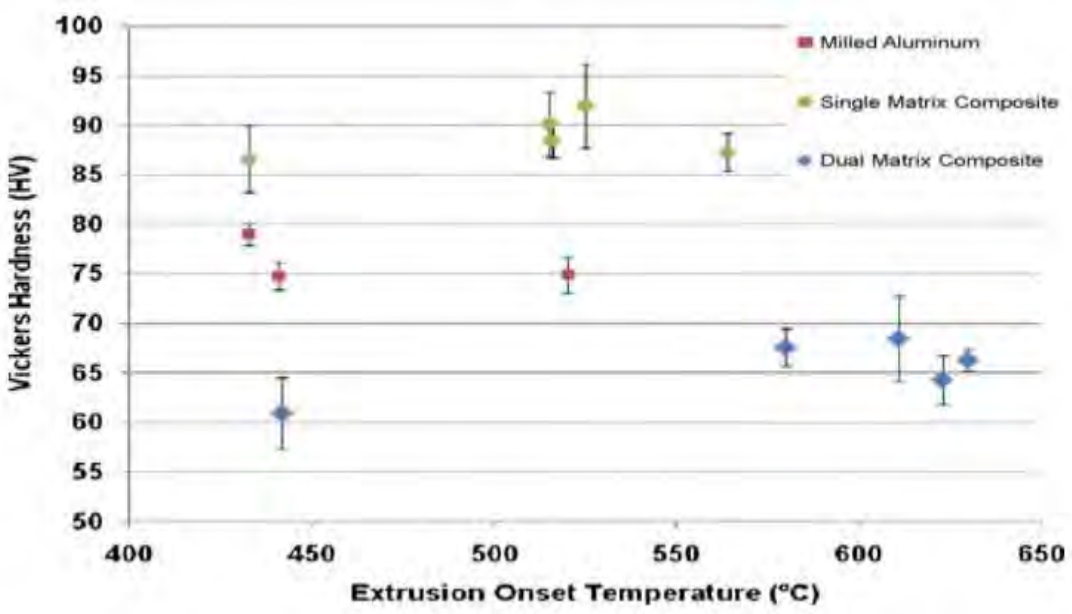

Figure 4.38 Effect of extrusion onset temperature on Vickers hardness of the investigated materials (all hardness values represented in the figure are for micro-hardness except for the dual matrix composites which are macro-hardness data, each data point in the figure represents the average of at least 3 readings except for the dual matrix data point for the extrusion onset temperature of 442 ◦C which is the average of two readings) [33].

In Figure 4.29, Vickers hardness analysis bar chart represents that a single matrix exhibits a hardness range of 90-150 HV when sintered at 800℃. Additionally, a dual matrix composite shows a hardness range of 30-70 HV. It is noteworthy that the hardness values vary with the percentage of external aluminum present and sintering temperature of the samples.

Chapter 5: Summary and Conclusion

This study focused on the production and analysis of dual matrix hybrid composites of aluminum using a simple Al-H_3BO_3-TiO_2 system through ball milling, cold pressing, and sintering. The composites' thermal, structural, morphological, and mechanical properties were analyzed and then compared to those of single matrix composites (0% external aluminium) .

The findings from this study are summarized as follows :

a) According to TG, DTA, and DTG data, in situ reinforcements started forming after 550°C, and a DTG curve showed an exothermic peak at 750°C for TiB_2 production.

b) The XRD results showed that the hybrid composites were indeed formed. At 600°C sintered samples , the main reinforcements in the aluminum matrix were B_2O_3, Al_2O_3, and TiAl. At 700°C sintered samples, the main reinforcements in the aluminum matrix were Al_2O_3, TiAl, and AlB_2. Finally, at 800°C sintered samples, the main reinforcements in the aluminum matrix were Al_2O_3, TiAl, and TiB_2.

c) The morphology of the samples was revealed by SEM and Optical microstructures. As the sintering temperature increased, there was an increase in in-situ reinforcements. Furthermore, as the external aluminium percentage increased, the outer ductile matrix became more connected.

d) The EDS results revealed that the inner matrix of the composites contained higher amounts of reinforcements compared to the outer matrix. However, the outer matrix was not entirely without reinforcements, but had lower concentrations of them.

e) The microhardness of the samples was found to be dependent on both the sintering temperature and the external aluminum percentage. The highest microhardness value was observed for the samples sintered at 800℃ without the addition of external aluminum, which was approximately 1 3 VH, with an average value of 125 VH. However, when external aluminum was added, the microhardness value sharply decreased to 60 VH.

f) The tensile strength of the composites also showed a similar trend as the microhardness, with the highest value observed for the 800℃ sintered samples with no external aluminum added. However, the change in tensile strength with the addition of external aluminum was more gradual compared to the sharp decrease in microhardness.

g) The dual matrix composites had lower hardness and tensile strength compared to the single matrix composites. However, the toughness of the 50% and 75% external aluminium dual matrix composites was higher than that of the single matrix. This indicates that while the dual matrix composites may not be as strong as the single matrix, they are more resistant to crack propagation and deformation, which makes them more durable under certain conditions.

h) Interconnected outer matrix was observed for the composites with 75% external aluminum. As a result, these composites exhibited the highest toughness among all the samples studied.

Chapter 6: Recommendation to Future Work

As the field of aluminum alloys and composites as a construction material is rapidly advancing, future research should aim to bridge the gap between theoretical knowledge and practical applications. This would involve conducting studies that can effectively address the challenges encountered in real-life structures.

1. One critical area of research that requires attention is the evaluation of properties , such as tensile strength. To achieve this, future research should focus on systematic evaluations of in situ hybrid aluminum composites. Such evaluations should compare the mechanical properties of the composites with published results and industrial specifications to avoid repetitive and self-evident reports. The findings from these studies would provide a foundation for the practical application of hybrid in situ aluminum alloys.

2. Another interesting area of future research is the examination of the ductility and energy dissipation capabilities of structural members under cyclic loading. This will help to enhance the understanding of the behavior of aluminum composites under real-life conditions.

3. Mathematical modeling techniques could be used to improve the prediction of mechanical and wear properties of aluminum alloys. This approach would enable researchers to better understand the underlying mechanisms that govern the behavior of these materials and develop more accurate models to predict their properties.

4. In addition, surface morphology analysis using techniques such as AFS, XPS, and EBSD is also an important aspect of future research. Such studies would help to enhance the understanding of the microstructure of aluminum composites and their relationship with their mechanical properties.

5. Finally, the study of fracture toughness is also a crucial area that requires attention in future research. Understanding the fracture behavior of aluminum composites is critical for predicting their failure under different loading conditions, and this knowledge can be used to enhance the design of aluminum-based structures.

References

[1] T. R, R. V, P. K. K, T. R, and A. R, "A novel approach for the production and characterisation of aluminium–alumina hybrid metal matrix composites," *Mater. Res. Express*, vol. 7, no. 4, p. 046512, Apr. 2020, doi: 10.1088/2053-1591/ab8657.

[2] A. Azarniya and H. R. Madaah Hosseini, "A new method for fabrication of in situ Al/Al 3 Ti–Al 2 O 3 nanocomposites based on thermal decomposition of nanostructured tialite," *J. Alloys Compd.*, vol. 643, pp. 64–73, Sep. 2015, doi: 10.1016/j.jallcom.2015.04.145.

[3] P. Samal, P. R. Vundavilli, A. Meher, and M. M. Mahapatra, "Recent progress in aluminum metal matrix composites: A review on processing, mechanical and wear properties," *J. Manuf. Process.*, vol. 59, pp. 131–152, Nov. 2020, doi: 10.1016/j.jmapro.2020.09.010.

[4] R. Gecu and A. Karaaslan, "A Comparative Study on Titanium-Reinforced Aluminium Matrix Composites Produced by Melt Infiltration Casting and Squeeze Infiltration," *Int. J. Met.*, vol. 13, no. 2, pp. 311–319, Apr. 2019, doi: 10.1007/s40962-018-0253-0.

[5] E. Fereiduni, M. Yakout, and M. Elbestawi, "Laser-Based Additive Manufacturing of Lightweight Metal Matrix Composites," in *Additive Manufacturing of Emerging Materials*, B. AlMangour, Ed. Cham: Springer International Publishing, 2019, pp. 55–109. doi: 10.1007/978-3-319-91713-9_3.

[6] X. Qu *et al.*, "In situ synthesis of a gamma-Al_2O_3 whisker reinforced aluminium matrix composite by cold pressing and sintering," *Mater. Sci. Eng. A*, vol. 709, pp. 223–231, Jan. 2018, doi: 10.1016/j.msea.2017.10.063.

[7] S. Lakra, T. K. Bandyopadhyay, S. Das, and K. Das, "Synthesis and characterization of in-situ (Al–Al3Ti–Al2O3)/Al dual matrix composite," *J. Alloys Compd.*, vol. 842, p. 155745, Nov. 2020, doi: 10.1016/j.jallcom.2020.155745.

[8] A. Azarniya, A. Azarniya, A. Abdollah-zadeh, and S. Ramakrishna, "In Situ Hybrid Aluminum Matrix Composites: A Review of Phase Transformations and Mechanical Aspects," *Adv. Eng. Mater.*, vol. 21, no. 7, p. 1801269, 2019, doi: 10.1002/adem.201801269.

[9] Z. L. Chao *et al.*, "Design, microstructure and high temperature properties of in-situ Al3Ti and nano-Al2O3 reinforced 2024Al matrix composites from Al-TiO2 system," *J. Alloys Compd.*, vol. 775, pp. 290–297, Feb. 2019, doi: 10.1016/j.jallcom.2018.09.376.

[10] T. Albert, J. Sunil, A. Simon Christopher, R. Jegan, P. Anand Prabhu, and M. Selvaganesan, "Preparation and characterization of aluminium-titanium carbide (Al-TiC) composite using powder metallurgy," *Mater. Today Proc.*, vol. 37, pp. 1558–1561, 2021, doi: 10.1016/j.matpr.2020.07.155.

[11] Q. Zhang, G. Wu, and L. Jiang, "Tensile deformation behavior of a sub-micrometer Al2O3/6061Al composite," *Mater. Sci. Eng. A*, vol. 483–484, pp. 281–284, Jun. 2008, doi: 10.1016/j.msea.2006.09.143.

[12] A. Fadavi Boostani *et al.*, "Enhanced tensile properties of aluminium matrix composites reinforced with graphene encapsulated SiC nanoparticles," *Compos. Part Appl. Sci. Manuf.*, vol. 68, pp. 155–163, Jan. 2015, doi: 10.1016/j.compositesa.2014.10.010.

[13] P. Dev Srivyas and M. S. Charoo, "Application of Hybrid Aluminum Matrix Composite in Automotive Industry," *Mater. Today Proc.*, vol. 18, pp. 3189–3200, Jan. 2019, doi: 10.1016/j.matpr.2019.07.195.

[14] K. Chawla, "Metal-matrix composites in ground transportation," *JOM*, vol. 58, pp. 67–70, Nov. 2006, doi: 10.1007/s11837-006-0231-5.

[15] V. Abbasi Chianeh, H. R. Madaah Hosseini, and M. Nofar, “Micro structural features and mechanical properties of Al–Al3Ti composite fabricated by in-situ powder metallurgy route,” *J. Alloys Compd.*, vol. 473, no. 1, pp. 127–132, Apr. 2009, doi: 10.1016/j.jallcom.2008.05.068.

[16] M. A. Muñoz-Morris, J. I. Rexach, and M. Lieblich, “Comparative study of Al-TiAl composites with different intermetallic volume fractions and particle sizes,” *Intermetallics*, vol. 13, no. 2, pp. 141–149, Feb. 2005, doi: 10.1016/j.intermet.2004.07.033.

[17] A. Albiter, A. Contreras, E. Bedolla, and R. Perez, “Structural and chemical characterization of precipitates in Al-2024/TiC composites,” *Compos. Part Appl. Sci. Manuf.*, vol. 34, no. 1, pp. 17–24, Jan. 2003, doi: 10.1016/S1359-835X(02)00259-2.

[18] “Reinforcement coatings and interfaces in aluminium metal matrix composites | SpringerLink.” https://link.springer.com/article/10.1023/A:1004674822751 (accessed Jan. 02, 2023).

[19] J. Sheng, L. Wang, Y. Zhao, S. C. Xu, X. L. Liu, and W. D. Fei, “Effect of solution treatment on the texture and tensile properties of Mg2B2O5W/2024Al composite,” *J. Alloys Compd.*, vol. 701, Jan. 2017, doi: 10.1016/j.jallcom.2017.01.080.

[20] L. Xin *et al.*, “Effect of extrusion treatment on the microstructure and mechanical behavior of SiC nanowires reinforced Al matrix composites,” *Mater. Sci. Eng. A*, vol. 682, pp. 38–44, Jan. 2017, doi: 10.1016/j.msea.2016.11.042.

[21] S. C. Tjong, S. Q. Wu, and H. G. Zhu, “Wear behavior of in situ TiB2·Al2O3/Al and TiB2·Al2O3/Al–Cu composites,” *Compos. Sci. Technol.*, vol. 59, no. 9, pp. 1341–1347, Jul. 1999, doi: 10.1016/S0266-3538(98)00172-9.

[22] B. X. Liu *et al.*, “Gradient grain distribution and enhanced properties of novel laminated Ti–TiBw/Ti composites by reaction hot-pressing,” *Mater. Sci. Eng. A*, vol. 595, pp. 257–265, Feb. 2014, doi: 10.1016/j.msea.2013.12.013.

[23] B. X. Liu *et al.*, “Microstructure and tensile behavior of novel laminated Ti–TiBw/Ti composites by reaction hot pressing,” *Mater. Sci. Eng. A*, vol. 583, pp. 182–187, Oct. 2013, doi: 10.1016/j.msea.2013.06.058.

[24] S. Chen, D. Zhang, J. Li, and G. Sun, “In-situ formation of MgO whiskers on the surface of magnesium alloy powders,” *Powder Technol.*, vol. 253, pp. 677–680, Feb. 2014, doi: 10.1016/j.powtec.2013.12.038.

[25] Y. Zhou *et al.*, “Microstructure and properties of in situ generated MgAl2O4 spinel whisker reinforced aluminum matrix composites,” *Mater. Des.*, vol. 46, pp. 724–730, Apr. 2013, doi: 10.1016/j.matdes.2012.11.022.

[26] Y. Zhou, N. Zhao, C. Shi, E. Liu, X. Du, and C. He, “In-situ processing and aging behaviors of MgAl2O4 spinel whisker reinforced 6061Al composite,” *Mater. Sci. Eng. A*, vol. 598, pp. 114–121, Mar. 2014, doi: 10.1016/j.msea.2013.12.086.

[27] S. Tjong and G. Wang, “High-cycle fatigue properties of Al-based composites reinforced with in situ TiB2 and Al2O3 particulates,” *Mater. Sci. Eng. A*, vol. 386, no. 1–2, pp. 48–53, Nov. 2004, doi: 10.1016/S0921-5093(04)00931-1.

[28] M. Nakamura and K. Kimura, “Elastic constants of TiAl3 and ZrAl3 single crystals,” *J. Mater. Sci.*, vol. 26, no. 8, pp. 2208–2214, Apr. 1991, doi: 10.1007/BF00549190.

[29] I. C. Barlow, H. Jones, and W. M. Rainforth, “Evolution of microstructure and hardening, and the role of Al3Ti coarsening, during extended thermal treatment in mechanically alloyed Al-Ti-O based materials,” *Acta Mater.*, vol. 49, no. 7, pp. 1209–1224, Apr. 2001, doi: 10.1016/S1359-6454(01)00016-7.

[30] D. J. Lloyd, “The solidification microstructure of particulate reinforced aluminium/SiC composites,” *Compos. Sci. Technol.*, vol. 35, no. 2, pp. 159–179, Jan. 1989, doi: 10.1016/0266-3538(89)90093-6.

[31] B. Kaveendran, G. S. Wang, L. J. Huang, L. Geng, and H. X. Peng, “In situ (Al3Zr+Al2O3np)/2024Al metal matrix composite with novel reinforcement distributions fabricated by reaction hot pressing,” *J. Alloys Compd.*, vol. 581, pp. 16–22, Dec. 2013, doi: 10.1016/j.jallcom.2013.06.143.

[32] H.-X. Peng and J. R. G. Evans, “Bi-Continuous Metal Matrix Composites,” *Mater. Sci. Eng. A*, vol. 303, pp. 37–45, May 2001, doi: 10.1016/S0921-5093(00)01879-7.

[33] K. Morsi, A. M. K. Esawi, P. Borah, S. Lanka, A. Sayed, and M. Taher, “Properties of single and dual matrix aluminum–carbon nanotube composites processed via spark plasma extrusion (SPE),” *Mater. Sci. Eng. A*, vol. 527, no. 21, pp. 5686–5690, Aug. 2010, doi: 10.1016/j.msea.2010.05.081.

[34] V. Patel, A. El-Desouky, J. Garay, and K. Morsi, “Pressure-less and current-activated pressure-assisted sintering of titanium dual matrix composites: Effect of reinforcement particle size,” *Mater. Sci. Eng. -Struct. Mater. Prop. Microstruct. Process. - MATER SCI ENG -STRUCT MATER*, vol. 507, pp. 161–166, May 2009, doi: 10.1016/j.msea.2008.11.046.

[35] K. Morsi, V. Patel, S. Naraghi, and J. Garay, “Processing of titanium–titanium boride dual matrix composites,” *J. Mater. Process. Technol. - J MATER PROCESS TECHNOL*, vol. 196, pp. 236–242, Jan. 2008, doi: 10.1016/j.jmatprotec.2007.05.047.

[36] V. Chak, H. Chattopadhyay, and T. L. Dora, “A review on fabrication methods, reinforcements and mechanical properties of aluminum matrix composites,” *J. Manuf. Process.*, vol. 56, pp. 1059–1074, Aug. 2020, doi: 10.1016/j.jmapro.2020.05.042.

[37] A. Canakci, F. Arslan, and T. Varol, “Effect of volume fraction and size of B_4C particles on production and microstructure properties of B_4C reinforced aluminium alloy composites,” *Mater. Sci. Technol.*, vol. 29, no. 8, pp. 954–960, Aug. 2013, doi: 10.1179/1743284713Y.0000000232.

[38] V. V. Vani and S. K. Chak, “The effect of process parameters in Aluminum Metal Matrix Composites with Powder Metallurgy,” *Manuf. Rev.*, vol. 5, p. 7, 2018, doi: 10.1051/mfreview/2018001.

[39] M. Rahimian, N. Ehsani, N. Parvin, and H. reza Baharvandi, “The effect of particle size, sintering temperature and sintering time on the properties of Al–Al2O3 composites, made by powder metallurgy,” *J. Mater. Process. Technol.*, vol. 209, no. 14, pp. 5387–5393, Jul. 2009, doi: 10.1016/j.jmatprotec.2009.04.007.

[40] A. K. Bodukuri, K. Eswaraiah, K. Rajendar, and V. Sampath, “Fabrication of Al–SiC–B4C metal matrix composite by powder metallurgy technique and evaluating mechanical properties,” *Perspect. Sci.*, vol. 8, 2016, Accessed: Jan. 11, 2023. [Online]. Available: https://cyberleninka.org/article/n/508673

[41] A. Slipenyuk, V. Kuprin, Y. Milman, J. E. Spowart, and D. Miracle, “The effect of matrix to reinforcement particle size ratio (PSR) on the microstructure and mechanical properties of a P/M processed AlCuMn/SiCp MMC,” *Mater. Sci. Eng. A*, vol. 381, pp. 165–170, Sep. 2004, doi: 10.1016/j.msea.2004.04.040.

[42] B. Q. Han and K. C. Chan, “Superplastic deformation mechanisms of particulate reinforced aluminum matrix composites,” *Mater. Sci. Eng. A*, vol. 212, no. 2, pp. 256–264, Jul. 1996, doi: 10.1016/0921-5093(96)10208-2.

[43] S. Razavi, “EFFECT OF SUPERSOLIDUS LIQUID PHASE SINTERING ON THE MICROSTRUCTURE AND DENSIFICATION OF THE Al-Cu-Mg PREALLOYED POWDER,” Feb. 2011.

[44] R. J. Arsenault and N. Shi, “Dislocation generation due to differences between the coefficients of thermal expansion,” *Mater. Sci. Eng.*, vol. 81, pp. 175–187, Aug. 1986, doi: 10.1016/0025-5416(86)90261-2.

[45] R. B. Bhagat and M. B. House, “Elevated-temperature mechanical properties of silicon-carbide-whisker-reinforced aluminum matrix composites,” *Mater. Sci. Eng. A*, vol. 144, no. 1, pp. 319–326, Oct. 1991, doi: 10.1016/0921-5093(91)90239-J.
[46] K. H. Min, S. P. Kang, D.-G. Kim, and Y. D. Kim, “Sintering characteristic of Al2O3-reinforced 2xxx series Al composite powders,” *J. Alloys Compd.*, vol. 400, no. 1, pp. 150–153, Sep. 2005, doi: 10.1016/j.jallcom.2005.03.070.
[47] “Phase Transformations in Metals and Alloys (Revised Reprint) | David A.” https://www.taylorfrancis.com/books/mono/10.1201/9781439883570/phase-transformations-metals-alloys-revised-reprint-david-porter-kenneth-easterling-kenneth-easterling (accessed Jan. 11, 2023).
[48] M. Y. Misutsu *et al.*, *Thermoanalytical Methods in Verifying the Quality of Biodiesel*. IntechOpen, 2015. doi: 10.5772/59479.
[49] “X-ray Powder Diffraction (XRD),” *Methods*. https://serc.carleton.edu/msu_nanotech/methods/XRD.html (accessed Jan. 09, 2023).
[50] D. L. Zhang, D. Y. Ying, and P. Munroe, “Formation of Al2O3 during heating of an Al/TiO2 nanocomposite powder,” *J. Mater. Res.*, vol. 20, no. 2, pp. 307–313, Feb. 2005, doi: 10.1557/JMR.2005.0059.
[51] S. C. Tjong, G. S. Wang, and Y. W. Mai, “Low-cycle fatigue behavior of Al-based composites containing in situ TiB2, Al2O3 and Al3Ti reinforcements,” *Mater. Sci. Eng. A*, vol. 358, no. 1, pp. 99–106, Oct. 2003, doi: 10.1016/S0921-5093(03)00266-1.
[52] S. C. Tjong, G. S. Wang, and Y. W. Mai, “Low-cycle fatigue behavior of Al-based composites containing in situ TiB2, Al2O3 and Al3Ti reinforcements,” *Mater. Sci. Eng. A*, vol. 358, no. 1–2, pp. 99–106, Oct. 2003, doi: 10.1016/S0921-5093(03)00266-1.
[53] S. C. Tjong, G. S. Wang, and Y.-. W. Mai, “High cycle fatigue response of in-situ Al-based composites containing TiB2 and Al2O3 submicron particles,” *Compos. Sci. Technol.*, vol. 65, no. 10, pp. 1537–1546, Aug. 2005, doi: 10.1016/j.compscitech.2005.01.012.
[54] S. Q. Wu, H. G. Zhu, and S. C. Tjong, “Wear behavior of in situ Al-based composites containing TiB2, Al2O3, and Al3Ti particles,” *Metall. Mater. Trans. A*, vol. 30, no. 1, pp. 243–248, Jan. 1999, doi: 10.1007/s11661-999-0213-7.
[55] Z. Y. Ma, J. H. Li, S. X. Li, X. G. Ning, Y. X. Lu, and J. Bi, “Property-microstructure correlation in in situ formed AI203, TiB2 and AI3Ti mixture-reinforced aluminium composites,” p. 7.
[56] H. Huo and S. C. Tjong, “Corrosion Behavior of Al-based Composites ContainingIn-situ TiB2, Al2O3 and Al3Ti Reinforcements in Aerated 3.5 % Sodium Chloride Solution,” *Adv. Eng. Mater.*, vol. 9, no. 7, pp. 588–593, Jul. 2007, doi: 10.1002/adem.200700001.
[57] L. Jiang, Z. Li, G. Fan, and D. Zhang, “A flake powder metallurgy approach to Al2O3/Al biomimetic nanolaminated composites with enhanced ductility,” *Scr. Mater.*, vol. 65, no. 5, pp. 412–415, Sep. 2011, doi: 10.1016/j.scriptamat.2011.05.022.
[58] “mp-717: B2O3 (Orthorhombic, Cmc2_1, 36),” *Materials Project*. https://materialsproject.org/materials/mp-717/ (accessed Feb. 07, 2023).
[59] E. J. W. Verwey, “Electrolytic conduction of a solid insulator at high fields The formation of the anodic oxide film on aluminium,” *Physica*, vol. 2, no. 1, pp. 1059–1063, Jan. 1935, doi: 10.1016/S0031-8914(35)90193-8.
[60] B. C. Lippens and J. H. de Boer, “Study of phase transformations during calcination of aluminum hydroxides by selected area electron diffraction,” *Acta Crystallogr.*, vol. 17, no. 10, Art. no. 10, Oct. 1964, doi: 10.1107/S0365110X64003267.

[61] R.-S. Zhou and R. L. Snyder, “Structures and transformation mechanisms of the η, γ and θ transition aluminas,” *Acta Crystallogr. Sect. B*, vol. 47, no. 5, pp. 617–630, Oct. 1991, doi: 10.1107/S0108768191002719.
[62] “mp-1953: TiAl (Tetragonal, P4/mmm, 123),” *Materials Project*. https://materialsproject.org/materials/mp-1953 (accessed Jan. 17, 2023).
[63] V. Kevorkijan and S. Skapin, “Fabrication and characterization of TiAl/Ti3Al-based intermetallic composites (IMCs) reinforced with ceramic particles,” *Arch. Mater. Sci. Eng.*, vol. 40, Dec. 2009.
[64] “mp-944: AlB2 (Hexagonal, P6/mmm, 191),” *Materials Project*. https://materialsproject.org/materials/mp-944 (accessed Feb. 07, 2023).
[65] “mp-1145: TiB2 (Hexagonal, P6/mmm, 191),” *Materials Project*. https://materialsproject.org/materials/mp-1145/ (accessed Feb. 07, 2023).
[66] S. Pichumani, R. Srinivasan, and V. Ramamoorthi, “Investigation on mechanical behavior and material characteristics of various weight composition of SiCp reinforced aluminium metal matrix composite,” *IOP Conf. Ser. Mater. Sci. Eng.*, vol. 310, p. 012082, Feb. 2018, doi: 10.1088/1757-899X/310/1/012082.